

THESIS

TIME-FILTERED INVERSE MODELING OF LAND-ATMOSPHERE CARBON EXCHANGE

Submitted by

Nicholas M. Geyer

Department of Atmospheric Science

In partial fulfillment of the requirements

For the Degree of Master of Science

Colorado State University

Fort Collins, Colorado

Fall 2015

Master's Committee:

Advisor: Scott Denning

Jennifer Hoeting
Christopher O'Dell

Copyright by Nicholas M. Geyer 2015

All Rights Reserved

ABSTRACT

TIME-FILTERED INVERSE MODELING OF LAND-ATMOSPHERE CARBON EXCHANGE

The sources and sinks of biospheric carbon dioxide represent one of the least understood and most critical processes in carbon science. Since the 1990s, carbon dioxide inversion models have estimated the magnitude, location, and uncertainty of carbon sources and sinks. These inversions are underconstrained statistical problems that employ aggressive statistical regularizations in both space and time to estimate quantities like net ecosystem exchange (NEE) on weekly timescales over fine spatial scales. This study developed and tested a new regularization that leverages the available observational information toward a small number of estimates associated with the longer-lived slowly varying biospheric processes, which control time-averaged sources and sinks of CO₂. This approach multiplicatively adjusts the longer lived component fluxes, gross primary production (GPP) and total respiration (RESP), using several timescale harmonics. This methodology was tested by estimating adjustments to either net or component fluxes from Simple Biosphere Model 4 (SiB4) using observational data from 8 different eddy-covariance flux towers selected from the North American Carbon Program (NACP) site synthesis dataset. The time-filtering methodology was robustly capable of accurately estimating both net and component fluxes given high observational uncertainty. Furthermore, the methodology was flexible of correctly producing estimates of all three fluxes when given a component flux as an additional observational constraint.

ACKNOWLEDGMENTS

I would express my gratitude, humility, and respect to the many people that I have interacted with throughout the research, development, and writing of this Thesis. First, I want to thank my advisor Dr. Scott Denning for allowing me the opportunity to perform cutting edge and quality research under one foremost scientists in carbon science field. Next, I would like to thank my the remaining Master's Committee members consisting Dr. Christopher O'Dell and Dr. Jennifer Hoeting. These two were consistently providing advice, suggestions, and aid throughout the development of this project and when I needed your advice. Next, I want to thank my research group both past and present. In particular, I want to acknowledge the hard work, help, and support of Dr. Ian Baker, Dr. Katherine Haynes, Dr. Andrew Schuh, Morgan Philips, and Aaron Piña. Without these dedicated researchers, I would have never had the theoretical background, land-model development, or basic common sense for when I needed interpretation.

I want to acknowledge my friends, family, and fellow graduate students. In particular, I especially want to recognize the support of Christopher Slocum and Danielle Thomas. Chris not only gave me the formatting for this thesis, but went above and beyond to be one the most supportive cohorts I have ever had the privilege to meet. The fellowship, support, and friendship he gave when I needed to make it through some tough times was immeasurably valueable and I hopefully can return the favor one day. To Danielle Thomas, thank you for the love, cookies, jokes and joy you bring to my life. The grammatical and emotional support she showed in all facets of this academic ordeal were especially helpful.

DEDICATION

This Thesis is dedicated to my mother.

She gave me the strength and courage to always

find a way to better myself and my life.

I love you Mom.

TABLE OF CONTENTS

Abstract	ii
Acknowledgments	iii
Dedication	iv
List of Tables	vii
List of Figures	viii
Chapter 1. Introduction	1
1.1. Inversion Modeling	3
1.2. Purpose	8
Chapter 2. Methods	15
2.1. Bias Correction Factors	15
2.2. Kalman Filter for Harmonic β s	17
2.3. Carbon Flux Tower Network	20
2.4. Simple Biosphere Model 4	22
2.5. Experimental Design	24
2.6. Hypotheses Testing and Significance	31
Chapter 3. Results	46
3.1. How Many Harmonics are Necessary?	46
3.2. Experiment 1	47
3.3. Experiment 2	50
3.4. Experiment 3	55

Chapter 4. Discussion	84
4.1. Experiment 1 Interpretations	84
4.2. Experiment 2 Interpretations	85
4.3. Experiment 3 Interpretations	87
Chapter 5. Conclusions and Future Work	91
References	94
Appendix A. Kalman Filter Derivation	100
A.1. Bayes Theorem and Assumptions	100
A.2. Kalman Filter Equations: State Estimate Update Equation	104
A.3. Kalman Filter Equations: State Covariance Matrix	106

LIST OF TABLES

2.1	Possible Sources of Bias in SiB4	40
2.2	Variables in Kalman Filter	40
2.3	List of Sites and Site Characteristics Used	41
2.4	List of PFTs in SiB4	41
2.5	Experiments to Test the Hypotheses	42
2.6	Experimental Set-Ups	43
2.7	Hypothesis Testing Methods	43
3.1	Results of Statistical Testing: Experiment 1	81
3.2	Results of Statistical Testing: Experiment 2	82
3.3	Results of Statistical Testing: Experiment 3	83
4.1	Hypotheses Results	90
A.1	Variables in Kalman Filter Derivation	109

LIST OF FIGURES

1.1	CO ₂ Emission Scenarios from Fossil Fuels	2
1.2	Partitioning of Anthropogenic Emissions over Time	4
2.1	Flow Diagram of Kalman Filter Estimation Procedure	44
2.2	Map of Tower Sites	44
2.3	Schematic of SiB4	45
3.1	Error Variance Explained by Power of Harmonics	60
3.2	Component Fluxes for Pre-assimilation and Control: Deciduous Broadleaf Forests	61
3.3	Fractional Reduction of RMSE of NEE	62
3.4	Fractional Reduction of RMSE of the Component Fluxes	63
3.5	Annual NEE Fluxes as Influenced by Increasing Observational Uncertainty for Experiment 1: Harvard Forest	64
3.6	Annual NEE Fluxes as Influenced by Increasing Observational Uncertainty for Experiment 1: Vaira Ranch	65
3.7	Cross-correlation and Autocorrelation Functions for Experiment 1	66
3.8	Mean Power Spectra of NEE for All Experiments	67
3.9	Component Fluxes for Experiment 2	68
3.10	Annual NEE Fluxes as Influenced by Increasing Observational Uncertainty for Experiment 2: Harvard Forest	69
3.11	Annual NEE Fluxes as Influenced by Increasing Observational Uncertainty for Experiment 2: Vaira Ranch	70
3.12	Cross-correlation and Autocorrelation Functions for NEE: Experiment 2	71

3.13 Cross-correlation and Autocorrelation Functions of Component Fluxes Experiment 2:	
Harvard Forest	72
3.14 Cross-correlation and Autocorrelation Functions of Component Fluxes Experiment 2:	
Vaira Ranch	73
3.15 Mean Power Spectra of Component Fluxes for Experiments 2 and 3	74
3.16 Component Fluxes for Experiment 3	75
3.17 Annual NEE Fluxes as Influenced by Increasing Observational Uncertainty for	
Experiment 3: Harvard Forest	76
3.18 Annual NEE Fluxes as Influenced by Increasing Observational Uncertainty for	
Experiment 3: Vaira Ranch	77
3.19 Cross-correlation and Autocorrelation Functions for NEE: Experiment 3	78
3.20 Cross-correlation and Autocorrelation Functions of Component Fluxes Experiment 3:	
Harvard Forest	79
3.21 Cross-correlation and Autocorrelation Functions of Component Fluxes Experiment 3:	
Vaira Ranch	80

CHAPTER 1

INTRODUCTION

In May 2014, carbon dioxide (CO₂) measurements taken by the National Oceanic and Atmospheric Administration (NOAA) indicated that atmospheric levels of CO₂ had risen above 400 parts per million (ppm) for the first time in recorded human history (ESRL 2014). This was determined to be the result of human activities including increased global fossil fuel consumption, cement production, and land-use change over the last 150 years (IPCC 2013; ESRL 2014). As seen in Figure 1.1, the Intergovernmental Panel on Climate Change (IPCC) Assessment Report 5 (AR5) estimates that future anthropogenic emissions of CO₂ may range between 6 to 25 PgC (1 PgC = 10¹⁵ gC) which would result in CO₂ concentrations of between 400 and 950 parts per million (ppm) by 2100 (IPCC 2013). This concentration range infers that global climate models (GCMs) have difficulty to match historical observations and converge toward similar climate predictions (IPCC 2013). The difficulty in GCM prediction is due to both uncertainty in how much CO₂ humanity will emit and how nature will react over this timeframe (IPCC 2013). This severely restricts the ability of researchers to accurately measure the effects of policy on global warming. A large contributor to the high levels of uncertainty in current estimates comes from a lack of understanding about the location and magnitude of carbon cycle sinks from the atmosphere (Friedlingstein et al. 2006; Hoffman et al. 2014).

Determination of the atmospheric sources and sinks of CO₂ is a fundamental goal of carbon science for predicting future climate change. Earth's carbon cycle is comprised of both inactive and active pools of carbon. The inactive pool is carbon stored in sedimentary rock, while the three active carbon pools consist of the atmosphere, ocean, and terrestrial biosphere (UNH 2014). The estimates of the influence of CO₂ on the atmospheric and ocean pools are well observed, but

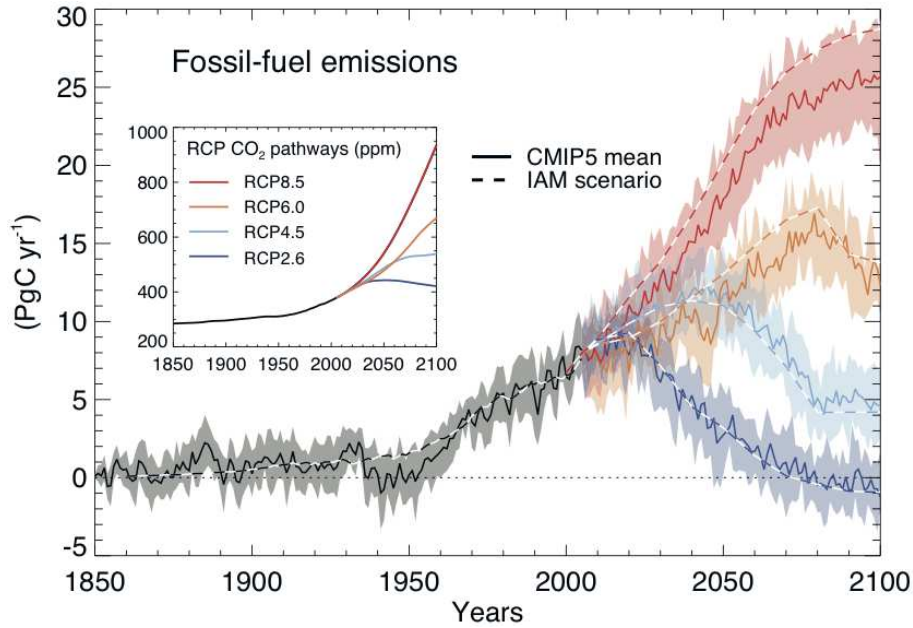


FIG. 1.1. Fossil fuel emissions scenarios from the IPCC AR5 and CMIP5 experiments. Each line represents a different emission scenario civilization could take in the future. The solid line represents the mean emissions and shaded represent the variability the scenario could take. The nested graph represents the equivalent atmospheric concentration of CO_2 . The y-axis is the global emission rate in units of $\frac{\text{PgC}}{\text{yr}}$ and the x-axis is time in units of years. Diagram courtesy of (IPCC 2013).

biospheric CO_2 estimates need to be improved upon. Observational studies during the 1950s and 1960s suggested that in order to resolve the carbon budget there must exist a net sink of CO_2 into both the oceans and terrestrial biosphere (Bolin and Eriksson 1958; Bolin and Keeling 1963). Over the next 50 years, observational estimates of this sink suggested that roughly 50% of anthropogenic CO_2 emissions remain in the atmosphere, while the other 50% are fluxed into the ocean and terrestrial biosphere pools (Bolin and Bischoff 1970; IPCC 2013). Oceans are well known chemistry driven sinks of CO_2 (Drever 1988; Sabine et al. 2004). The magnitude of the oceanic sink was observed to be a quarter of anthropogenic CO_2 emissions, while the other quarter is accounted for by terrestrial biosphere to close the balance (Bolin and Bischoff 1970; Ciais et al. 1995; Sabine et al. 2004). Recent estimates suggested that of the 555 PgC that humans have emitted into the atmosphere since the 1800s, the oceans and biosphere were responsible for sinking 155 ± 30 PgC

and 160 ± 90 PgC, respectively (IPCC 2013). The biosphere sink estimate has an uncertainty estimate that is over half of the flux itself. Uncertainty associated with these recent estimates was due to both the sparse number of observations available and the lack of understanding biological processes involving carbon.

To understand the biological sink, it is important to accurately measure the locations and strengths of sources and sinks of biospheric CO₂. One of the difficulties in attaining an accurate estimate of the biospheric sink is due to the fact that biology can adapt to different conditions of CO₂. Shown in Figure 1.2 are the IPCC's estimates from the Coupled Model Intercomparison Project Phase 5 (CMIP5) experiment's variations of the CO₂ sink partition. These estimates showed that the land portion of the sink varied between $1 \frac{GtC}{yr}$ to $-4 \frac{GtC}{yr}$ since the 1800s. The IPCC noted that in both the 4th and 5th assessment reports (AR4, AR5) a large source of this variation occurred because of the GCMs' high sensitivity to the locations of carbon sources and sinks and biological parameterizations (Friedlingstein et al. 2006; Hoffman et al. 2014). A way to determine the magnitude and location of this sink is through inversion modeling.

1.1. INVERSION MODELING

Inversion modeling is a popular technique designed to infer the locations and strengths of the sources and sinks of CO₂. The inversion is a statistical model that allows an initial estimates of CO₂ fluxes, then uses an atmospheric transport model to estimate CO₂ concentrations. The inversion then uses observations to optimize biospheric fluxes in order to match CO₂ concentrations (Evensen 1994). In general, CO₂ inversion models provide underconstrained flux estimates. This means there are many more parameters to estimate than observations to constrain them. To compensate for the lack of observations, inversion frameworks have been developed to introduce aggressive regularizations to allow for more constrained estimates of CO₂ fluxes.

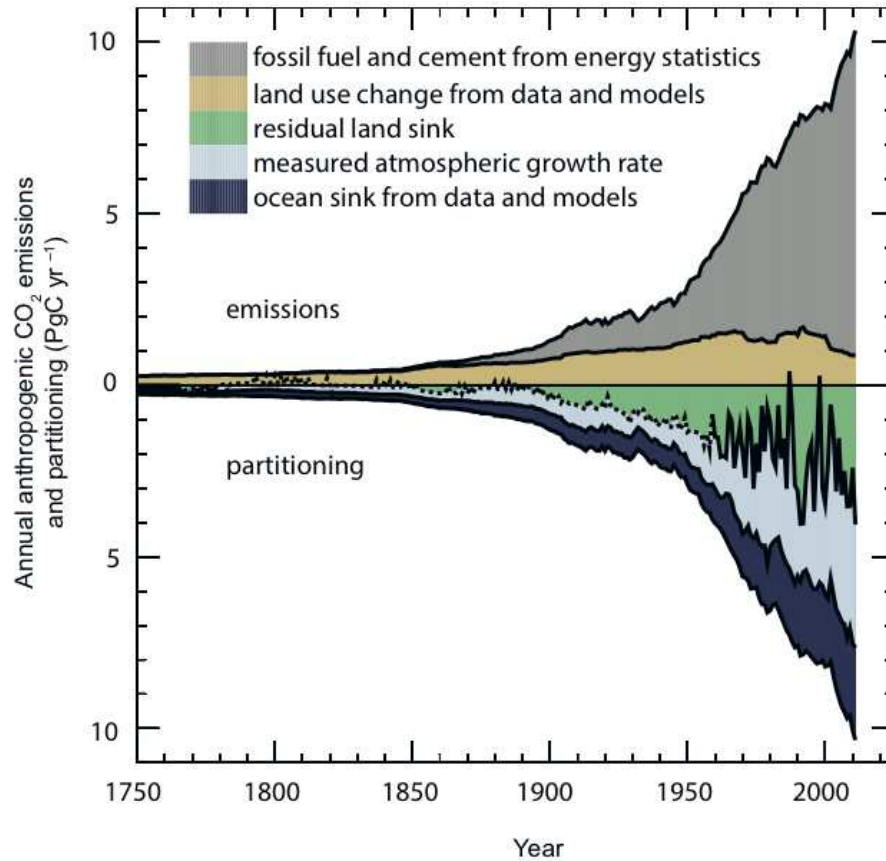


FIG. 1.2. Estimations of how anthropogenic emissions of CO₂ are being partitioned and evolving by the land and ocean carbon pools over time. Diagram courtesy of (IPCC 2013)

The creation of a large network of carbon flask observations and eddy-covariance towers made it possible to use pre-aggregated observations and biological regions as early regularizations. Pre-aggregation refers to using the coarse observational network of fluxes and concentrations to associate basic flux patterns with particular regions of the world. In this manner, the number of estimated flux parameters in the inversion framework is substantially reduced to compensate for the relative concentrations of available CO₂ observations. In the late 1980s, early inversion studies using spatial aggregation showed that a large Northern Hemispheric mid-latitude land CO₂ sink of 2.0 to 3.4 $\frac{\text{PgC}}{\text{yr}}$ was responsible for closing the carbon budget. This early work was plagued with source-sink errors in atmospheric transport and a sparse observational network over the whole globe (Tans

et al. 1990). In the 1990s and early 2000s, the experiments performed under the Atmospheric Tracer Transport Model Intercomparison Project (TransCom) project resulted in an intercomparison study used to determine the strength and causes of a bias between inversion frameworks and observations (Gurney and Denning 2007). The project found the Northern Hemispheric sink estimates that generally agreed with estimates derived from eddy-covariance towers and historical carbon budget studies, however the model fluxes were lacking in precision (Baldocchi and Coauthors 2001; Baldocchi 2008; Houghton 1999). Flux estimate biases were noted to be caused by errors arising from the combination of a sparse observing network, coarse spatial resolution, poor atmospheric transport models, and poor land-model parameterizations. Improvements in spatial resolution of the observations and the models themselves were suggested to help alleviate estimate biases (Law et al. 1996; Denning et al. 1999; Gurney et al. 2002, 2004; Bakwin et al. 1998; Baker et al. 2006; Kawa et al. 2004). In the mid-2000s, research was focused on addressing the observing network.

By the mid-2000s, advancements in computational resources and better models allowed for studies of the regularizations associated with poor spatial resolution flux estimates. Studies during this time focused on estimating the regional-scale fluxes scaled to the resolution of the atmospheric transport model. This method assessed the aggregation of errors when prescribed fluxes are not accurately assigned within spatial regions (Kaminski et al. 1999; Rödenbeck et al. 2003). These studies showed that the sparse resolution of both observations and models can violate the Bayesian assumptions associated with inversion models (Michalak et al. 2004). Efforts to alleviate this problem were accomplished by introducing pseudo-observations to fill in the observational gaps. Some examples included incorporating either correlation length scales between similar ecosystems over nearby grid-cells or geostatistical smoothing of flux strengths between grid-cells (Kaminski et al. 1999; Rödenbeck et al. 2003; Michalak et al. 2004; Michalak 2008). These studies reproduced

similar magnitude fluxes to previous studies, but at a higher precision. While these methods to increase resolution did work, these methods suffered from poor flux constraints to operate efficiently.

In the later 2000s, methods to increase the information associated with prior flux estimates were used to address the issues associated with increased spatial resolution. Prior fluxes must be measured at a regular frequency to constrain observational and modeled background fluxes. An example inversion project being employed for CO₂ inversions that uses continuous observations of CO₂ to make estimates of these prior fluxes is CarbonTracker (Chevallier et al. 2009; Peters et al. 2007). CarbonTracker is an inversion modeling system that makes weekly flux estimates of net ecosystem exchange (NEE) of the entire globe on a 1° by 1° spatial grid. The inversion framework of CarbonTracker makes use of a concept known as ecoregions to provide spatial regularization. Ecoregions are large expanses of land that generalize ecosystems with similar characteristics, which dramatically lowers the number of estimated parameters. The use ecoregions on the spatial grid allows CarbonTracker to produce 6552 estimated parameters per year(CarbonTracker 2014). Modeling via ecoregions coupled with higher resolution transport models, improved land models, and eddy-covariance towers tightly constrained regional estimations of CO₂ fluxes on a weekly basis, but when downscaled to the spatial grid were not verified by flux observations (Peters et al. 2007, 2010; CarbonTracker 2014). With high resolution and temporally regular estimates of CO₂ prior fluxes now available, it has been suggested that uncertainty studies should be focused on making better biological process models (Peters et al. 2007; CarbonTracker 2014; Hurtt and Kang 2014).

Since improvement from observational platforms from carbon flasks, eddy-covariance towers, and satellites can provide reasonable and frequent flux observation records, the focus of improved inversion estimates must shift toward development of more accurate flux estimates from

land-atmosphere models. Land-atmosphere models can be improved through the estimation of biological flux biases incurred from spatio-temporal flux correlations, model mis-timing, and other systematic model errors on several spatio-temporal scales. Inversion systems like CarbonTracker can translate the estimated fluxes to provide flux bias corrections as seen in (1.1).

$$NEE_{obs}(\lambda, \phi, t) = (1 + \beta_{NEE}(t))NEE_{model}(\lambda, \phi, t) \quad (1.1)$$

Where λ is the longitude, ϕ is the latitude, and t is time. In this formulation, β is the time-dependent bias correction of modeled NEE to observed NEE varying in time and space. Fundamentally, (1.1) suggests that following the week-to-week variations in model to observation errors can better identify issues in land model fluxes. Chasing week-to-week will obtain some estimate of shorter scale bias, but another school of thought was to extend this methodology toward longer scale biases. Longer scale biases were obtained through the introduction of inversion variants like maximum likelihood ensemble filter (MLEF) and ensemble Kalman filter to remove the adjoint model associated with atmospheric CO₂ transportation (Zupanski et al. 2007; Michalak et al. 2004). These inversion frameworks used suites of Monty-Carlo ensembles of flux optimizations to provide better constraint of posterior fluxes. These studies provided estimates of flux biases on regional and global scales while using a modest number of ensemble members even with low observational constraint (Zupanski et al. 2007; Lokupitiya et al. 2008). This was due to their fundamental assumption that biases from modeled NEE fluxes were the result of persistent and long-lived errors from the two contrasting component fluxes: gross primary production (GPP) and ecosystem respiration (RESP). Under this assumption, bias estimates only had to be updated every few months rather than every week. These algorithms reduced the time dimensionality of the inversion problem at a grid-cell by reducing the number of parameters estimated from 52 to 6 per year. This

lowers the computational requirements for the inversion, which could then allow for increased the spatial resolution. In these frameworks rather than adjusting for the NEE biases themselves, GPP and RESP are adjusted in the following manner:

$$NEE_{obs}(\lambda, \phi, t) = (1 + \beta_{RESP}(t))RESP_{model}(\lambda, \phi, t) - (1 + \beta_{GPP}(t))GPP_{model}(\lambda, \phi, t) \quad (1.2)$$

Unlike in (1.1), this formulation of β is now the time-dependent bias correction of a particular component flux varying in time and space. Using the gross component fluxes in this manner has two advantages. The first is increased insight into the mechanisms causing the biases in GPP and RESP separately. The second is the ability to capture the “slowly-varying” biases, since both opposing gross fluxes have known time signals, unlike more noisy NEE measurements. This methodology prevents “wasting” precious information content of the atmospheric observations on estimation of well-known ecosystem properties by focusing the corrections on persistent, scientifically valuable and statistically stable quantities with predictive power. The applications of this methodology have been shown to substantially reduce large-scale carbon biases and variability and produce accurate high-resolution flux estimates (Schuh et al. 2009, 2010, 2013). While isolating the biological biases improves inversion estimates, the usage of a single bias term does not identify the particular slow processes in a model that make the bias. This does not provide information on where or how to improve prior modeled flux estimates. This shortcoming must be addressed to provide additional constraint on inversion estimates of biological sources and sinks of CO₂.

1.2. PURPOSE

In each of the previously mentioned regularization methods, errors in estimated fluxes come from one or more of the following problems:

- (1) Inability to isolate multiple slowly-varying biases in a continuous manner.
- (2) Week-to-week assimilation updates with no *a priori* knowledge of previous CO₂ fluxes.
- (3) Inability to properly reconstruct the GPP and RESP CO₂ fluxes.
- (4) Necessity for decorrelation length scales in space.
- (5) Inability to estimate bias due to poor observational constraints.

These issues are the focus of present day spatio-temporal methods, but with more observational information available everyday a spatio-temporal method may not be most useful route for estimating future biospheric flux locations and strength. This research presents an solution to these problems by shifting the temporal aspect to a yearly temporal harmonic smoothing regularization. This is accomplished by adapting the work of Zupanski et al. (2007), Schuh et al. (2009), and Lokupitiya et al. (2008) to fit a harmonic smoother to isolate multiple long-term biases in flux estimates.

A temporal smoothing regularization that is capable of assessing slowly-varying flux biases in a continuous manner must be capable of assessing biases on several timescales and have the ability to “learn” about the biases over time. Under the formulation presented in equation (1.2), the bias coefficients are updated every few months using both accumulated observational data and the previous assimilation cycle’s posterior estimates and uncertainties in the current assimilation step (Zupanski et al. 2007; Lokupitiya et al. 2008). By doing this, the bias coefficient estimates are updated and adjusted slowly in such a way that these estimates can “learn” about the bias in order to adjust toward a stable solution as more data is assimilated in a non-isotropic way. However, these formulations are only able to estimate biases on one timescale. A single bias estimate is insufficient to fully describe the errors from the biological parameterizations in present day land-models. For instance, errors from long-lived soil pool turnover times and shorter-lived

biological Q^{10} temperature responses may result in an aliased persistent bias in respiration that is not controlled by one variable on one timescale. This makes attribution of model parameter errors more difficult to do in a temporal regularization. A more realistic formulation can be accomplished by deconstructing the bias coefficient in equation (1.2) into several terms that are associated with yearly, seasonal, and sub-seasonal timescale flux biases as seen equation (1.3).

$$\beta_{RESP,GPP} = \bar{\beta}_{RESP,GPP} + \beta_{RESP,GPP}^{seasonal} + \beta_{RESP,GPP}^{sub-seasonal} \quad (1.3)$$

Where $\bar{\beta}_{RESP,GPP}$ quantifies biases of the annually average, $\beta_{RESP,GPP}^{seasonal}$ quantifies seasonal scale biases, and $\beta_{RESP,GPP}^{sub-seasonal}$ quantifies subseasonal noise. Under this decomposition, flux biases can be associated with the responsible mechanisms and parameterizations in models while retaining the same ability to “learn” about the biases as more observations are assimilated. These bias coefficients can be either discretely or continuously estimated. This research uses equation (1.3) in a continuous formulation using harmonics, seen in (1.3), estimated every year as opposed to present day week-to-week assimilation systems.

The bias coefficients of equation (1.3) should be updated annually rather than on week-to-week or monthly timescales. This effectively retains the number of estimated parameters and spatial improvements of the studies from Zupanski et al. (2007); Schuh et al. (2009); Lokupitiya et al. (2008), but allows for full years to be assimilated at once rather than in increments. Modeling efforts must be focused toward seasonal, interannual, and decadal timescales because these are the timescales needed to properly characterize the mechanisms responsible for an ecosystem’s CO_2 source and sink strength. Poorly understood ecological processes in models may not be able to respond properly to long term ecosystem controls like disturbances, succession, and fertilization. These processes would therefore produce which can produce long term errors in flux estimates that

week-to-week bias corrections cannot properly characterize. Flux estimates from CarbonTracker are generally good at correcting the week-to-week variations in NEE, but they are incapable of properly characterizing the longer timescale processes that can systematically effects annual carbon budgets. Flux bias estimation could be much more efficient if the numerical power of the observations were focused toward longer timescale variations rather than week-to-week variations of model flux estimates.

There are two gains to the assimilation process when temporally smoothing to isolate long-lived biases. First, the flux bias estimates are fundamentally better constrained with observations. Since the bias coefficients of equation (1.3) require at least a year's worth of data to be estimated, they are inherently better constrained with more observations. This strengthens the Gaussian assumptions in CO₂ inversions over that of weekly updates. The second advantage is that there is a computational gain by only estimating 3 to 11 bias coefficients rather than 52 bias coefficients. As previously mentioned, spatial smoothing algorithms like CarbonTracker are able to estimate a bias coefficient every week for each ecoregion. Placing this into a computational context, these regularization algorithms can estimate 52 bias coefficients every year for each ecoregion over the globe, which is both computationally straining and unnecessary. If the focus of the numerical power of observations were focused toward long lived biases over a yearly assimilation cycle, then the number of estimated parameters becomes 3 to 11 bias coefficients per ecoregion per year rather than 52. This means temporal smoothing regularizations require a number of operations less than or equal to that of spatial regularizations while retaining a similar spatial resolution. There is a clear advantage in using temporal smoothing regularizations over that of current regularizations, but this power is only gained once there are enough observations.

Since equation (1.3) requires a sufficiently long time series of fluxes and uncertainties estimates of those fluxes to resolve the longest timescale biases, there is an issue with obtaining a global time series of fluxes. Spatial regularizations were originally designed to compensate statistically for the lack of CO₂ observations to constrain estimates. While useful, spatial methods suffer from biases involving unequal sampling coverage and issues with decorrelation length scales. With the dawn of new carbon observing satellites like OCO-2 in orbit, there now exists the possibility to globally quantify CO₂ fluxes and their uncertainties down to about few kilometers with even temporal frequency. This provides an opportunity to aggregate satellite data over a long enough time to produce a time series of fluxes for each cell or ecoregion over the globe at the resolution of the satellite. Given enough time to aggregate this data could, in principle, eliminates the unequal sampling coverage problem and the need for decorrelation length scales. Unfortunately, these satellite products have not been aggregated for long enough to provide sufficient amounts of data for this study. Instead, this research is developed as a site-level prototype of the temporal smoothing regularization. This approach uses eddy covariance towers from the FLUXNET network to provide hourly and half hourly observations of fluxes and the daily flux uncertainty estimates from (Barr et al. 2013) as the observational constraints over a variety of years. The usage of this data provides this study with an overconstrained inversion problem for the bias coefficients in equation (1.3), which serves as a test bed for examining the limits of observational constraints and uncertainty for both week-to-week and temporal smoothing regularizations.

In summary, this thesis presents a technique to isolate the longer lived biases of land-atmosphere model fluxes by temporally smoothing modeled fluxes to remove shorter timescale variations. This can more appropriately address the biases associated with poorly understood slowly varying processes, which should produce a much better estimate of seasonal, interannual, and decadal

timescale CO₂ fluxes. Through the use yearly time series of daily averaged GPP, RESP, and NEE observed and modeled fluxes as well as their uncertainties at an eddy covariance tower, there will be enough data to overconstrain the inversion problem and test the limits of a control algorithm mimicking week-to-week assimilation cycles and a continuous harmonic formulation of equation (1.3).

To further understand the biospheric sink, this thesis addresses the following hypotheses tested across many ecosystems and uncertainty scenarios:

- (1) A time smoothing regularization provides a better *a posteriori* average estimate of the interannual NEE flux than an estimate produced using a current week-to-week assimilation algorithms.
- (2) A time smoothing regularization provides a better *a posteriori* estimate of the seasonal cycle of the NEE flux than an estimate produced using a current week-to-week assimilation algorithms.
- (3) A time smoothing regularization provides a better *a posteriori* average estimate of the interannual NEE flux than an estimate produced using a current week-to-week assimilation algorithms when using NEE as the only constraining observational flux.
- (4) A time smoothing regularization provides a better *a posteriori* estimate of the seasonal cycle of the NEE flux than an estimate produced using a current week-to-week assimilation algorithms when using NEE as the only constraining observational flux.
- (5) A time smoothing regularization accurately estimates the seasonal cycle and interannual average of GPP and RESP when using NEE as the only constraining observational flux.

- (6) A time smoothing regularization provides a better *a posteriori* average estimate of the interannual NEE flux than an estimate produced using a current week-to-week assimilation algorithms when using NEE and a component flux as the constraining observations.
- (7) A time smoothing regularization provides a better *a posteriori* estimate of the seasonal cycle of the NEE flux than that of current week-to-week assimilation algorithms when using NEE and a component flux as the constraining observations.
- (8) A time smoothing regularization accurately estimates the seasonal cycle and interannual average of GPP and RESP when using NEE and a component flux as the constraining observations.

CHAPTER 2

METHODS

2.1. BIAS CORRECTION FACTORS

As seen in equation (1.3), the time smoothing algorithm was conceived by separating faster more well-understood processes like radiation and temperature from slower less-understood processes like biogeochemistry and phenological triggers. The mapping of modeled to observed gross fluxes at any point in time for NEE, GPP, and RESP are given by

$$\begin{aligned} NEE_{obs}(t) &= [1 + \beta_{RESP}(t)] RESP_{model}(t) - [1 + \beta_{GPP}(t)] GPP_{model}(t) + \epsilon \\ &= [1 + \beta_{NEE}(t)] NEE_{model}(t) + \epsilon \end{aligned} \tag{2.1}$$

$$GPP_{obs}(t) = [1 + \beta_{GPP}(t)] GPP_{model}(t) + \epsilon \tag{2.2}$$

$$RESP_{obs}(t) = [1 + \beta_{RESP}(t)] RESP_{model}(t) + \epsilon$$

here t indicates time, β is the bias correction and ϵ is an error term between the observed and modeled fluxes. The GPP and RESP fluxes can be optimized as a standalone fluxes ((2.2)) or simultaneously using NEE ((2.1)). In these equations, β represents a multiplicative correction term to map the two vectors of fluxes on the measurement timescale. This method allows for the fluxes to vary from hourly to decadal timescales, but assumes flux biases persist on timescales longer than that of the fluxes. A single bias coefficient used in this form gives little suggestion for what could be responsible for the errors in models. This is because bias coefficients used in this manner misuse the statistical strength of the observations to correct for well-known ecosystem properties. To overcome this, β can be decomposed into three terms to separate the unknown and well-known biases, as suggested in equation (1.3). Studies have shown that the biases in our land-atmosphere

model, SiB4, are associated with various phenological, physiological, location based biases. As seen in Table 2.1, these example parameters are mechanistic. This indicates that application of the bias corrections should be multiplicative rather additive when applied to the gross fluxes. By decomposing β in this way, the statistical power and stability of the observational information is used toward estimating the biases in slowly-varying processes only.

A continuous slowly-varying time series of the bias coefficients is preferable to discrete estimates at each time and location. In a discrete estimation framework using (1.3), there are physical and mathematical possibilities which can cause misrepresentative values or discontinuities in the estimate. This is alleviated by using a continuous estimate of the bias coefficients. Equation (2.3) is used to introduce a harmonic and continuous time series of the bias coefficients.

$$\beta_{GPP/RESP} = \bar{\beta}_{GPP/RESP} + \sum_{k=1}^L (\beta_{A,k} \cos \omega_k i + \beta_{B,k} \sin \omega_k i) + \beta''_{GPP/RESP} \quad (2.3)$$

$$1 < L \leq \frac{N}{2} \quad (2.4)$$

$$\omega_k = \frac{2\pi k \Delta t}{N}$$

where L is the number of total number of harmonics, k is the wavenumber of a harmonic, i is the i^{th} day of year, and N is the number of days in a year. In this formulation, the annual average correction ($\bar{\beta}_{GPP/RESP}$) and subseasonal noise ($\beta''_{GPP/RESP}$) were retained, but $\beta'_{GPP/RESP}$ is decomposed into component bias harmonics over a yearly timescales (i.e. N=365). As seen in equation (2.4), the bias coefficients from equation (2.3) are limited to the Nyquist frequency of the time series. The Nyquist frequency theorem states that to prevent aliasing in a signal, the signal can only be resolved to $\frac{N}{2}$ of the sampling rate. In this study, the lowest resolvable frequency is the

180th harmonic. Since many biospheric mechanisms are cyclical over interannual, seasonal, and subseasonal timescales, harmonics are a natural fit for continuous bias estimation.

2.2. KALMAN FILTER FOR HARMONIC β S

The Kalman filter was the optimization algorithm used in this study to estimate the bias coefficients. The choice of the Kalman filter over the more advanced methods, like a 4DVar or an Ensemble Kalman filter, was because the length of the observational record being used was much larger than number of estimated parameters. This study, by design, was an overconstrained problem. This meant that a Kalman filter can be used without issue. The full derivation of the Kalman filter equations used in this study are presented in appendix A, however the important points are presented here.

The cost function for the Kalman filter used in this study is given by

$$\Psi = \left[(\vec{m}_t^{upd} - \vec{m}_t^{pre})^T \mathbf{C}_\beta^{-1} (\vec{m}_t^{upd} - \vec{m}_t^{pre}) + (\mathbf{d}_t - \mathbf{G}_t \vec{m}_t^{upd})^T \mathbf{C}_{d,t}^{-1} (\mathbf{d}_t - \mathbf{G}_t \vec{m}_t^{upd}) \right] \quad (2.5)$$

Following some matrix identities and algebra, the Kalman filter equations can be derived for use.

The equations used in this study with respect to the bias coefficients, β , are given as

$$\vec{m}_t^{pre} = \mathbf{A}_{t-1} \vec{m}_{t-1}^{upd} + \mu_t \quad (2.6)$$

$$\mathbf{C}_{\beta,t}^{pre} = \mathbf{A}_{t-1}^T \mathbf{C}_{\beta,t-1}^{upd} \mathbf{A}_{t-1} + \mathbf{Q}_{t-1} \quad (2.7)$$

$$\mathbf{K}_t = \frac{\mathbf{C}_{\beta,t}^{pre} \mathbf{G}_t^T}{\mathbf{C}_{d,t} + \mathbf{G}_t^T \mathbf{C}_{\beta,t}^{pre} \mathbf{G}_t} \quad (2.8)$$

$$\vec{m}_t^{upd} = \vec{m}_t^{pre} + \mathbf{K}_t (\mathbf{d}_t - \mathbf{G}_t \vec{m}_t^{pre}) \quad (2.9)$$

$$\mathbf{C}_{\beta,t}^{upd,*} = (\mathbf{I} - \mathbf{K}_t \mathbf{G}_t)^T \mathbf{C}_{\beta,t}^{pre} (\mathbf{I} - \mathbf{K}_t \mathbf{G}_t) + \mathbf{K}_t^T \mathbf{C}_{d,t} \mathbf{K}_t \quad (2.10)$$

$$\mathbf{C}_{\beta,t}^{upd} = \mathbf{C}_{\beta,t}^{upd,*}(w) + \mathbf{C}_{\beta,t}^{pre}(1-w) \quad (2.11)$$

where the definition of all of these terms seen above are given in table 2.2.

Equation (2.10) for $\mathbf{C}_{\beta,t}^{upd,*}$ is known as the ‘‘Joesph’s Form’’ of the state covariance matrix update equation. This form is not typically seen in many studies because it is usually more computationally inefficient than an optimal Kalman Gain solution to the same equation. This form is being used because the state covariance update step can be vulnerable to round off errors, which breaks a symmetry assumption underlying the Kalman Gain. If this occurs, then the *a posteriori* state covariance matrix will become negative. This will cause the algorithm to become become invalidated. Additionally, equation (2.11) presents a new term, w . w is a tuning parameter between 0 and 1 that artificially inflates the *a posteriori* state covariance matrix (Zhang et al. 2004). This is done because there lies another mathematical possibility that the filter will become too certain of the state estimates, which will lead to the state covariance matrix to converge to zero. If this occurs, it is impossible to update the state estimates. This would lead toward infinite solutions.

The initialization of \vec{m}_{t-1}^{upd} in equation (2.6) was prescribed as

$$\vec{m}_{t=0} = \mathfrak{R}^{M \times 1} = \begin{pmatrix} 1 \\ \bar{\beta} \\ \beta_{A,j=1} \\ \beta_{B,j=1} \\ \vdots \\ \beta_{A,j=L} \\ \beta_{B,j=L} \end{pmatrix} = \begin{pmatrix} 1 \\ 0 \\ \vdots \\ 0 \end{pmatrix} \quad (2.12)$$

where M is the number of bias coefficients to be estimated and j is the harmonic number from 1 to the maximum harmonic number, L . J is currently designed to be manually assigned by the user, but can be assigned in three ways. The first is to simply assign an arbitrary number of harmonics (e.g. $L=3$ harmonics). The second approach is to use known harmonics in the flux cycle (e.g. seasonal ($k=1$), diurnal ($k=365$), etc). The final approach is to use a Fourier transform to obtain the wavenumbers associated with a particular percent of the variance with the errors between the observations and the model.

The Jacobian matrix to map from state space to observational space, \mathbf{G}_t , is assigned as

$$\mathbf{G}_t = \mathfrak{R}^{N \times M} \tag{2.13}$$

$$= \begin{pmatrix} SiB_1 & SiB_1 & SiB_1 \cos(\omega_1 1) & SiB_1 \sin(\omega_1 1) & \cdots & SiB_1 \cos(\omega_j 1) & SiB_1 \sin(\omega_j 1) \\ \vdots & \vdots & \vdots & \vdots & \vdots & \vdots & \vdots \\ SiB_N & SiB_N & SiB_N \cos(\omega_1 N) & SiB_N \sin(\omega_1 N) & \cdots & SiB_N \cos(\omega_j N) & SiB_N \sin(\omega_j N) \end{pmatrix}$$

$\omega_j = \frac{2\pi j}{N}$, where $j = 1, L$

Where N is the number of data points. For each harmonic or the mean, two corresponding time series of modeled gross flux values are multiplied by the corresponding harmonic. This allows isolation of just the mean and selected harmonic coefficients for β .

The observation vector and state covariance matrix are assigned as given by

$$\mathbf{d}_t = \mathfrak{R}^{N \times 1} = \begin{pmatrix} d_1 \\ \vdots \\ d_N \end{pmatrix} \tag{2.14}$$

$$\mathbf{C}_\beta = \mathfrak{R}^{M \times M} = \begin{pmatrix} \sigma_1^2 & 0 & \cdots & \cdots & 0 \\ 0 & \sigma_\beta^2 & 0 & \cdots & \vdots \\ \vdots & 0 & \sigma_{\beta_{A,1}}^2 & 0 & \vdots \\ \vdots & \vdots & 0 & \ddots & 0 \\ 0 & \cdots & \cdots & \cdots & \sigma_{\beta_{B,L}}^2 \end{pmatrix} \quad (2.15)$$

$$\mathbf{C}_{d,t} = \mathfrak{R}^{N \times N} = \begin{pmatrix} \sigma_{d_1}^2 & 0 & \cdots & \cdots & 0 \\ 0 & \sigma_{d_2}^2 & 0 & \cdots & \vdots \\ \vdots & 0 & \sigma_{d_3}^2 & 0 & \vdots \\ \vdots & \vdots & 0 & \ddots & 0 \\ 0 & \cdots & \cdots & \cdots & \sigma_{d_N}^2 \end{pmatrix} \quad (2.16)$$

The off-diagonal terms in the observational covariance matrix are assumed to be zero for a 1 flux observation filter (a 2-flux filter is later described). As will be explained later, this is because the individual flux uncertainty estimates used in this study were assumed to be independent of one another (Barr et al. 2013). The filter should be implemented in an algorithm summarized by the flow chart presented in Figure 2.1.

2.3. CARBON FLUX TOWER NETWORK

This study used flux records from 8 different eddy covariance (EC) towers from the FLUXNET network to comprise the observational data used in equation (2.14) of the Kalman filter. The usage of the flux tower data allowed this study to use high quality direct measurements of the component and net fluxes to well-constrain the inversion to test the hypotheses. Figure 2.2 shows the location of all the EC towers we used. A brief site summary and references to more indepth EC tower site descriptions and methods are given in Table 2.3. When choosing these sites, it was important to select towers that had complete or very near-complete (>99%) data records of NEE, RESP, and

GPP. At the lowest level of quality control, most sites have long “missing data” gaps for various reasons that make conventional statistical methods difficult to interpret with strong confidence. This study used data from the the North American Carbon Program (NACP) Site Synthesis dataset to avoid this problem.

The NACP site synthesis was a multiyear integrated research program supported designed to understand, predict, and quantify the budgets and fluxes of carbon dioxide, carbon monoxide, and methane over North America. The site synthesis was an intercomparison of 39 EC towers from the FLUXNET network simulated by 24 different land-atmosphere models from the beginning of a EC tower’s flux record until 2006, if capable.

NACP NEE, RESP, and GPP fluxes are derived from eddy covariance tower measurements using the modified FLUXNET-Canada decomposition techniques. Measured NEE was the result of summing eddy covariance and air-column storage fluxes of CO₂ integrated from 10 Hz measurements of eddy covariance measurements every 30 minutes. NEE measurements were adjusted for known energy closure issues using the Bowen Ratio and filtered for low nighttime friction velocity measurements. NEE was then regressed with temperature to derive an empirical exponential relationship applied to obtain respiration each year. When photosynthesis was possible, GPP was estimated as the difference between measured respiration and NEE, otherwise it was assumed to be zero. Missing GPP or RESP data gaps were filled by using the linear regression coefficient of a 100 point moving window between modeled and observed measurements. Please see Barr et al. (2004) for a more indepth analysis of the data preparation.

Sources of uncertainty accounted for in this dataset are from the gap-filling algorithm, random variations, threshold friction velocity and partitioning uncertainties (Schaefer et al. 2012). Random and threshold friction velocity uncertainties were estimated using the 95% confidence

interval from 1000 Monte Carlo realizations of RESP, NEE, and GPP flux estimates (Barr et al. 2013; Richardson and Hollinger 2007). The gap filling uncertainty was formulated from the standard deviation between 15 different methodologies and the fraction of filled gaps per day (Moffat et al. 2007). Partitioning uncertainty was derived from the standard deviation of 23 different partitioning methodologies and observed values (Desai et al. 2008). These uncertainties are summed in quadrature and are assumed to be uncorrelated (Schaefer et al. 2012). The estimates were provided on several timescales from half-hourly to annual estimates (Barr et al. 2013). These uncertainty estimates are used for the observational covariance matrix seen in equation (2.16).

2.4. SIMPLE BIOSPHERE MODEL 4

The land-atmosphere model fluxes were generated by the Simple Biosphere Model 4 (SiB4). SiB4 is the fourth and most advanced implementation of the biological enzyme kinetic equations originally proposed by Sellers et al. (1986). The underlying framework for SiB4 originated in second version of SiB, known as SiB2. SiB2 used the original SiB equations, but introduced new C4 photosynthesis parameterizations, improved stomatal conductance parameterizations, satellite based vegetation phenology and annual carbon flux balancing (Collatz et al. 1992; Sellers et al. 1996a, 1992; Denning et al. 1996). SiB3 updated the SiB2 framework for more modern hydrology and energy exchange parameterizations between the land surface and the atmosphere (Baker et al. 2008). The advancements from SiB3 to SiB4 presented a new framework that combined the usage of prognostic phenology, crop, and terrestrial carbon pool models to grow, senesce and turnover several flows of carbon throughout the biosphere. Figure 2.3 summarizes how SiB4 operates. Important model highlights are presented below, but refer to Haynes et al. (2013) for more technical specifics.

2.4.1. SiB4: PROGNOSTIC PHENOLOGY, CARBON POOLS, AND PLANT FUNCTIONAL TYPES

SiB4 has the capability to prognostically derive phenological quantities for vegetation in its “Prognostic Phenology” module. The framework intakes empirically derived temperature, light, and moisture factors as well as carbon stock data to diagnose both leaf area index (LAI) and the fraction of photosynthetically active radiation (fPAR) as prognostic variables. By using LAI, fPAR and other environmental stressors, SiB4 determines the magnitude of photosynthesis (Stöckli et al. 2008; Jolly et al. 2005; Stöckli et al. 2011).

Leaf-scale photosynthesis is based upon the stomatal conductance work of Collatz et al. (1992); Ball (1988) and is limited by the carboxylation enzyme kinetics of rubisco (Farquhar et al. 1980; Collatz et al. 1991). This is integrated to a bulk canopy photosynthesis flux and is regulated by the canopy air space parameterizations for ecosystem-scale balancing (Sellers et al. 1996b; Baker et al. 2008).

SiB4 operates with 11 carbon pools to simulate the cycling of carbon through the biosphere. There are 5 living carbon pools and 6 inactive carbon pools which are updated daily in the model. As SiB4 photosynthesizes, the vegetation will either respire carbon via autotrophic respiration or allocate it into the living pools for building new biomass or maintenance. The magnitude of what is allocated into a living pool depends upon the ecosystem’s phenological state and vegetation composition. Once introduced into the ecosystem as living biomass, SiB4 uses a cascading series of carbon pools each with their own turnover times and controls to limit the amount of carbon being passed through to the next stage in the series until it is released via heterotrophic respiration (Denning et al. 1996; Lokupitiya et al. 2009; Haynes et al. 2013).

Total respiration in SiB4 is formulated from autotrophic and heterotrophic respiration between the plant and surface carbon pools (Denning et al. 1996). Respiration in SiB4 is a function of soil

moisture, soil temperature, and carbon pool size. The autotrophic respiration parameterizations are applied to the live carbon pools. The heterotrophic respiration parameterizations are applied to the surface and soil pools. Every year the gross annual photosynthetic production is balanced by the total respiration for a net-zero annual carbon flux budget.

SiB4 uses 25 plant functional types (PFT) unlike previous versions used that 15 IGBP Biome classifications of ecosystems. As seen in Table 2.4, SiB4 implements 1 desert, 8 forest, 3 shrublands, 5 grasslands, and 7 crops PFT types. These are distinguished by vegetation characteristics and climate regimes. Using PFTs over Biomes allows SiB4 to more accurately describe the phenological characteristics of an ecosystem. Beyond this, SiB4 also has the capability of making a multi-PFT grid cell that can represent a mosaic of land heterogeneity, which is more representative of real vegetation cover (Bonan et al. 2002).

SiB4 was run as a single point centered directly over a selected EC tower's location. SiB4 requires look-up tables for vegetation phenology, physiology, and carbon pool to initialize and calculate various biological quantities. The driver meteorology supplied to SiB4 was from the MERRA .5° by .5° gridded reanalysis dataset over the observed record. Additionally, a spin-up model run was required to bring the carbon pools to equilibrium before a forward simulation. The spin-up model run was no more than 7 iterations of the observed length of record. Once the carbon pools reached equilibrium, SiB4 was run forward over the observed record. Model flux output was then stored for analysis.

2.5. EXPERIMENTAL DESIGN

The hypotheses are tested by means of three by means of three different experiments involving both the time smoothing and a control algorithm. These experiments were designed to evaluate the time smoothing algorithm in ways that mimic past, present, and future applications of bias

estimates. As shown in Table 2.5, the estimates created from these experiments are used to address the hypotheses outlined in section 1.2. Furthermore, a summary of the experimental set-ups and tests between the control and time smoothing algorithms are seen in Table 2.6.

The control algorithm used in all three experiments to estimate NEE is analogous to an inversion algorithm that is currently employed by modern inversion models. The control algorithm updates a single bias coefficient estimates of NEE every week. The *a posteriori* bias coefficients and state covariance matrix are estimated once and are not used as *a priori* information for future assimilation cycles. That is, the control algorithm used new initializations of the bias coefficients and state covariance matrix every assimilation cycle. Thus, the control algorithm estimates 52 separate and independent single bias coefficients of NEE in a year. A control algorithm formulated in this manner has been shown to be highly useful for estimating week-to-week variations in CO₂, but may be unable to properly match the yearly and annual cycles of CO₂ (CarbonTracker 2014).

2.5.1. EXPERIMENT 1: NEE OPTIMIZED FROM NEE

The first experiment is an “apples-to-apples” comparison of the estimation of the mean and seasonal errors of modeled NEE given direct measurements of NEE. This is analogous to estimating NEE from CO₂ in a conventional atmospheric inversion because only NEE changes the concentrations of atmospheric CO₂. The equations used by the control and time-smoothing algorithms in Experiment 1 are given by

$$NEE_{obs,control}(t) = [1 + \beta_{NEE}(t)] NEE_{model}(t) + \epsilon \quad (2.17)$$

$$NEE_{obs,TS}(t) = \left[1 + \bar{\beta} + \sum_{k=1}^L (\beta_{A,k} \cos \omega_k t + \beta_{B,k} \sin \omega_k t) \right] NEE_{model}(t) + \epsilon \quad (2.18)$$

Both algorithms used the same initial conditions and Kalman filter equations. The initial bias uncertainty was set to .9 for all parameters ($\sigma_\beta = .9$) and was inflated during the update step with a weighting factor of 0.4 ($w = 0.4$). The observational uncertainty was prescribed from Barr et al. (2013) and updated for each assimilation cycle.

Once each algorithm was applied using the prescribed condition, additional tests were run using various amounts of uncertainty in both β and the observations. Since atmospheric inversions have problems with dilution and wind advection of the NEE signal, flux towers provide much stronger observational constraint. It is reasonable to assume that if the findings of this study were applied to a full scale atmospheric inversion, then the tests of the observational certainty must be done to extrapolate observational uncertainty estimates toward global scale uncertainty values. To do this, this experiment applied increased observational uncertainties of 2, 5, and 10 times the given observational uncertainty estimates from Barr et al. (2013).

2.5.2. EXPERIMENT 2: GPP AND RESP OPTIMIZED FROM NEE

The second experiment attempts to use the GPP and RESP fluxes to formulate a NEE estimate, which is then optimized by observed NEE. This experiment is similar to previous studies by Zupanski et al. (2007), Lokupitiya et al. (2008), and Schuh et al. (2009, 2010, 2013). Like the first experiment, NEE is still being optimized by observed NEE, however the bias coefficient estimates are now representative of the adjustments for flux patterns in GPP and RESP, not NEE. The control algorithm remained composed from equation (2.17), but the time smoothing algorithm was updated to optimize equation (2.19).

$$NEE_{obs,TS}(t) = \left[1 + \bar{\beta}_{RE} + \sum_{k=1}^L (\beta_{RE,A,k} \cos \omega_k i + \beta_{RE,B,k} \sin \omega_k i) \right] RESP_{model}(t)$$

$$- \left[1 + \bar{\beta}_{GPP} + \sum_{k=1}^L (\beta_{GPP,A,k} \cos \omega_k i + \beta_{GPP,B,k} \sin \omega_k i) \right] GPP_{model}(t) + \epsilon \quad (2.19)$$

When solving for both β_{GPP} and β_{RESP} at the same time using NEE state estimation, reformulation of the \mathbf{G}_t , $\vec{m}_{t=0}$, and \mathbf{C}_β matrices was needed. These vectors and matrices are changed via equations (2.20) through (2.22) and were substituted into the Kalman filter accordingly.

$$\vec{m}_{t=0} = \mathfrak{R}^{2M \times 1} = \begin{pmatrix} 1 \\ \bar{\beta}_{RESP} \\ \beta_{RESP,A,1} \\ \beta_{RESP,B,1} \\ \vdots \\ \beta_{RESP,A,L} \\ \beta_{RESP,B,L} \\ 1 \\ \bar{\beta}_{GPP} \\ \beta_{GPP,A,1} \\ \beta_{GPP,B,1} \\ \vdots \\ \beta_{GPP,A,L} \\ \beta_{GPP,B,L} \end{pmatrix} = \begin{pmatrix} 1 \\ 0 \\ \vdots \\ 0 \\ 1 \\ 0 \\ \vdots \\ 0 \end{pmatrix} \quad (2.20)$$

$$\mathbf{G}_t = \mathfrak{R}^{N \times 2M}$$

$$= \begin{pmatrix} SiB_{R,1} & \dots & SiB_{R,1} \sin(\omega_k 1) & -SiB_{G,1} & \dots & -SiB_{G,1} \sin(\omega_k 1) \\ \vdots & \vdots & \vdots & \vdots & \vdots & \vdots \\ SiB_{R,N} & \dots & SiB_{R,N} \sin(\omega_k N) & -SiB_{G,N} & \dots & -SiB_{G,N} \sin(\omega_k N) \end{pmatrix} \quad (2.21)$$

$$\mathbf{C}_\beta = \mathfrak{R}^{2M \times 2M}$$

$$= \begin{pmatrix} \sigma_{1,RESP}^2 & 0 & \dots & \dots & \dots & \dots & \dots & 0 \\ 0 & \sigma_{\bar{\beta}_{RESP}}^2 & 0 & \dots & \dots & \dots & \dots & \vdots \\ \vdots & 0 & \sigma_{\beta_{RESP,A,1}}^2 & 0 & \dots & \dots & \dots & \vdots \\ \vdots & \vdots & 0 & \ddots & \dots & \dots & \dots & \vdots \\ \vdots & \dots & \dots & 0 & \sigma_{\beta_{RESP,B,L}}^2 & 0 & \dots & \vdots \\ \vdots & \dots & \dots & \dots & 0 & \sigma_{1,GPP}^2 & 0 & \vdots \\ \vdots & \dots & \dots & \dots & \dots & 0 & \ddots & 0 \\ 0 & \dots & \dots & \dots & \dots & \dots & 0 & \sigma_{\beta_{GPP,B,L}}^2 \end{pmatrix} \quad (2.22)$$

The initial bias coefficient uncertainty was set to .9 for all parameters ($\sigma_\beta = .9$) and was inflated during the update step with a weighting factor of 0.4 ($w=0.4$). After optimization, GPP and RESP fluxes were reconstructed for hypothesis and significance testing given by

$$RESP_{est,TS}(t) = \left[1 + \bar{\beta}_{RE} + \sum_{k=1}^L (\beta_{RE,A,k} \cos \omega_k i + \beta_{RE,B,k} \sin \omega_k i) \right] RESP_{model}(t) + \epsilon \quad (2.23)$$

$$GPP_{est,TS}(t) = \left[1 + \bar{\beta}_{GPP} + \sum_{k=1}^L (\beta_{GPP,A,k} \cos \omega_k i + \beta_{GPP,B,k} \sin \omega_k i) \right] GPP_{model}(t) + \epsilon \quad (2.24)$$

Like Experiment 1, once each algorithm was tested using the prescribed conditions, increased observational uncertainties of 2, 5, and 10 times the given the uncertainty estimates from Barr et al. (2013) were used to test limits of each algorithm's performance.

2.5.3. EXPERIMENT 3: RESP AND GPP OPTIMIZED FROM NEE AND GPP

The third experiment is analogous to an inversion where additional observational data such as GPP or RESP are able to constrain one of the two component fluxes. With the advent of more advanced carbon observing satellites like GOSAT and OCO-2, these satellite products are more likely to be used in the future to help constrain inversion estimates. This experiment replicates the uncertainty tests of the first two experiment, but this time uses both observed NEE and GPP fluxes to estimate the bias coefficients of modeled GPP and NEE. The control algorithm remained composed from equation (2.17). The time smoothing algorithm was updated to use equations (2.24) and (2.18) in tandem for prior estimates of GPP and NEE. Since the three fluxes are intimately connected, this experiment should not only optimize NEE and GPP, but also optimize RESP. The Kalman filter algorithm was updated with $\vec{m}_{t=0}$ and \mathbf{C}_β matrices from equations (2.20) and (2.22). The vectors and matrices \mathbf{d}_t , \mathbf{G}_t , and $\mathbf{C}_{d,t}$ are updated to equations (2.25) through (2.27).

$$\mathbf{d}_t = \mathfrak{R}^{2N \times 1} = \begin{pmatrix} d_{NEE,1} \\ \vdots \\ d_{NEE,N} \\ d_{GPP,1} \\ \vdots \\ d_{GPP,N} \end{pmatrix} \quad (2.25)$$

$$\mathbf{G}_t = \mathfrak{R}^{2N \times 2M} = \begin{pmatrix} SiB_{R,1} & \dots & SiB_{R,1} \sin(\omega_k 1) & -SiB_{G,1} & \dots & -SiB_{G,1} \sin(\omega_k 1) \\ \vdots & \vdots & \vdots & \vdots & \vdots & \vdots \\ SiB_{R,N} & \dots & SiB_{R,N} \sin(\omega_k N) & -SiB_{G,N} & \dots & -SiB_{G,N} \sin(\omega_k N) \\ 0 & 0 & 0 & SiB_{G,1} & \dots & SiB_{G,1} \sin(\omega_k 1) \\ \vdots & \vdots & \vdots & \vdots & \vdots & \vdots \\ 0 & 0 & 0 & SiB_{G,N} & \dots & SiB_{G,N} \sin(\omega_k N) \end{pmatrix} \quad (2.26)$$

$$\mathbf{C}_{d,t} = \mathfrak{R}^{2N \times 2N} = \begin{pmatrix} \sigma_{d_{NEE,1}}^2 & 0 & \dots & \sigma_{d_{NEE,GPP,1}}^2 & \dots & 0 \\ 0 & \ddots & 0 & \dots & \dots & \vdots \\ \vdots & 0 & \sigma_{d_{NEE,N}}^2 & 0 & \dots & \sigma_{d_{NEE,GPP,N}}^2 \\ \sigma_{d_{GPP,NEE,1}}^2 & \dots & 0 & \sigma_{d_{GPP,1}}^2 & 0 & \vdots \\ \vdots & \dots & \dots & 0 & \ddots & 0 \\ 0 & \dots & \sigma_{d_{GPP,NEE,N}}^2 & \dots & 0 & \sigma_{d_{GPP,N}}^2 \end{pmatrix} \quad (2.27)$$

As can be seen in equation (2.27), the observational covariance matrix now has off-diagonal elements to communicate covarying uncertainty between day-to-day uncertainty estimates between GPP and NEE. This was not part of the original uncertainty estimates provided, but it was found that there are issues when assuming zero value off-diagonal covariances in this version of the assimilation algorithm. Since the observational uncertainty estimates were assumed to be independent and uncorrelated on a day-to-day basis of a singular flux, it can be assumed that there is still

some covariance between the net and component fluxes. Therefore, the estimate the daily observational covariance uncertainty between net and the component flux can be found by summing the corresponding flux uncertainty estimates in quadrature. The uncertainty covariance ($\sigma_{NEE,GPP,obs}^2$) for any particular day was given by

$$\sigma_{NEE,GPP,obs}^2 = \frac{\sigma_{NEE,obs}^2 - \sigma_{GPP,obs}^2}{2} \quad (2.28)$$

2.6. HYPOTHESES TESTING AND SIGNIFICANCE

As stated in section 1.2, there are eight hypotheses being tested by the time smoothing algorithm in this study. Once the data was prepared in one of the experiments in section 2.5, this study then administered a possible five step evaluation to provide visual, qualitative, and quantitative evidence of the time smoothing algorithms fit. NEE estimates were evaluated against the control and time smoothing algorithms. The component fluxes were solely evaluated against observations as the control algorithm did not provide component flux estimates. The suite of tests run on various hypotheses are outlined in table 2.7. Full elaboration of these methods are explained in this section.

2.6.1. ANNUAL AVERAGES

This study employed equations (2.29) and (2.30) from the update step of the optimization as both a visual and qualitative evaluation the annual average, interannual pattern, and associated uncertainty in a particular year.

$$\overline{NEE}_{posterior} = \vec{k}_m \mathbf{G}_t \vec{\eta}_t^{upd} \quad (2.29)$$

$$\sigma_{NEE_{posterior}}^2 = \vec{k}_m^T \mathbf{G}_t^T \mathbf{C}_{\beta,t}^{upd} \mathbf{G}_t \vec{k}_m \quad (2.30)$$

$$\vec{k}_m = \mathfrak{R}^{1 \times N} = \left(\begin{array}{cccc} \frac{1}{365} & \frac{1}{365} & \dots & \frac{1}{365} \end{array} \right) \quad (2.31)$$

These are applied to the observational, time smoothing and control algorithms, if applicable.

2.6.2. FRACTIONAL ROOT MEAN SQUARE ERROR REDUCTION

Another visual, but more quantitative test to suggest whether the mean and variance of the error between the observations and model flux estimate has been lowered was a fractional root mean square error (RMSE) reduction test. This test is similar to the one used in Schuh et al. (2009) and follows equation (2.32).

$$\text{Fractional Reduction of RMSE} = 1 - \frac{RMSE_{posterior}}{RMSE_{prior}} \quad (2.32)$$

Here the RMSE is determined on an annual basis between the observations and the pre-assimilation flux estimate or the post-assimilation flux estimate. The conclusions are given by

$$\text{Conclusion} = \begin{cases} RMSE_{posterior} < RMSE_{prior}, & \text{if } 0 < \text{Fractional Reduction of RMSE} \leq 1 \\ RMSE_{posterior} = RMSE_{prior}, & \text{if Fractional Reduction of RMSE} = 0 \\ RMSE_{posterior} > RMSE_{prior}, & \text{if Fractional Reduction of RMSE} < 0 \end{cases} \quad (2.33)$$

This test can be used as an indication that the post-assimilation flux estimates are better than that of the pre-assimilation, control or other algorithm variant's flux estimates. However, this method does not give statistical confidence and was for qualitative use.

2.6.3. ERROR AUTOCORRELATION AND CROSS-CORRELATION

A more rigorous statistical test of the interannual mean and seasonal cycles was administered according to the reduction of the error between the observed flux and the corresponding optimized

fit. Given below are examples of the difference in *a posteriori* estimates of NEE from the control or time smoothing algorithms and the observations.

$$\Delta NEE_{Obs-TF}(t) = NEE_{Obs}(t) - NEE_{TF,est}(t) \quad (2.34)$$

$$\Delta NEE_{Obs-Control}(t) = NEE_{Obs}(t) - NEE_{Control,est}(t) \quad (2.35)$$

The first evaluation was to see if these two error time series are correlated or independent and identically distributed (IID). This was evaluated by the cross-correlation across a number of lags (τ). An example of the cross-correlation function when $\Delta NEE_{Obs-Control}$ lags ΔNEE_{Obs-TF} is given by

$$r_{\Delta NEE_{Obs-Control}, \Delta NEE_{Obs-TF}}(\tau) = \frac{\sum_{i=1+\tau}^N [(\Delta NEE_{Obs-Control}(i)' \Delta NEE_{Obs-TF}(i - \tau)')]}{\sigma_{\Delta NEE_{Obs-Control}} \sigma_{\Delta NEE_{Obs-TF}}} \quad (2.36)$$

$$\Delta NEE_{Obs-Control}(i)' = \Delta NEE_{Obs-Control}(i) - \overline{\Delta NEE}_{Obs-Control}(i) \quad (2.37)$$

$$\Delta NEE_{Obs-TF}(i - \tau)' = \Delta NEE_{Obs-TF}(i - \tau) - \overline{\Delta NEE}_{Obs-TF}(i) \quad (2.38)$$

An example of the null and alternative hypotheses for the cross-correlation function in (2.36) are given by

$$H_o : r_{\Delta NEE_{Obs-Control}, \Delta NEE_{Obs-TF}}(\tau) = 0 \quad (2.39)$$

$$H_a : r_{\Delta NEE_{Obs-Control}, \Delta NEE_{Obs-TF}}(\tau) \neq 0 \quad (2.40)$$

If the errors of the fits are correlated in some way, the correlation coefficient of a particular lag will exceed a critical certainty bounds defined by a critical t-statistic at the 95th percentile adjusted by

the Bonferroni correction as defined below

$$C_{bound} = \pm \frac{t_{crit, \frac{\alpha}{2N}}}{\sqrt{N}} \quad (2.41)$$

$$\alpha = 0.05$$

In equation (2.42), the autocorrelation function of the error time series was used to detect white noise as the remaining signal of the error time series.

$$r_{\Delta NEE, \Delta NEE}(\tau) = \frac{\sum_{i=1+\tau}^N [(\Delta NEE(i)' \Delta NEE(i - \tau)')]}{\sigma_{\Delta NEE}^2} \quad (2.42)$$

Example residuals, $\Delta NEE(i)'$ and $\Delta NEE(i - \tau)'$, are defined in equations (2.37) and (2.38).

If the autocorrelation function is approximately 0 across all lags, then it can be assumed the error time series is white noise. Therefore, the autocorrelation functions of the error time series were evaluated by the example hypothesis tests given below

$$H_o : r_{\Delta NEE, \Delta NEE}(\tau) = 0 \quad (2.43)$$

$$H_a : r_{\Delta NEE, \Delta NEE}(\tau) \neq 0 \quad (2.44)$$

These hypotheses were evaluated against the same certainty bounds in equation (2.41).

2.6.4. PAIRED T-TEST

The direct evaluation of the annual averages was based on the results of a the paired T-test. In the event that the cross-correlation suggested that the error time series of NEE may be slightly correlated above the confidence bound, the assumption of normality of the annual averages still seems reasonable as the length of the time series is always much greater than 30. An example of

the paired T-test for NEE is seen below

$$t_{score} = \frac{\frac{1}{N} \sum_{t=1}^N (\Delta NEE_{Obs-TF}(t) - \Delta NEE_{Obs-Control}(t))}{\sqrt{\frac{\sigma_{TF-Control}^2}{N_{TF-Control}}}} \quad (2.45)$$

$$|t_{score}| > |t_{crit, 1-\alpha, N_{TF-Control}-1}|$$

$$p_{value} < \alpha, \alpha = 0.05$$

Example null and alternative hypotheses being tested for NEE in this step are given below

$$H_o : \overline{\Delta NEE_{Obs-TF}} \geq \overline{\Delta NEE_{Obs-Control}} \quad (2.46)$$

$$H_a : \overline{\Delta NEE_{Obs-TF}} < \overline{\Delta NEE_{Obs-Control}} \quad (2.47)$$

The T-test and hypotheses being tested for GPP and RESP in this step are given by

$$H_o : \overline{(GPP/RESP)_{TF}} = \overline{(GPP/RESP)_{Control}} \quad (2.48)$$

$$H_a : \overline{(GPP/RESP)_{TF}} \neq \overline{(GPP/RESP)_{Control}} \quad (2.49)$$

$$t_{score} = \frac{\frac{1}{N} \sum_{t=1}^N ((GPP/RESP)_{TF}(t) - (GPP/RESP)_{Obs}(t))}{\sqrt{\frac{\sigma_{TF-Obs}^2}{N_{TF-Obs}}}} \quad (2.50)$$

$$|t_{score}| > |t_{crit, 1-\frac{\alpha}{2}, N_{TF-Control}-1}|$$

$$p_{value} < \frac{\alpha}{2}, \alpha = 0.05$$

If the paired T-test was able to reject the null hypothesis, then it can be assumed that the mean error between the time smoothing algorithm and the observations was equal or lower than the mean error between the control algorithm and observations.

2.6.5. LJUNG-BOX TEST

If the autocorrelation function of an error time series was found to be within the bounds to suggest the presence of white noise, then a Ljung-Box test was used to confirm or deny only white noise remains in the error time series (Ljung and Box 1978). The Ljung-Box test of the autocorrelation function is given as

$$Q = N(N + 2) \sum_{\tau=1}^H \frac{r_{\tau}}{N - \tau} \quad (2.51)$$

$$Q > \chi_{1-\alpha, H}^2$$

$$p_{value} < \alpha, \alpha = 0.05$$

where H is the number of lags, Q is the Q-score, and $\chi_{1-\alpha, H}^2$ is the χ^2 value at the α -quantile of H number of lags. The hypothesis test being evaluated of the Ljung-Box test at the 95th quantile is shown below

$$H_o : \text{The data are independent as a result of white noise} \quad (2.52)$$

$$H_a : \text{The data are not independent and display some sort of correlation} \quad (2.53)$$

If the null hypotheses of this test was retained then it can be assumed that both the annual mean and seasonal cycle were well-fitted.

2.6.6. MEAN POWER SPECTRUM

If both the autocorrelation and Ljung-Box tests suggest there was the presence of some correlation in the error time series, then the conclusions of a well-fitted seasonal cycle may not be dismissed as other unresolved biases may still exist. A mean power spectrum was used to identify

which parts of the error time series signal were being unresolved. The number of spectral estimates that formulated the mean power spectrum are given by

$$M_{ch} = 2N_{years} - 1 \quad (2.54)$$

where N_{years} is the number of year in the time series and M_{ch} is the number of spectral estimates. Furthermore, a Kaiser window filter was applied to the time series over a window length of 365 days to provide one spectral estimate. The usage of a Kaiser window was preferred since it can mimic the spectral qualities many other window filters, but gives the utility of manual window shape parameter adjustment, γ . The Kaiser window is given by

$$w(t) = \begin{cases} 0 & -\frac{N_{days}-1}{2} > t \\ I_0 \frac{\left(\gamma \sqrt{1 - \frac{4t^2}{(N_{days}-1)^2}} \right)}{I_0(\gamma)} & -\frac{N_{days}-1}{2} \leq t \leq \frac{N_{days}-1}{2} \\ 0 & t > \frac{N_{days}-1}{2} \end{cases} \quad (2.55)$$

$$\gamma = 14, N_{days} = 365$$

where I_0 is the zeroth order Modified Bessel Function. Since the window tapers off giving only maximum representation to a minimal number of actual points in the power spectrum, every spectral estimate began at every half year. This means the final year of a time series will only have half of its data fully represented. This should not cause any misinterpretation given a substantial number of spectral estimates to statistically make a claim about the hypotheses.

The power spectrum of each estimate was then computed and averaged together to make the mean power spectrum using the equation below

$$\bar{\phi}(\omega) = \frac{\sum_{i=1}^{M_{ch}} \phi_i(\omega)}{M_{ch}} \quad (2.56)$$

where ω is a particular frequency and i is the i^{th} spectral estimate. The mean power spectrum is then evaluated against the corresponding red noise spectrum and critical red noise spectrum in given below

$$\phi_{red}(\omega) = \frac{2T}{1 + T^2\omega^2} \quad (2.57)$$

$$\phi_{red,crit}(\omega) = F_{crit,\alpha,2N_{years},N_{days}} \phi_{red} \quad (2.58)$$

$$T = -\frac{1}{\ln(r_{\tau=1})}$$

$$\alpha = 0.05$$

where T is the e-folding timescale of the red noise spectrum based on the lag-1 autocorrelation of the error time series. If the particular power of a wavenumber, k , is greater than the critical red noise time series, then this particular harmonic indicates an important signal unresolved by the optimization. The seasonal signal was be evaluated against the hypotheses below

$$H_o : \bar{\phi}(\omega)_{k=1} \geq \phi(\omega)_{red,crit,k=1} \quad (2.59)$$

$$H_a : \bar{\phi}(\omega)_{k=1} < \phi(\omega)_{red,crit,k=1} \quad (2.60)$$

If the first wavenumber is less than the critical red noise spectrum, then the assumption can be made that there was modest fit of the seasonal cycle from either a variant of the time smoothing algorithm or the control algorithm.

TABLE 2.1. Possible sources of bias in SiB4

	GPP	RESP
$\bar{\beta}$	fPAR or V_{max}	Soil Pool Turnover Times ($\tau_{soil\ pools}$)
β'	Growing Degree Days or Soil Moisture	Temperature Sensitivity (Q^{10})

TABLE 2.2. Variables present in equations (2.6) through (2.11). All variables are given at a current assimilation time (t).

Variable Name	Definition
\vec{m}_t^{pre}	Predicted state estimate
\vec{m}_t^{true}	True value of state
\vec{m}_t^{upd}	<i>A posteriori</i> state estimate
\mathbf{d}_t	Vector of observations
\mathbf{A}_{t-1}	State transition matrix
μ_t	White noise error in the state between assimilation times
$\mathbf{C}_{\beta,t}^{pre}$	Predicted state covariance matrix
$\mathbf{C}_{\beta,t}^{upd}$	<i>A posteriori</i> state covariance matrix
\mathbf{K}_t	Kalman Gain matrix
\mathbf{G}_t	State to observational space Jacobian at current assimilation time
\mathbf{I}	Identity matrix
w	Inflation parameter to prevent state covariance collapse

TABLE 2.3. Observational Site Descriptions

Site Name (Site Code)	Latitude Longitude	PFT Type	Years Used	PI	Site References
Lethbridge (CA-Let)	49.709 -112.940	C3 grass	2000-2006	Lawrence Flanagan	(Flanagan and Adkinson 2011)
Campbell River (CA-Ca1)	49.867 -125.333	ENF	1998-2006	Andrew T. Black	(Krishnan et al. 2009)
U. of Mich. Biolo. Station (US-UMB)	45.559 -84.713	DBF	2004-2006	Gil Bohrer	(Gough et al. 2008)
Vaira Ranch (US-Var)	38.406 -120.950	C3 grass	2001-2007	Dennis Baldocchi	(Ma et al. 2007)
Mead-Irrigated (US-Ne1)	41.165 -96.476	Maize/Soy Wheat	2002-2012	Andrew E. Suyker	(Verma et al. 2005) (Suyker and Verma 2010)
Harvard Forest (US-Ha1)	42.537 -72.171	DBF	1997-2004	Bill Munger	(Urbanski et al. 2007)
ARM-Oklahoma SGP Main (US-ARM)	36.605/ -97.488	Maize/Soy Wheat	2003-2006	Marc Fischer	(Fischer et al. 2007)
Old Black Spruce (CA-Obs)	53.987 -105.118	ENF	2000-2006	Andrew T. Black	(Krishnan et al. 2008) (Kljun et al. 2006)

TABLE 2.4. Description of PFTs present in SiB4

PFT Number	PFT Code	PFT Description
1	des.all	Desert
2	enf.tem	Temperate Evergreen Needleleaf Forest
3	enf.bor	Boreal Evergreen Needleleaf Forest
4	dnf.bor	Boreal Deciduous Needleleaf Forest
5	ebf.tro	Tropical Evergreen Broadleaf Forest
6	ebf.tem	Temperate Evergreen Broadleaf Forest
7	dbf.tro	Tropical Deciduous Broadleaf Forest
8	dbf.tem	Temperate Deciduous Broadleaf Forest
9	dbf.bor	Boreal Deciduous Broadleaf Forest
10	ebs.tro	Tropical Evergreen Broadleaf Shrub
11	dbs.tem	Temperate Deciduous Broadleaf Shrub
12	dbs.bor	Boreal Deciduous Broadleaf Shrub
13	c3g.tro	Tropical C3 Grass
14	c3g.tem	Temperate C3 Grass
15	c3g.bor	Boreal C3 Grass
16	c4g.tro	Tropical C4 Grass
17	c4g.tem	Temperate C4 Grass
18	cro.tro	Tropical Generic Crop
19	cro.tem	Temperate Generic Crop
20	mze.tro	Tropical Maize Crop
21	mze.tem	Temperate Maize Crop
22	soy.tro	Tropical Soy Crop
23	soy.tem	Temperate Soy Crop
24	wwt.tem	Temperate Winter Wheat Crop
25	misc.tem	Temperate Miscanthus

TABLE 2.5. Experiments used to explore the hypotheses outlined in section 1.2

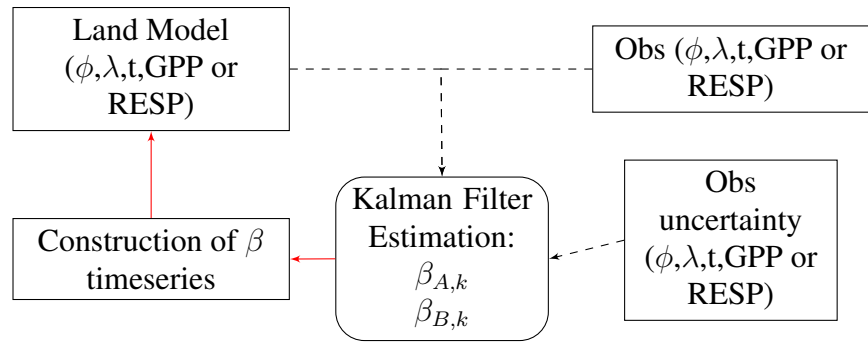
	Experiment 1	Experiment 2	Experiment 3
Hypothesis 1	✓	-	-
Hypothesis 2	✓	-	-
Hypothesis 3	-	✓	-
Hypothesis 4	-	✓	-
Hypothesis 5	-	✓	-
Hypothesis 6	-	-	✓
Hypothesis 7	-	-	✓
Hypothesis 8	-	-	✓

TABLE 2.6. Set-up of variables and tests for Experiment 1, 2, and 3

	Time Smoothing	Control
Experiment 1: Variable(s) Optimized	NEE	NEE
Experiment 2: Variable(s) Optimized	NEE	NEE
Experiment 3: Variable(s) Optimized	NEE and GPP	NEE
Experiment 1: Variable(s) Used	NEE	NEE
Experiment 2: Variable(s) Used	GPP and RESP	NEE
Experiment 3: Variable(s) Used	GPP and RESP	NEE
Number of harmonics (L)	5	N/A
Experiment 1: Number of Parameters Optimized	11	52
Experiment 2: Number of Parameters Optimized	22	52
Experiment 3: Number of Parameters Optimized	22	52
Observational Uncertainty	(Barr et al. 2013)	(Barr et al. 2013)
Observational Uncertainty Tests	2x, 5x, 10x	2x, 5x, 10x
Initial β Uncertainty	.9	.9
Tuning Parameter (w)	0.4	0

TABLE 2.7. The methods that will be employed to statistically verify the hypotheses outlined in section 1.2

	Annual Mean	RMSE Test	Paired T-test	Cross/Autocor	Ljung-Box Test	Φ Spectrum
$\overline{NEE}_{TF} \leq \overline{NEE}_{Control}$	✓	✓	✓	-	-	-
$\overline{GPP}_{TF} = \overline{GPP}_{Obs}$	✓	✓	✓	-	-	✓
$\overline{RESP}_{TF} = \overline{RESP}_{Obs}$	✓	✓	✓	-	-	✓
$NEE_{TF,seas} = NEE_{Control,seas}$	-	-	-	✓	✓	✓
$GPP_{TF,seas} = GPP_{Obs,seas}$	-	-	-	✓	✓	✓
$RESP_{TF,seas} = RESP_{Obs,seas}$	-	-	-	✓	✓	✓
Observational Uncertainty Tests	✓	-	-	-	-	-



Line Color Definitions

- : β destination for next SiB4 run
- - -: Raw data input

FIG. 2.1. Kalman Filter estimation procedure. Shown is one assimilation cycle.

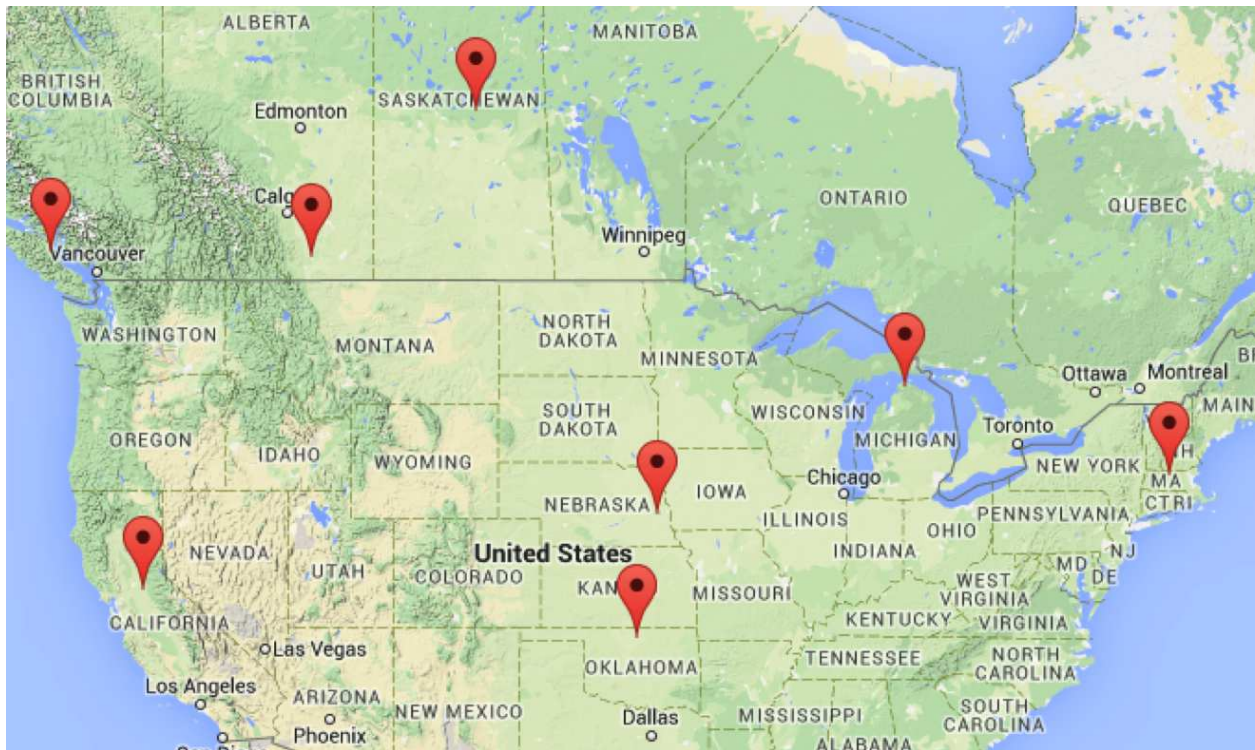


FIG. 2.2. Map of tower sites used in this study. Created using Google Maps.

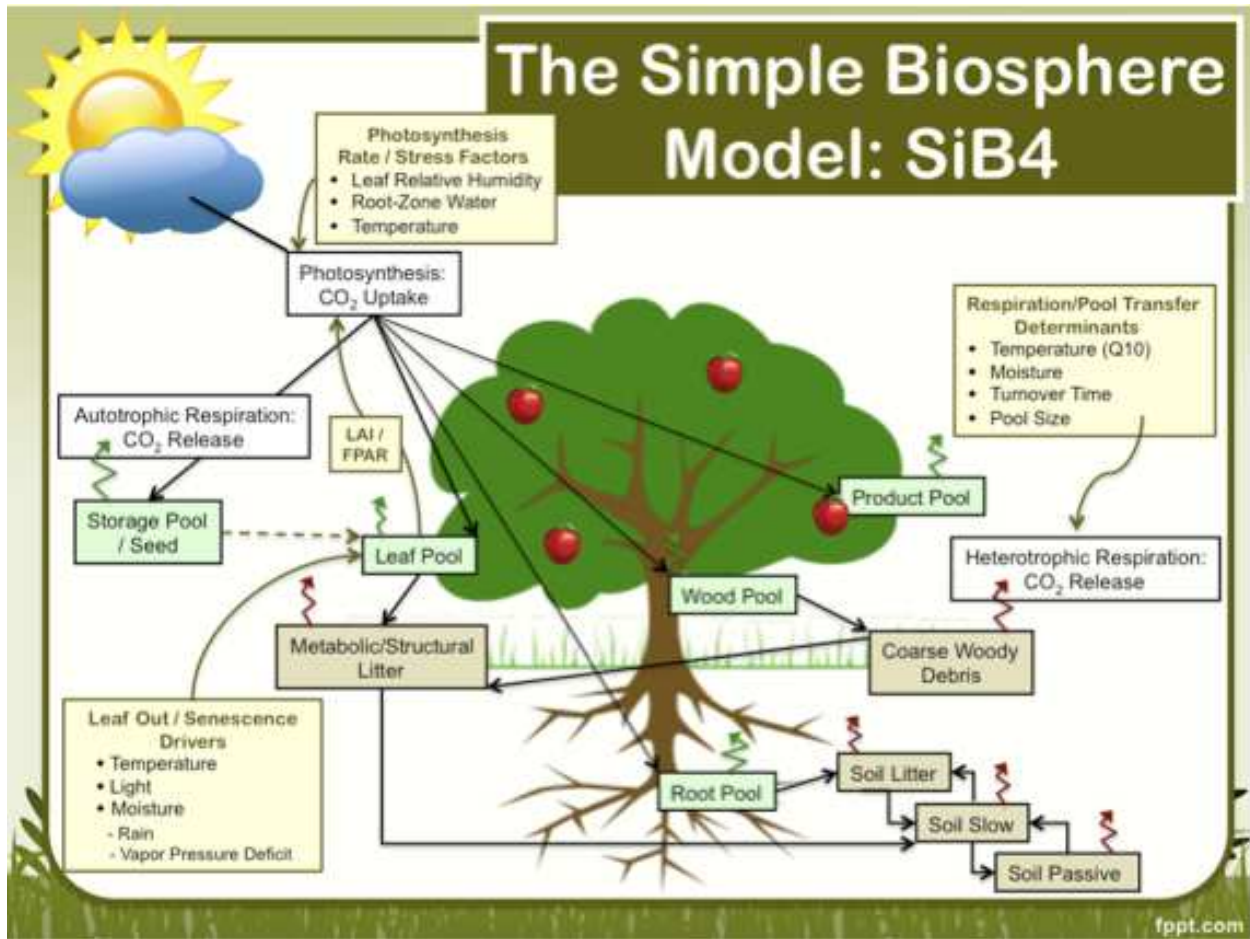


FIG. 2.3. Shown is a representation of how SiB4 treats the cycling of carbon. Figure is courtesy of Haynes et al. (2013).

CHAPTER 3

RESULTS

3.1. HOW MANY HARMONICS ARE NECESSARY?

Shown in Figure 3.1 is the percent variance explained by harmonics from the averaged power spectrum of the normalized flux errors at three different ecosystems and climate regimes. The three ecosystems show that at least 60% of the error variance explained is between the first 3 to 6 harmonics of any gross flux and decreases to 0 to 2% for the remaining harmonics. This suggests that the errors between the model and observations are the most persistent for the slowest of timescales.

It is worth mentioning that there should be a discrepancy between the realistic number of harmonics needed to optimize for just NEE alone and the number of harmonics needed to optimize for NEE when using the component fluxes. This is because when optimizing using two contrasting component fluxes that vary differently than the net flux, the result will be short rapid variations in the net flux. As a general rule for this methodology, use the number significant harmonics to resolve the largest variance explained without being too computationally expensive. If the algorithm is optimizing NEE using RESP and GPP, then the highest number of significant harmonics between GPP and RESP should be used. An example of this would be in the deciduous broadleaf forest where only need 3 harmonics to optimize for NEE alone, but 6 harmonics to optimize NEE using GPP and RESP. As a result, Figure 3.1 shows that the choice of 3 to 6 harmonics is justified for the optimization process.

3.2. EXPERIMENT 1

The purpose of the first experiment was to evaluate the time smoothing algorithm against the control algorithm using only observed the NEE flux to optimize for the modeled NEE flux. As stated in the methods, the algorithm optimizes for 12 bias coefficients and uses a portion of both the posterior and prior bias coefficient covariance matrix estimates rather than the 52 independent weekly bias coefficients. Table 3.1 shows the results of all statistical significance tests done to the optimizations of the first experiment and whether or not the statistical hypothesis tests were confirmed or denied.

3.2.1. EXPERIMENT 1: NEE ESTIMATES AND RMSE REDUCTION

The first experiment only produced estimates of the NEE model bias from assimilated NEE observations. Figure 3.2 shows the daily estimations of NEE from both the control and the time smoothing algorithms. These algorithms both show good estimation of both the seasonal and annual cycles of NEE for both Harvard Forest and Vaira Ranch across all years. Closer examination of the visual fits show that the control algorithm appears to be better at estimating the faster time variations and the time smoothing algorithm is better at obtaining the slower time variations of the observations. This same result was seen across all 8 sites. The goodness of these estimations is incapable of being diagnosed just from this visual comparison and so more rigorous testing is needed.

The first test was the reduction of the RMSE between the prior and posterior estimates of NEE. The top panel of Figure 3.3 shows the annual RMSE reduction between the control and time smoothing algorithms across all 8 sites. Visually, this test demonstrates that in most circumstances the reduction of RMSE of NEE for the time smoothing algorithm is as good or worse than the control. An example of the control algorithm outperformance over the time smoothing

algorithm is seen at Harvard Forest. This site only experienced a reduction between .19 and .2 for the time smoothing algorithm, while the control demonstrated a reduction between .22 and .32. These results suggest that either the annual means or variance may be underestimated by the time smoothing algorithm.

3.2.2. EXPERIMENT 1: ANNUAL SOURCES AND SINKS

Examination of the annual mean estimates gives way to supporting the results of the RMSE reductions and the overarching hypotheses. Example annual CO₂ sources and sinks under increasing amounts of observational uncertainty from the first experiment are seen in Figure 3.5 for Harvard Forest and Vaira Ranch. In the top left panel of these figures, the standard optimization using no variations in observational uncertainty are observed. Under the prescribed conditions, both algorithms estimate basically the same annual average and interannual variations at both sites. This was observed at the other 6 sites as well. Thus, a definitive result about the performance of the time smoothing algorithm compared the control is difficult to deduce from the annual means alone.

Quantitative evidence of both the cross-correlation function and paired T-test of the error means show that the error time series of both algorithms are statistically different but nearly indistinguishable from one another. Beginning with the cross-correlation, Figure 3.7 shows the cross-correlation functions for the error time series at Harvard Forest and Vaira Ranch. The cross-correlation functions at both sites suggests that when either error time series lags the other, there is some periodicity and correlation between the two time series that exceeds the 95th percentile certainty bounds. The maximum exceedence of the confidence interval is at lag-0, but the general exceedence is on the order of .05 which is within the relative certainty of the significance bounds given the sample size. This is true across all sites. This result indicates that the two optimizations cannot be seen as IID from one another in this test. However, since the violation of the certainty bounds is small and

the sample size much larger in comparison to the statistical test requirements of the paired T-test can still be used. The paired T-test results demonstrate that the interannual source or sink estimate from the time smoothing algorithm was equal to or greater than the control algorithm for 6 of the 8 sites estimated to within the 95th percentile. Campbell River and Vaira Ranch both resulted in statistically significant better annual estimates than the control algorithm. Consequently, these two statistical tests verify the qualitative results of the annual NEE averages and RMSE reductions.

3.2.3. EXPERIMENT 1: INCREASING OBSERVATIONAL UNCERTAINTY

When exposed to increasing amounts of observational uncertainty, the time smoothing algorithm was more resilient to observational uncertainty changes than the control. The other three panels of Figures 3.5 and 3.6 show the effects of 2, 5, and 10 times increases in observational uncertainty estimates for Harvard Forest and Vaira Ranch. Both algorithms revert toward the prior estimate of NEE before receding toward the original estimations of SiB4 flux. At all sites, it was evident that the control algorithm regresses toward the prior estimate much sooner than the time smoothing algorithm. The effect of this increase is moderated by how much original certainty the observations had. Therefore, a well-observed flux was good for both algorithm's resulting estimates, but only the time smoothing algorithm showed robustness to more poorly-observed fluxes.

3.2.4. EXPERIMENT 1: SEASONALITY

When seasonality was examined, the time smoothing and control algorithms showed that neither algorithm was particularly skilled at estimating the seasonal cycle. Figure 3.7 shows the autocovariance functions of the NEE error time series for both algorithms. The autocorrelation functions for Harvard Forest indicates that on a yearly basis, both algorithms are correlated with

themselves outside of the 95th percentile certainty bounds. The location of this error was representative of a fall or spring mismatch where NEE crosses zero. This pattern was observed at all sites except for ARM-SGP and Vaira Ranch. The general correlation exceedence of the confidence bounds at these sites was about .06 and .11 for the control and time smoothing algorithms. The autocorrelation function at Vaira Ranch indicated the presence of white noise. When this result was tested on the Ljung-Box test, Vaira Ranch was shown to still have some correlation remaining in the error at the 99th confidence level. In general, the magnitude and timing of error varied from site-to-site, but these results suggest there was still some residual of seasonality to be estimated.

The mean power spectra for the first 20 harmonics for both Harvard Forest and Vaira Ranch are seen in Figure 3.8. These two sites suggested that there was still statistically significant power within at least the first 5 harmonics for both algorithms. The zeroth and seasonal harmonic (k=0 and 1) suggested that neither the general mean or seasonal cycle were fully resolved in either time series. These power spectra results are not generalized to all sites. The other 6 sites were able to fully resolve both the mean and seasonality of the NEE signal to within red noise spectrum of 95th percentile, but not the normal red noise spectrum.

3.3. EXPERIMENT 2

The purpose of the second experiment was to evaluate the time smoothing algorithm against the control algorithm when using modeled GPP and RESP fluxes to formulate an NEE estimate which was optimized by observed the NEE flux. As stated in the methods, this version of the algorithm optimizes for 24 bias coefficients rather than the 52 independent weekly bias coefficients and uses a portion of both the posterior and prior model covariance estimates. Table 3.2 shows the results of all statistical significance tests done to the optimizations of the second experiment and whether or not the statistical hypothesis tests were met.

3.3.1. EXPERIMENT 2: FLUX ESTIMATES AND RMSE REDUCTION

The flux estimates from the second experiment indicated that while NEE is well-estimated, it achieved at the cost of the GPP and RESP signals. Example component flux estimates for Harvard Forest and Vaira Ranch from the second experiment are shown in Figure 3.9. As can be seen at both sites, the second experiment was capable of making excellent estimates for any year of the NEE signal. The RESP and GPP estimates do not resemble the observations or prior estimates and are physically unrealistic. These results were seen across all sites. These visual results are supported by the fractional RMSE reduction.

In the middle panel of Figure 3.3, the RMSE reduction of NEE shows that the second experiment was skilled at making a better prediction than that of the prior flux estimate and control estimate. For example, the RMSE reduction of NEE at Harvard Forest for Experiment 2 is on the order of .25 to .45, which is nearly a .2 better than the control algorithm. All sites showed improvement and better performance in the fractional RMSE reduction of NEE, however this came at the cost of an increase in RMSE for the component fluxes. In Figure 3.4, the fractional RMSE reduction for the component fluxes are seen for the second and third experiments. Across 7 sites for both GPP and RESP, the second experiment resulted in negative RMSE reductions upwards of -.1 to -.3. This suggests that both component fluxes lost estimation skill upwards of 300% in some circumstances. Vaira Ranch was the only site to have both positive fractional RMSE reductions for both the net and component fluxes as consequences of this result.

3.3.2. EXPERIMENT 2: ANNUAL SOURCES AND SINKS AND UNCERTAINTY INCREASES

The annual NEE mean estimate gave way to supporting the results of the RMSE of NEE reductions. Like the first experiment, example annual NEE averages from Harvard Forest and Vaira Ranch under increasing amounts of observational uncertainty for the second experiment are seen

in Figures 3.10 and 3.11. In the top left panel of these figures, the second experiment shows near better estimation of the annual NEE average over the control to within error estimates of observed NEE average. The interannual pattern is well-estimated. In the other three panels of both figures, there is virtually no change to the algorithm's performance except with larger uncertainty bounds. This indicates that this version of the time smoothing algorithm has robust estimation skill with upwards of 100 times more observational uncertainty. These same results were observed at the other 6 sites as well. This qualitative evidence is supported by both the cross-correlation functions and paired T-test for the original uncertainty estimation.

Quantitative evidence of both the cross-correlation function and paired T-test of the error means show that the error time series of both algorithms are statistically different but more distinguishable from one another than the first experiment. The cross-correlation functions of Harvard Forest and Vaira Ranch in Figure 3.12 show that the correlation between the time series is lower than the first experiment. As demonstrated at Harvard Forest, 5 of the 8 sites exhibited some periodicity in the correlation on a yearly basis, but the only substantial maximum exceedence of the confidence interval is at lag-0 and in the final lag. The general exceedence is on the order of .07 which is within the relative certainty of the significance bounds given the sample size N. Vaira Ranch demonstrated how the other 3 sites produced cross-correlation functions that resemble nearly pure noise. These result suggest the error time series can be interpreted as IID from one another in this test, thus violation of the T-test's assumptions is kept to a minimum. The application the paired T-test demonstrated that at every site the time smoothing algorithm produced better estimates of the interannual source or sink over the control algorithm to within the 95th confidence level. These two statistical tests verified the results the annual NEE averages and RMSE of NEE reductions.

3.3.3. EXPERIMENT 2: ANNUALLY AVERAGED COMPONENT FLUXES

The evidence presented by the time series plots of GPP and RESP indicated that there would be little information about the plots of the annual average of GPP and RESP for any site, however a description of this error can still be seen by the cross-correlation and paired T-test between the observations and the component fluxes. Figures 3.13 and 3.14 show the cross-correlation functions between the observations and the component fluxes. At both sites, it is visually evident that there is a sinusoidal pattern that follows a biannual statistically significant pattern of correlation and anti-correlation. There are 5 superimposed harmonics within these cross-correlation functions that are representative of the 5 harmonics used for the time smoothing algorithm estimate. The general exceedence of the certainty bounds is on the average order of .2 for RESP and .3 for GPP. This result suggests the component fluxes at Harvard Forest sites are not IID from the observations, but this result does not necessarily hold true for all sites. Campbell River, Lethbridge, UMBS, and ARM-SGP all showed similar behaviors with respect to the harmonic structure, but indicated noise from the cross-correlation functions. These 4 sites were assumed to be IID and evaluated using the paired T-test. When applied to the paired T-test, only 1 of the 4 IID sites showed the annual average of GPP for the time smoothing algorithm is equal to annual average of the observations within the 95th confidence level. Additionally, the paired T-test demonstrated that all four IID sites have annual average of RESP estimations that are equal to the annual average of the observations within the 95th confidence level.

3.3.4. EXPERIMENT 2: NEE SEASONALITY

The second experiment was exceptional in obtaining the NEE seasonality while not skilled in obtaining the component flux seasonality. Figure 3.12 visually show that the error autocorrelation functions of NEE for the time smoothing algorithm is noise. There is only minor periodicity that

is substantially suppressed from the first experiment and with the exception of the first couple lags, the autocovariance functions do not surpass the 95th percentile certainty bounds. This was true across all 6 other sites. When the autocorrelation functions were applied to the Ljung-Box Test, it was found that none of the 8 sites only had white noise composing the error. The mean power spectra of NEE error analysis in Figure 3.8 showed that the error time series of the second experiment does not have significant power above the red noise spectrum at the 95th certainty level for either the mean or the seasonal harmonics. In general, these results suggested the error between the observations and time smoothing algorithm at the mean and seasonal cycles are red noise at best, but there does exist some residual subseasonal signal in the error.

3.3.5. EXPERIMENT 2: COMPONENT FLUX SEASONALITY

As opposed to the successful results of the NEE seasonality analysis, the second experiment was not skilled in obtaining the component flux seasonality. Both example sites in Figures 3.13 and 3.14 show that the autocorrelation functions of the component flux error time series are virtually noise except for the first 20 lags. At these lags for both component fluxes, the correlation is on the average about .3 above the 95th percentile certainty bounds. This was seen at 7 of the 8 flux towers with the exception of UMBS. Given the white noise nature of the remaining signal for the component fluxes, the Ljung-Box test revealed that white noise was not present in either error time series at any site. The mean power spectra of RESP flux error analysis in Figure 3.15 that for both example sites the second experiment does not produce significant power above the red noise spectrum at the 95th confidence level for either the mean or the seasonal harmonics. This was true for all 8 sites. Furthermore, the mean power spectra of the GPP flux error analysis in Figure 3.15 showed mixed results concerning the annual and seasonal error power. For 7 of the 8 sites, the spectral power produced by GPP error time series was between the red noise time series

and red noise spectrum at the 95th confidence level for both the mean or the seasonal harmonics. Harvard Forest was the only site that produced significant power at mean and seasonal harmonics, but in all first 10 harmonics, which could be an outlier result. In general, the combination of the visual, qualitative, and quantitative tests done on the time smoothing time series suggested poor and unrealistic estimation of the component fluxes.

3.4. EXPERIMENT 3

The purpose of the third experiment was to evaluate the time smoothing algorithm against the control algorithm using only observed the NEE and GPP fluxes to optimize for the modeled GPP and RESP fluxes. As stated in the methods, this version of the algorithm optimizes for 24 bias coefficients and uses a portion of both the posterior and prior model covariance estimates rather than the 52 independent weekly bias coefficients. Table 3.3 shows the results of all statistical significance tests done to the optimizations of the third experiment and whether or not the statistical hypothesis tests were met.

3.4.1. EXPERIMENT 3: FLUX ESTIMATES AND RMSE REDUCTION

The flux estimates from the third experiment resulted in all three fluxes being well-estimated. Example component flux estimates for Harvard Forest and Vaira Ranch from the third experiment are shown in Figure 3.16. From these figures, the third experiment is capable of recovering all observed fluxes for any year of the flux signal at Vaira Ranch and for most years at Harvard Forest. Like the second experiment, the NEE signal is well fitted. Unlike the second experiment, the RESP and GPP estimates now fit the observations, which is much more physically realistic. These results were seen across all sites except for Mead-Irrigated. At this site, the estimates resembled the

second experiment. The visual results of these time series are supported by the fractional RMSE reduction.

In the bottom panel of Figure 3.3, the RMSE reduction of NEE shows that the third experiment is skilled at making a similar NEE estimate to that of the second experiment. For example, the RMSE reduction of NEE at UMBS for experiment 3 is on the order of .3 to .5, which is identical to that of the second experiment and about .2 better than the control. 6 of the 8 towers showed similar results. Old Black Spruce and Harvard Forest showed increased performance when compared the first experiment and control, but decreased performance when compared to the second experiment. In Figure 3.4, the fractional RMSE reduction across all 8 sites showed that for both GPP, the third experiment resulted in RMSE reductions upwards of .05 to .7. This was also true for RESP, but Mead-Irrigated was the only site to produce a negative RMSE reduction. This suggests that both component fluxes gained estimation skill upwards of 70% in some years. As a result of these tests, the other statistical tests were able to be used to statistically reinforce these results.

3.4.2. EXPERIMENT 3: ANNUAL SOURCES AND SINKS AND UNCERTAINTY INCREASES

Like the second experiment, the annual NEE mean estimates supported the results of the RMSE of NEE reductions. Example annual NEE averages from Harvard Forest and Vaira Ranch under increasing amounts of observational uncertainty for the third experiment are seen in Figures 3.17 and 3.18. The annual NEE average estimated by the time smoothing algorithm over Vaira Ranch shows better estimates than the control to within error estimates of observed NEE average. This result was seen in all sites except for Harvard Forest. Harvard Forest resulted in better estimates of the annually averaged NEE than the control, but does not replicate the observational record over most years. The interannual pattern is well-estimated to within error estimate at all sites except for Harvard Forest. Under increasing uncertainty, Vaira Ranch and the other 6 sites show virtually

no change to the algorithm's performance except with larger uncertainty bounds. Harvard Forest showed increased performance under a doubling of observational uncertainty, similar to the initial estimation of Harvard Forest under the second experiment. This result was constant under the 5 and 10 times simulations for Harvard Forest as well. Qualitatively, this algorithm estimates NEE sources and sinks comparable to the second experiment. This evidence is further supported by both the cross-correlation functions and paired T-test.

The cross-correlation functions and paired T-test of the error means showed that the error time series of the third experiment's time smoothing algorithm is statistically different from the control. In Figure 3.19, the cross-correlation functions of NEE at Harvard Forest and Vaira Ranch showed that the correlation between the two error time series was comparable to the results of the second experiment. The estimation at Harvard Forest demonstrated that when the control lags the time smoothing algorithm there is evidence of periodicity in the correlation on a yearly basis, but not vice versa. When the time smoothing algorithm lags the control, there is evidence of only minor periodicity and noise to within the 95th percentile certainty bounds. This result was seen at 5 of the 8 sites, with the exceptions being of Vaira Ranch, ARM-SGP, and UMBS. At these 5 sites, the maximum location and mean exceedence of the confidence bound was at lag-0 and .07. Therefore, across most sites these results were not considered only noise. The cross-correlation function at Vaira Ranch, ARM-SGP, and UMBS resemble noise and can be considered IID.

Since, the general of the exceedence of the cross-correlation function of NEE is on the order of .07, the paired T-test was applied to all sites. The paired T-tests demonstrated that at every site the time smoothing algorithm produced better estimates of the interannual source or sink over the control algorithm to within the 95th confidence level. Thus, these two statistical tests of NEE verified the results seen in the annual NEE averages and RMSE of NEE reductions.

3.4.3. EXPERIMENT 3: ANNUALLY AVERAGED COMPONENT FLUXES

The time series plots of GPP and RESP indicated that there is strong evidence that annual average of GPP and RESP for any site may be well-estimated. Figures 3.20 and 3.21 show the cross-correlation functions between the observations and the component fluxes. These two sites display nearly identical patterns on both wings of the cross-correlation function. Furthermore, it is visually evident that there is a sinusoidal pattern that follows an biannual statistically significant pattern of correlation and anti-correlation similar to that of the second experiment. The general exceedence of the certainty bounds is on the order of .4 for both RESP and GPP. This is result was seen for all sites. From this, these sites are not IID and are assumed to be indistinguishable from one another.

3.4.4. EXPERIMENT 3: NEE SEASONALITY

Like the second experiment, the third experiment was skilled in estimating the NEE seasonality. In Figure 3.19 for both example sites visually show that the error autocorrelation functions of the time smoothing algorithm is basically noise. These autocovariance functions for NEE do not surpass the 95th percentile certainty bounds with the exception of the first couple of lags. This was true across all other sites. When the autocorrelation functions were applied to the Ljung-Box Test, it was found that none of the 8 sites only had white noise composing the error, much like the second experiment.

The mean power spectra of NEE error analysis in Figure 3.8 showed that for both example sites the error time series of the third experiment did not have significant power above the red noise spectrum at the 95th certainty level for any tested harmonics. This was seen for all sites. Harvard Forest, Lethbridge, UMBS, and Mead-Irrigated produced an NEE error mean power spectrum that was above the normal red noise spectrum, but not above the critical certainty level. In general,

these results suggested the error between the observations and time smoothing algorithm at the mean and seasonal cycles are red noise at best, but there is a presence of unresolved subseasonal error.

3.4.5. EXPERIMENT 3: COMPONENT FLUX SEASONALITY

Unlike the the second experiment, the third experient was skilled in obtaining the component flux seasonality. Both example sites in Figures 3.20 and 3.21 show that the autocorrelation functions of the component flux error time series represent the most resemblance to white noise of any experiment. There are no lags that exceed the 95th percentile certainty bounds beyond the first 10 lags. This was found at all sites as well. The Ljung-Box test discredited the presence of only white noise in any component flux error time series. The mean power spectra of RESP flux error analysis suggested that there was no significant unresolved power present within any harmonic in the first 20 harmonics. In Figure 3.15, both example sites showed the third experiment does not produce significant power above the red noise spectrum at the 95th confidence level for RESP. This was found for the other 6 sites. At all sites, the mean power spectra of GPP flux error analysis suggested that there was significant power present within in the first 20 harmonics, especially within the first 5 harmonics. The mean power spectra of GPP flux error analysis in Figure 3.15 exceeded the baseline red noise spectrum all sites. Furthermore, the power spectrum for 5 of the 8 sites exceeded the red noise spectrum at the 95th confidence level. In general, these results, with all other tests taken into account, suggests that these are just the minor differences between the observations and very similar component fluxes.

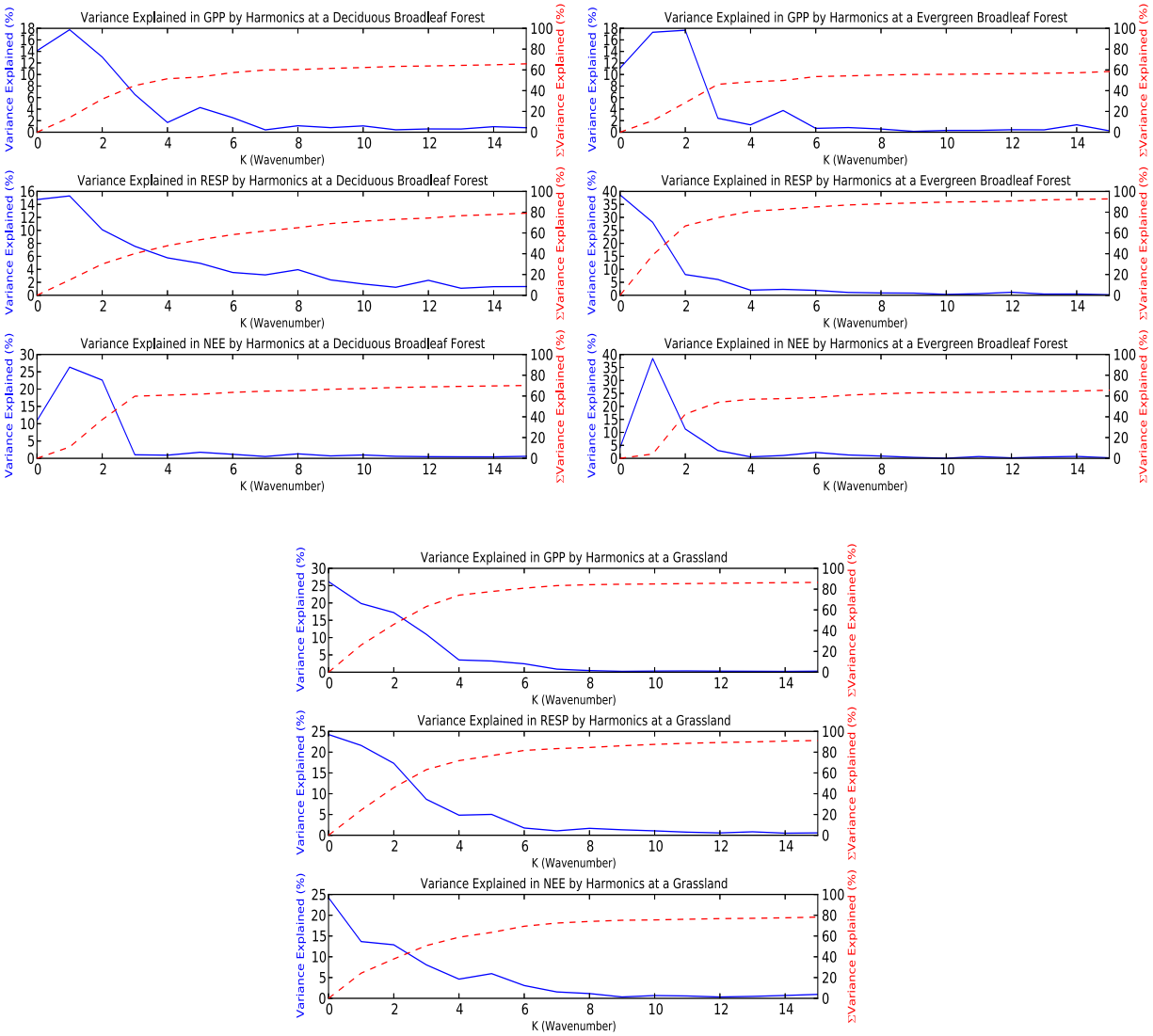


FIG. 3.1. Spectral plots of the percent of variance explained in the errors between the observed flux and the SiB4 flux. The blue curve is the percent of variance explained per wavenumber. The red curve is the partial integral of the blue curve signifying the sum of the variance explained. Upper Left: Harvard Forest, MA. Upper Right: KM67, Tapajos, Brazil. Bottom Center: Lethbridge, Canada

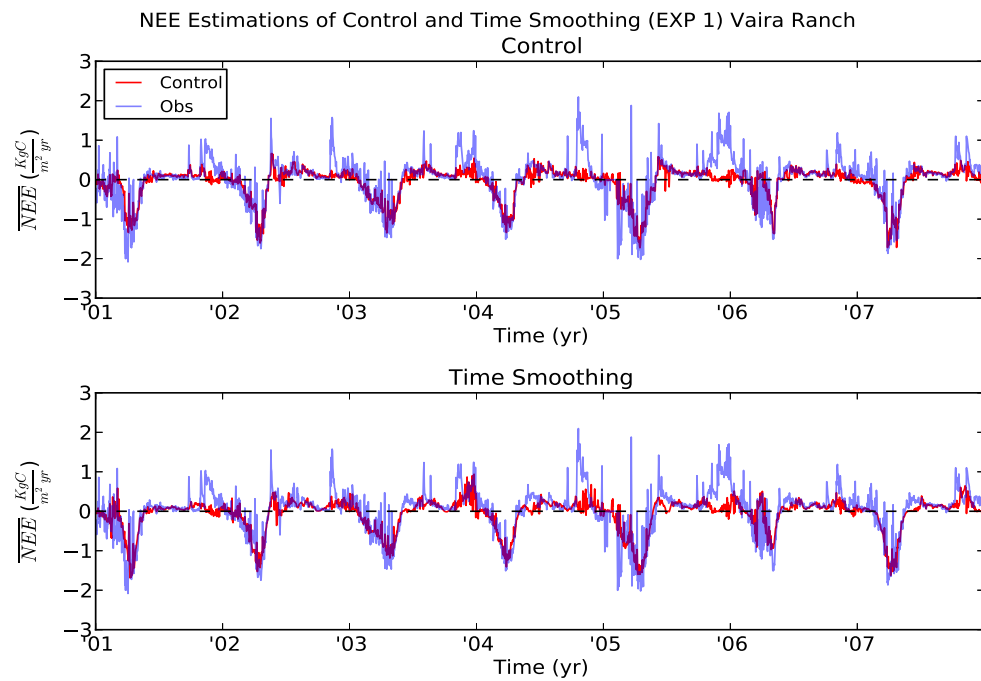
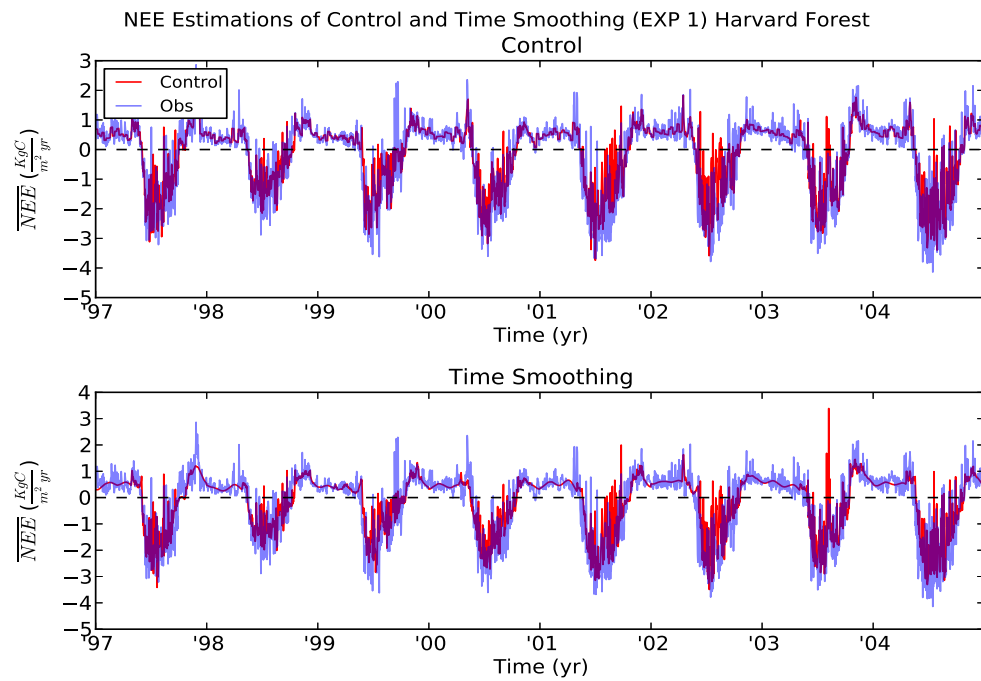


FIG. 3.2. Time evolution of the daily component fluxes at Harvard Forest and Vaira Ranch for the control and time smoothing estimates for Experiment 1. The blue lines are the observations. The red lines are the posterior estimates of a particular algorithm.

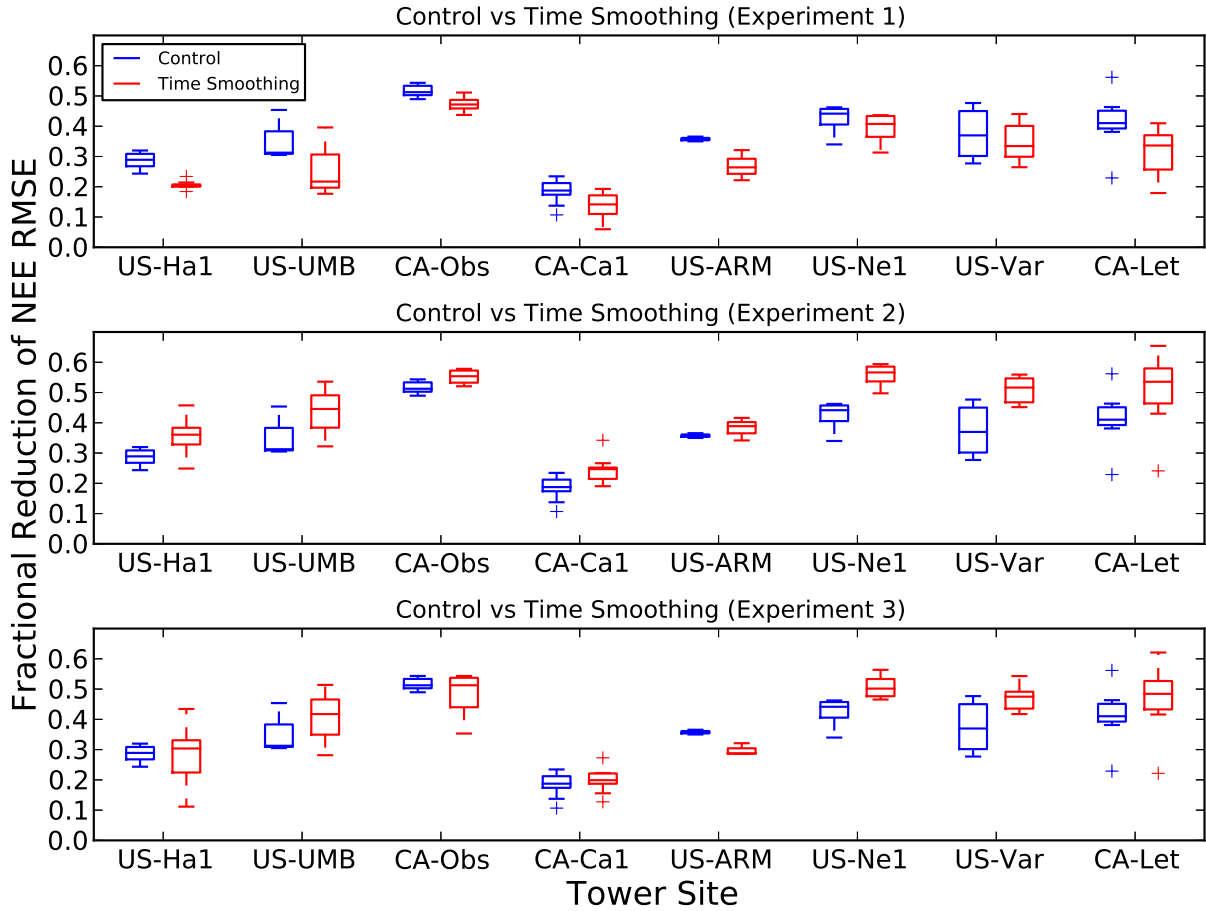


FIG. 3.3. Box-and-whiskers plots of the fractional reduction of RMSE of NEE estimations between the control and the three time smoothing algorithm variants across all sites. Blue and red boxes represent the control and time smoothing algorithm results. "+" signs represent outliers.

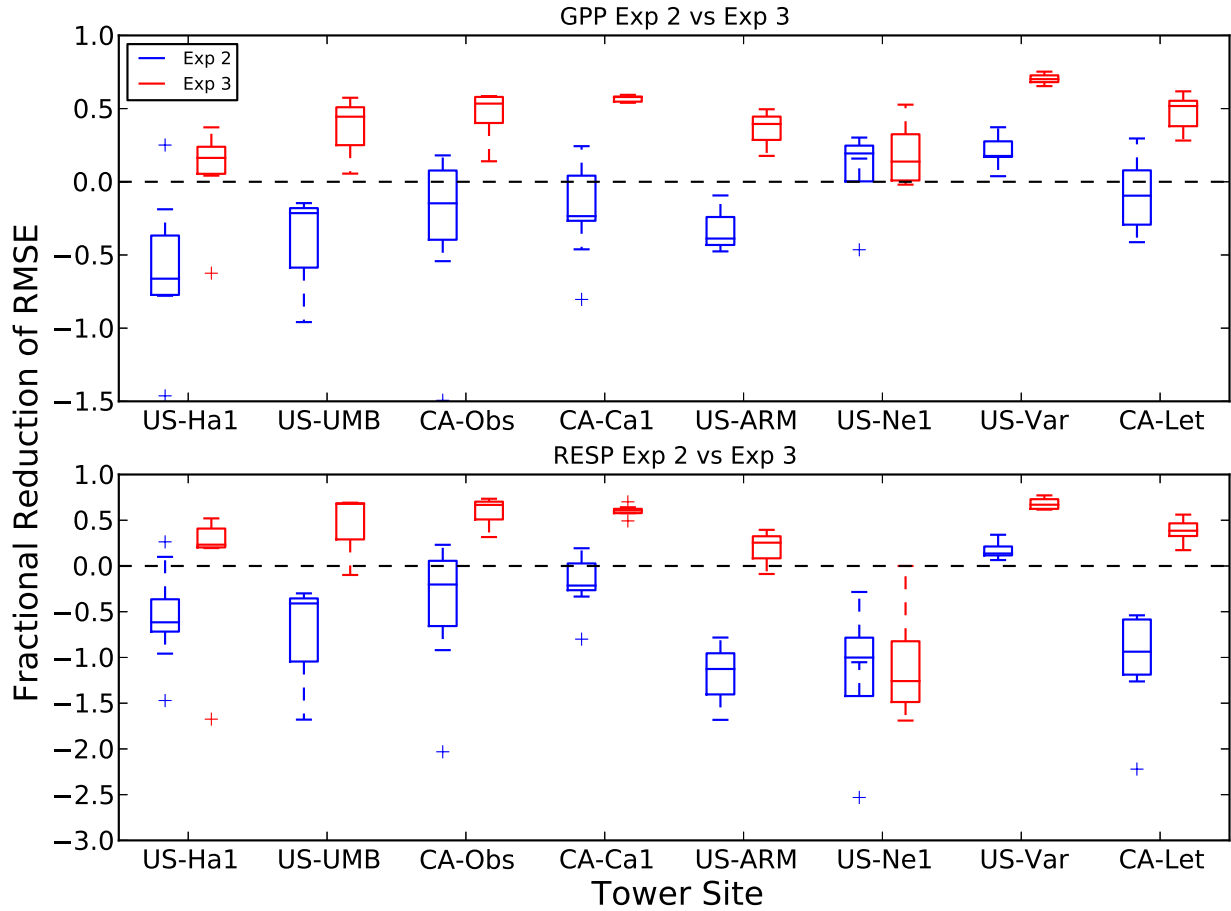
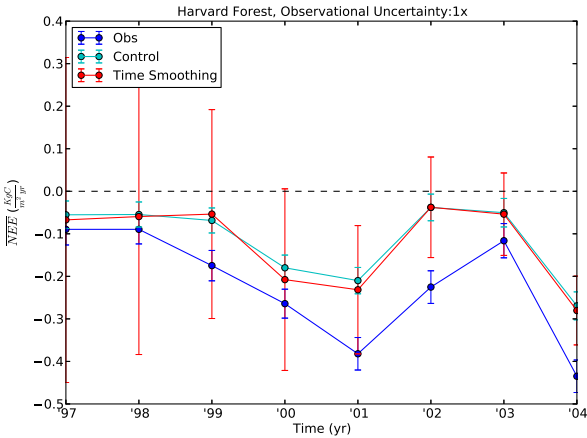
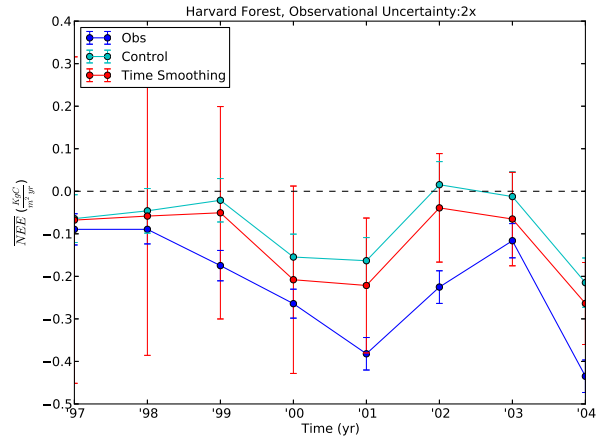


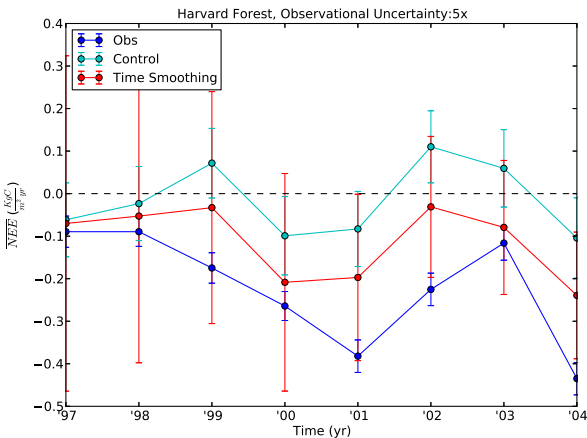
FIG. 3.4. Box-and-whiskers plots of the fractional reduction of RMSE of the component fluxes between the time smoothing algorithm of the 2nd and 3rd experiments. Blue and red boxes represent the 2nd and 3rd experiments fit of the particular component flux. "+" signs represent outliers.



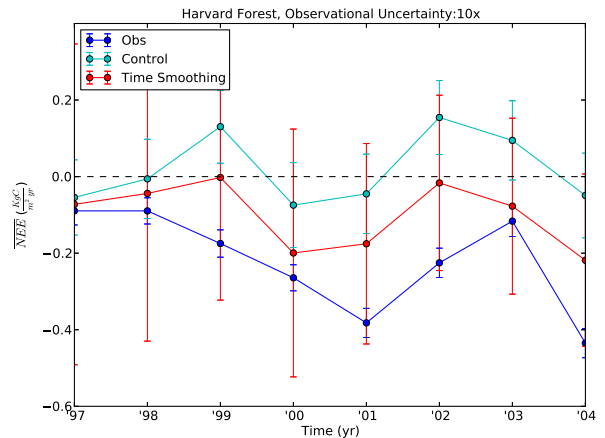
(A) Harvard Forest 1 Times Uncertainty



(B) Harvard Forest 2 Times Uncertainty

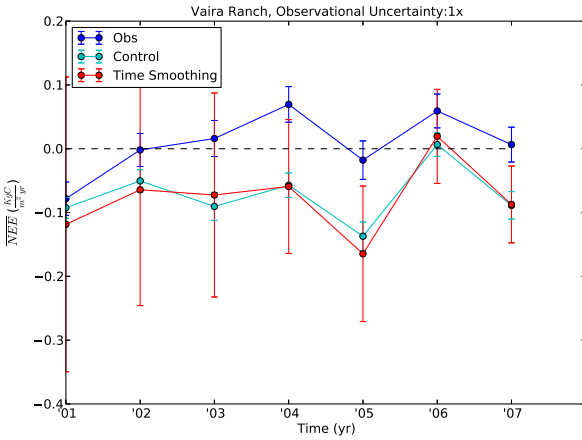


(C) Harvard Forest 5 Times Uncertainty

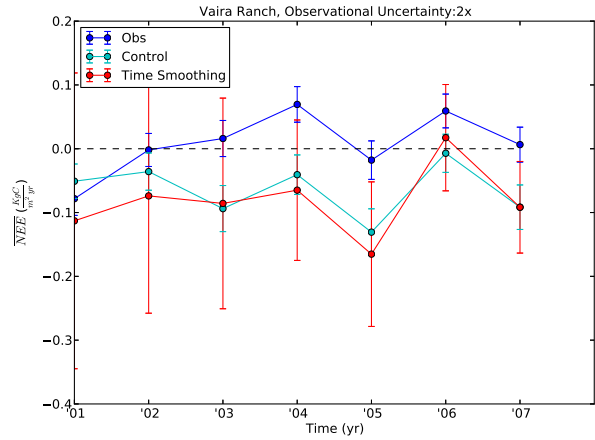


(D) Harvard Forest 10 Times Uncertainty

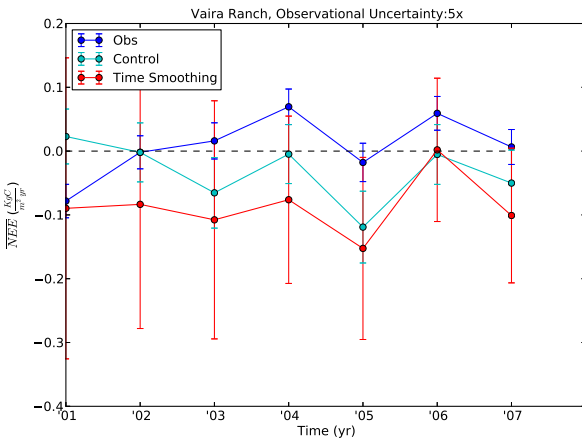
FIG. 3.5. Time evolution of the annually averaged NEE flux at Harvard Forest under varying amounts of observational uncertainty. Blue and cyan lines are the observations and control simulation. Purple lines are SiB4's simulation pre-assimilation. Red lines are the posterior estimates of SiB4 during assimilation. Error bars represent the 1 standard deviation uncertainty in the flux.



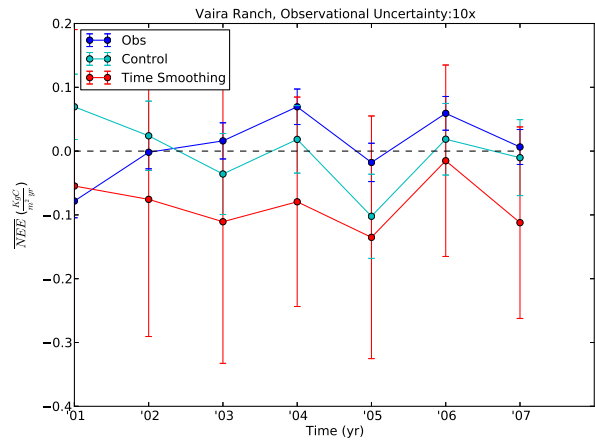
(A) Vaira Ranch 1 Times Uncertainty



(B) Vaira Ranch 2 Times Uncertainty

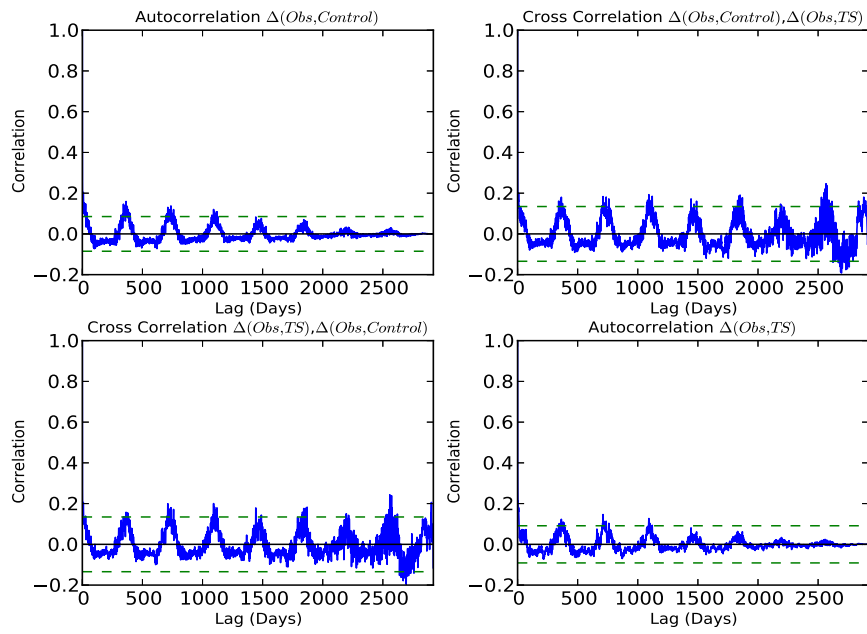


(C) Vaira Ranch 5 Times Uncertainty

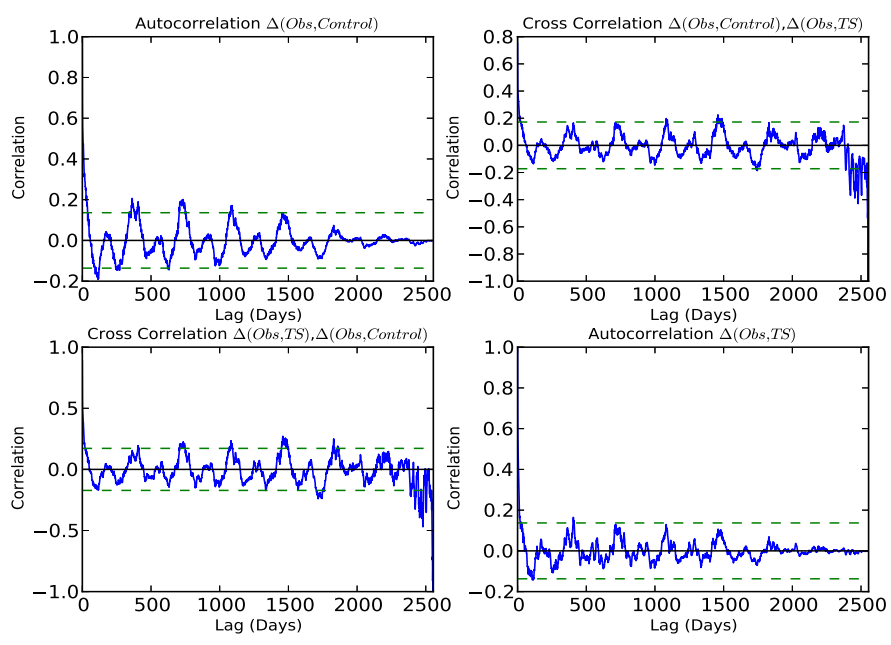


(D) Vaira Ranch 10 Times Uncertainty

FIG. 3.6. Time evolution of the annually averaged NEE flux at Vaira Ranch under varying amounts of observational uncertainty. Blue and cyan lines are the observations and control simulation. Purple lines are SiB4's simulation pre-assimilation. Red lines are the posterior estimates of SiB4 during assimilation. Error bars represent the 1 standard deviation uncertainty in the flux.



(A) Harvard Forest



(B) Vaira Ranch

FIG. 3.7. Cross-correlation and Autocorrelation functions between the error time series of the control and time smoothing algorithm used in Experiment 1 Harvard Forest and Vaira Ranch. Top Left: Autocorrelation function of control fit error. Top Right: cross-correlation function when control lags time smoothing. Bottom Left: cross-correlation function when time smoothing lags control. Bottom Right: Autocorrelation function of error time smoothing fit time series.

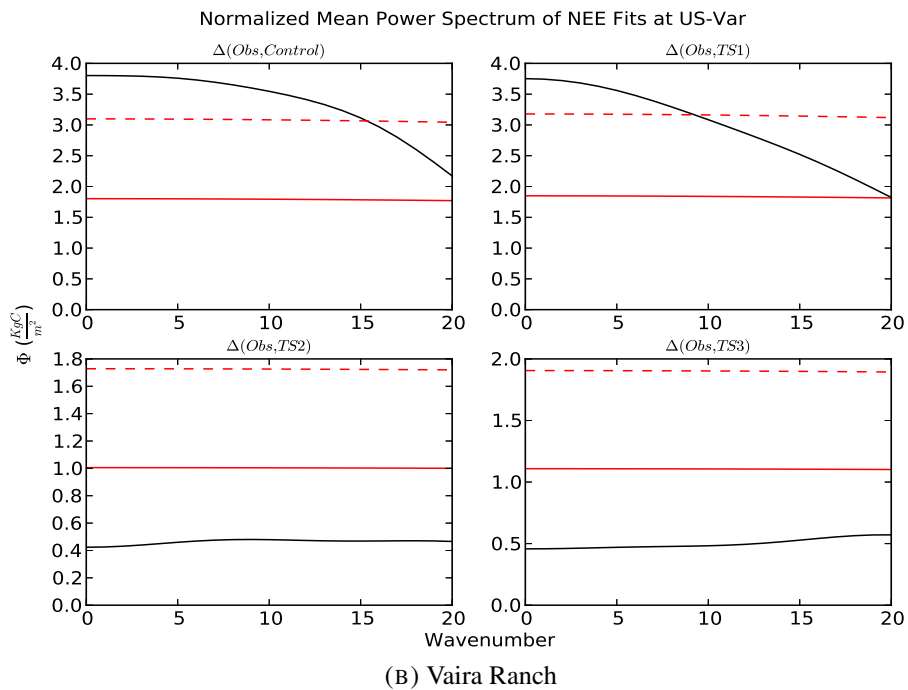
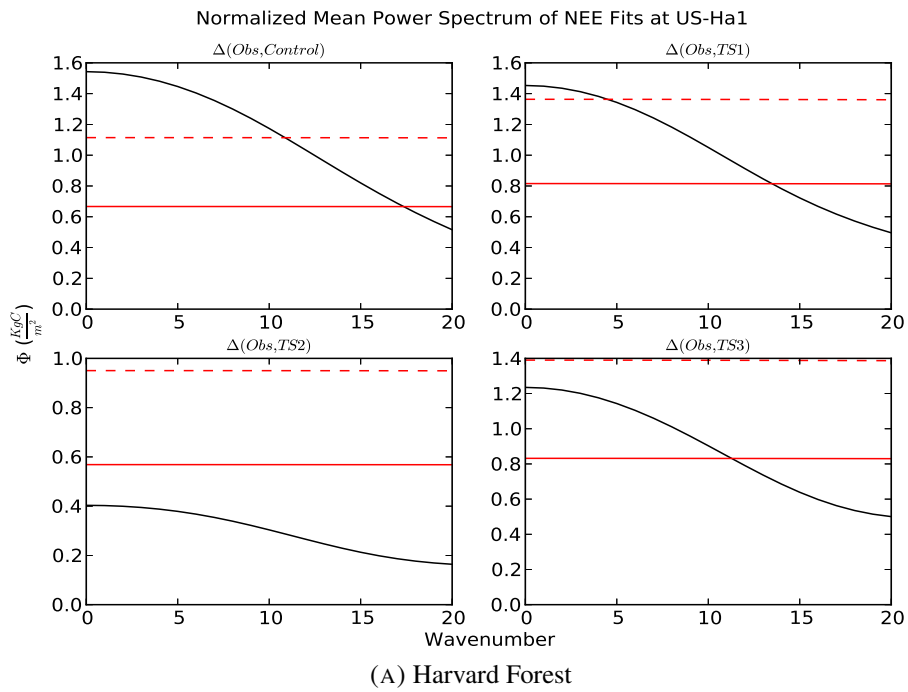
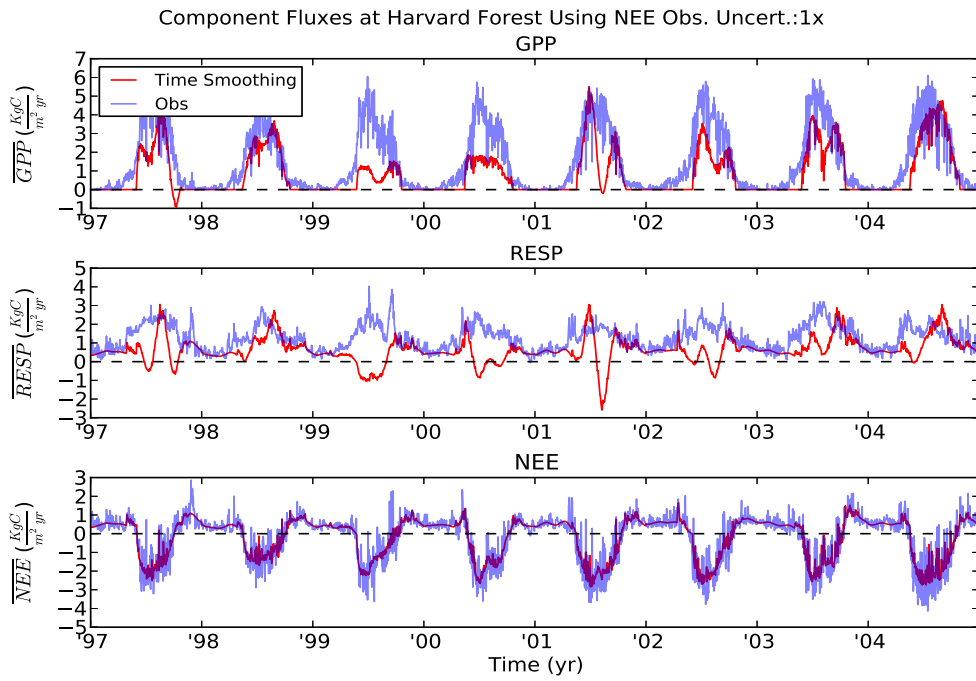
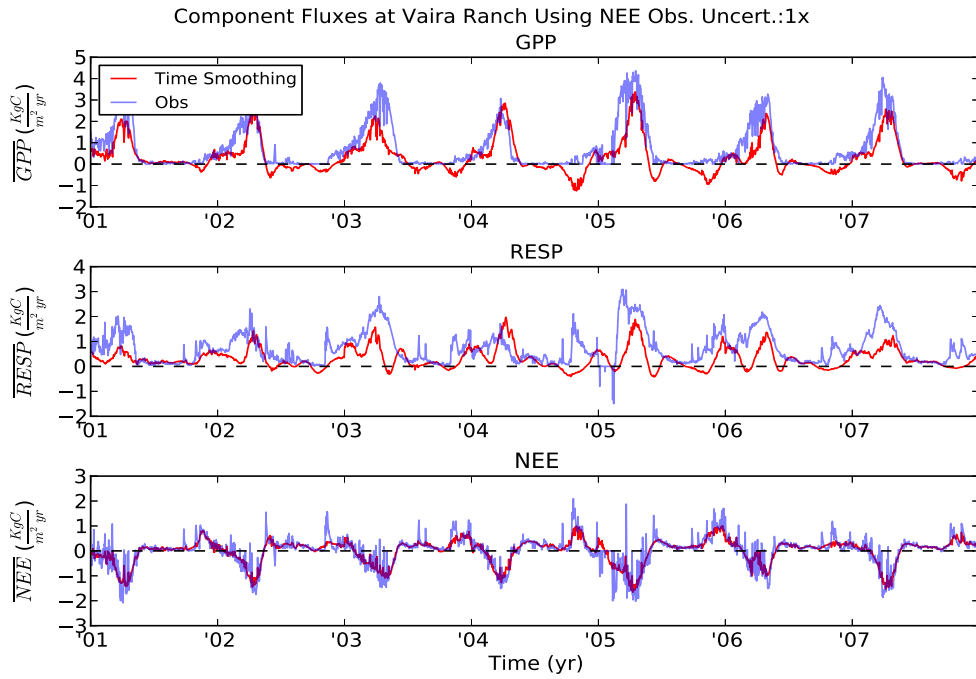


FIG. 3.8. Mean power spectrums for NEE error for all time smoothing variants and control at Harvard Forest and Vaira Ranch. Black lines are power. Red solid line line is the red noise power spectrum of the datum, and the dashed red line is the red noise spectrum at the 95th percentile. Top Left: Control. Top Right: Time smoothing algorithm for Experiment 1. Bottom Left: Time smoothing algorithm for Experiment 2. Bottom Right: Time smoothing algorithm for Experiment 3

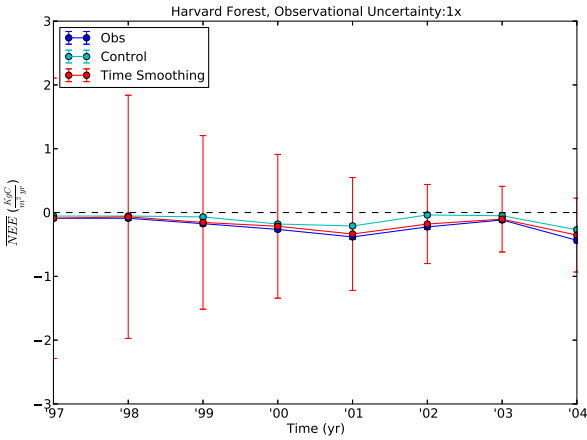


(A) Harvard Forest

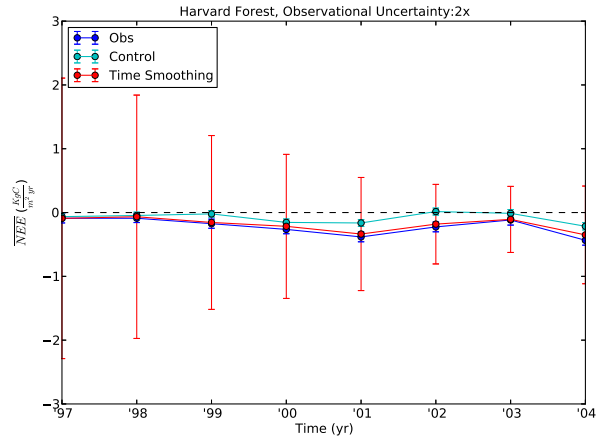


(B) Vaira Ranch

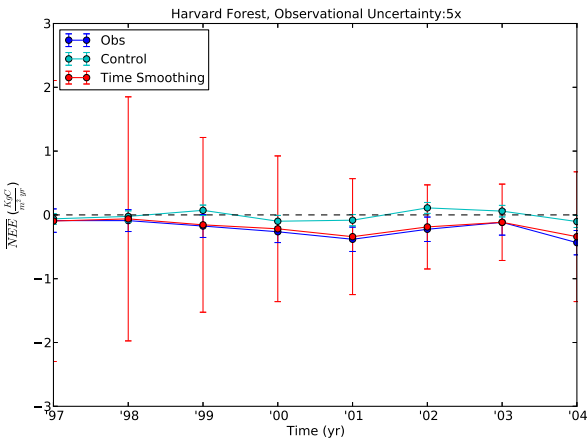
FIG. 3.9. Time evolution of the daily component fluxes of both Harvard Forest and Vaira Ranch as a result of the second experiment. The blue lines are the observations. The red lines are the posterior estimates.



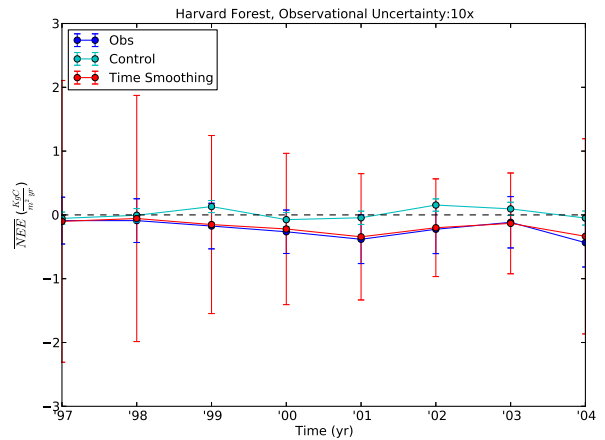
(A) Harvard Forest 1 Times Uncertainty



(B) Harvard Forest 2 Times Uncertainty

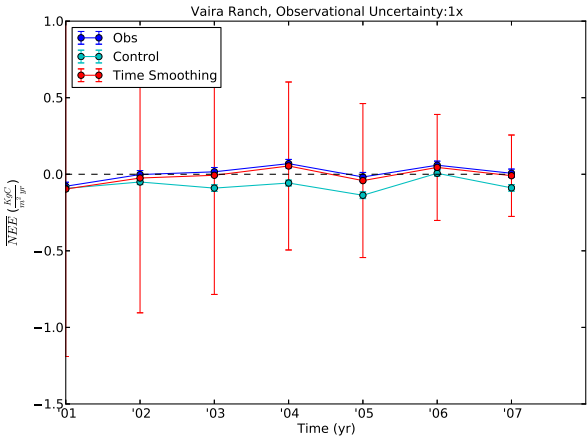


(C) Harvard Forest 5 Times Uncertainty

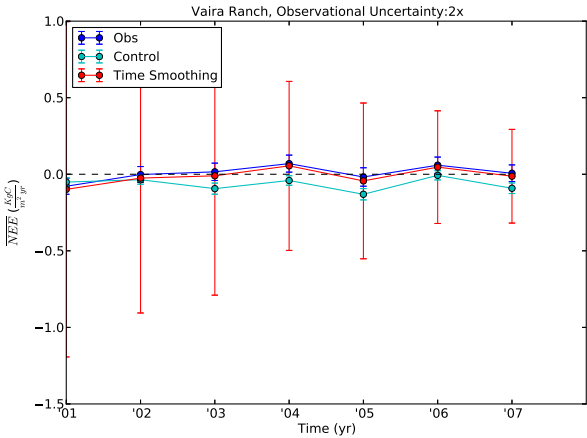


(D) Harvard Forest 10 Times Uncertainty

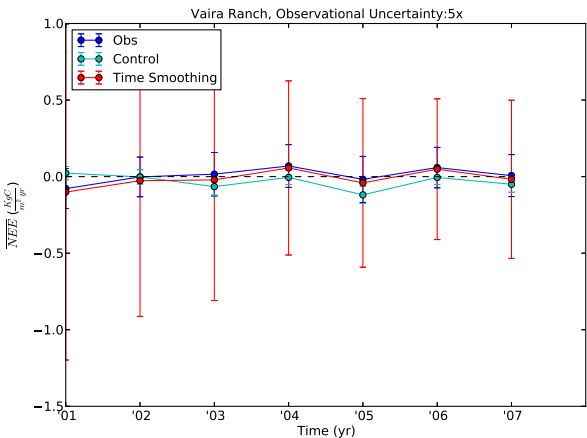
FIG. 3.10. Time evolution of the annually averaged NEE flux at Harvard Forest under varying amounts of observational uncertainty. Blue and cyan lines are the observations and control simulation. Purple lines are SiB4's simulation pre-assimilation. Red lines are the posterior estimates of SiB4 during assimilation. Error bars represent the 1 standard deviation uncertainty in the flux.



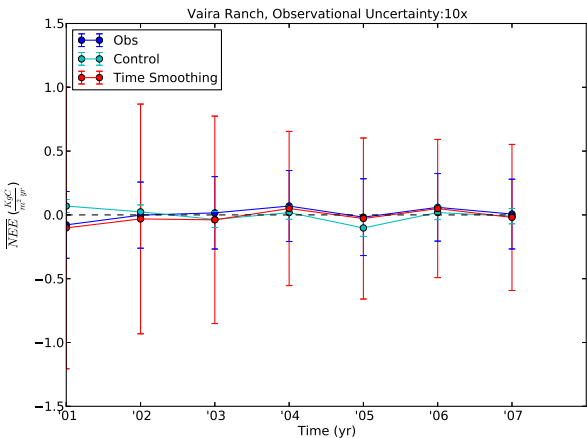
(A) Vaira Ranch 1 Times Uncertainty



(B) Vaira Ranch 2 Times Uncertainty

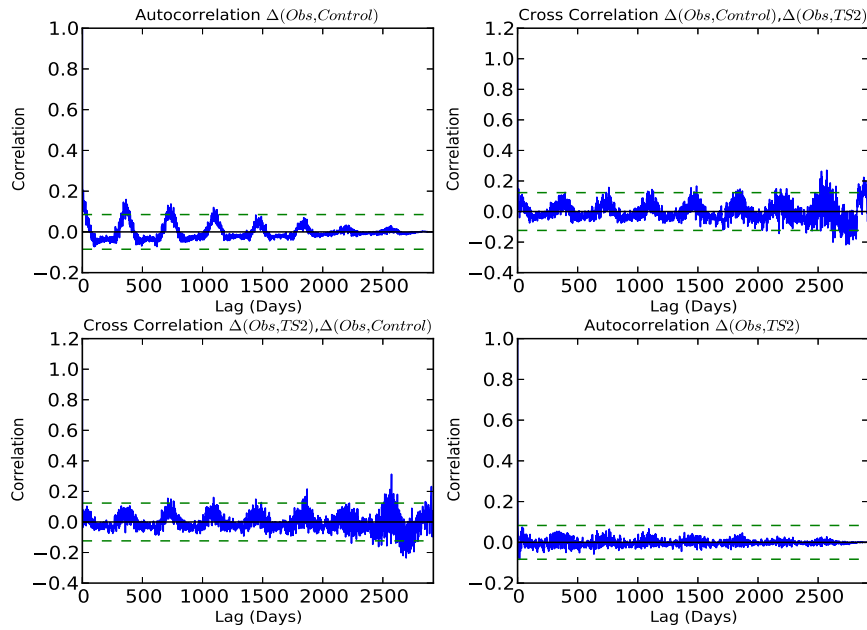


(C) Vaira Ranch 5 Times Uncertainty

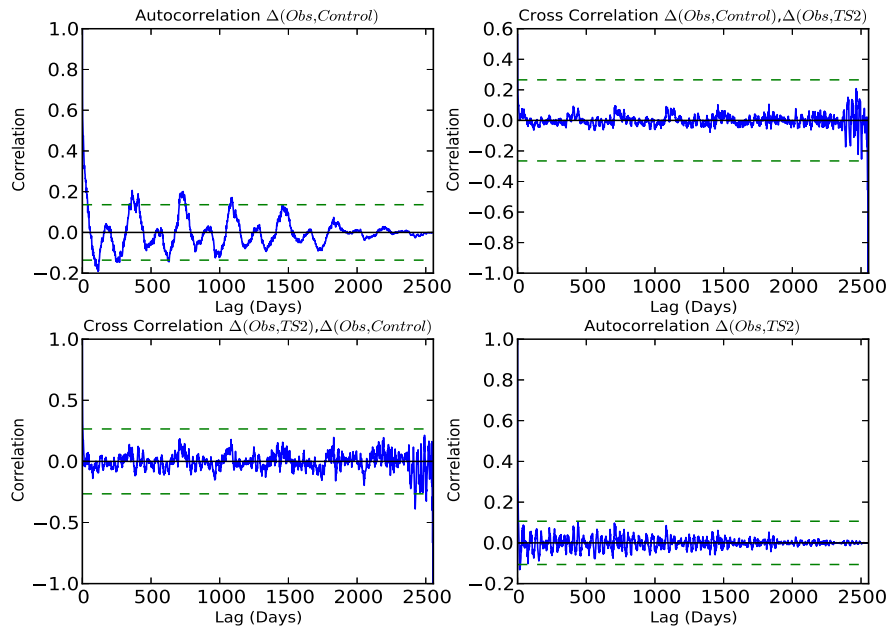


(D) Vaira Ranch 10 Times Uncertainty

FIG. 3.11. Time evolution of the annually averaged NEE flux at Vaira Ranch under varying amounts of observational uncertainty. Blue and cyan lines are the observations and control simulation. Purple lines are SiB4's simulation pre-assimilation. Red lines are the posterior estimates of SiB4 during assimilation. Error bars represent the 1 standard deviation uncertainty in the flux.

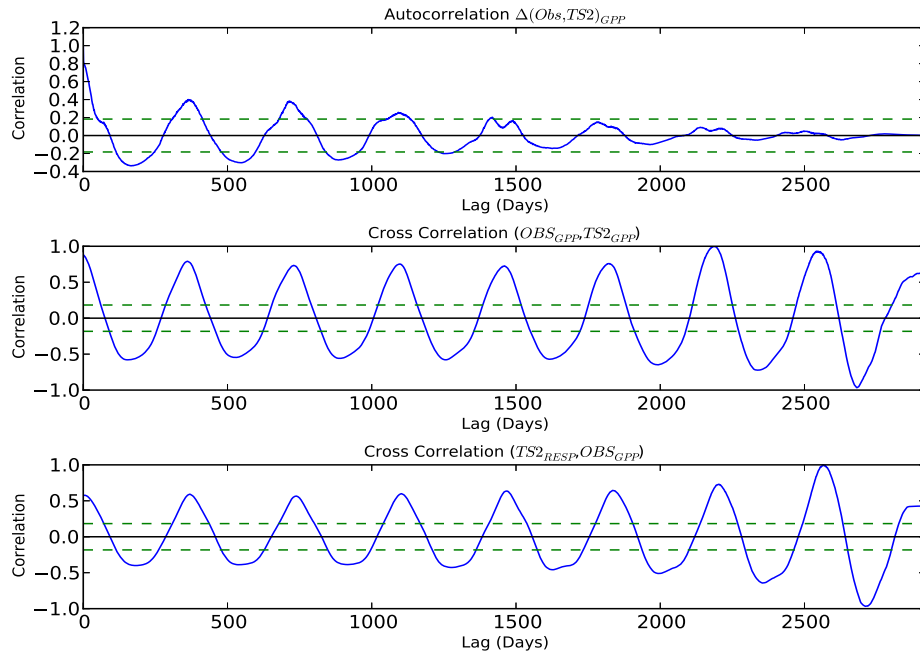


(A) Harvard Forest

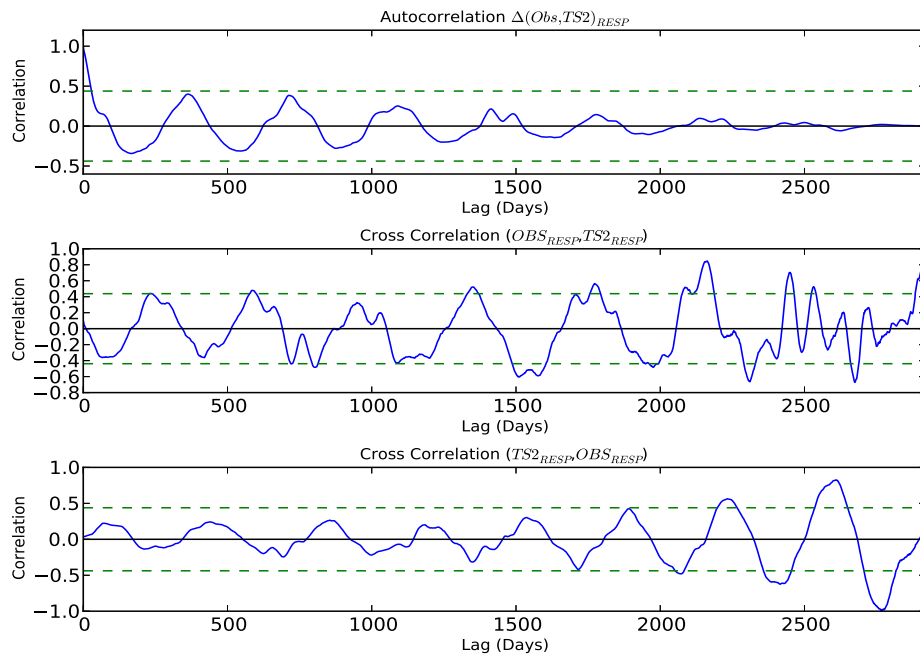


(B) Vaira Ranch

FIG. 3.12. Cross-correlation and Autocorrelation functions between the error time series of the control and time smoothing algorithm used in Experiment 2 Harvard Forest and Vaira Ranch. Top Left: Autocorrelation function of control fit error. Top Right: cross-correlation function when control lags time smoothing. Bottom Left: cross-correlation function when time smoothing lags control. Bottom Right: Autocorrelation function of error time smoothing fit time series.

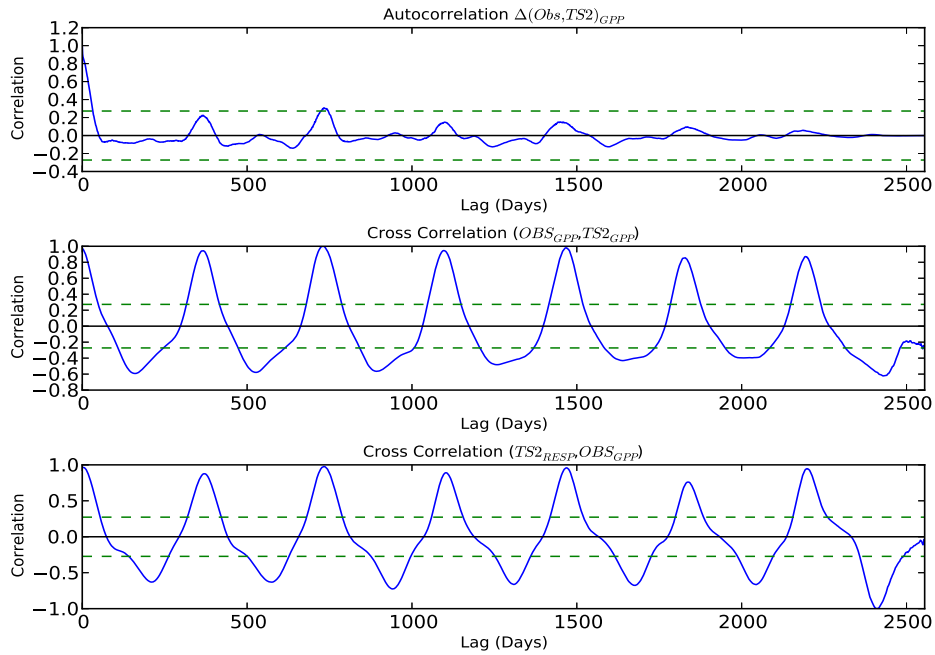


(A) Harvard Forest: GPP

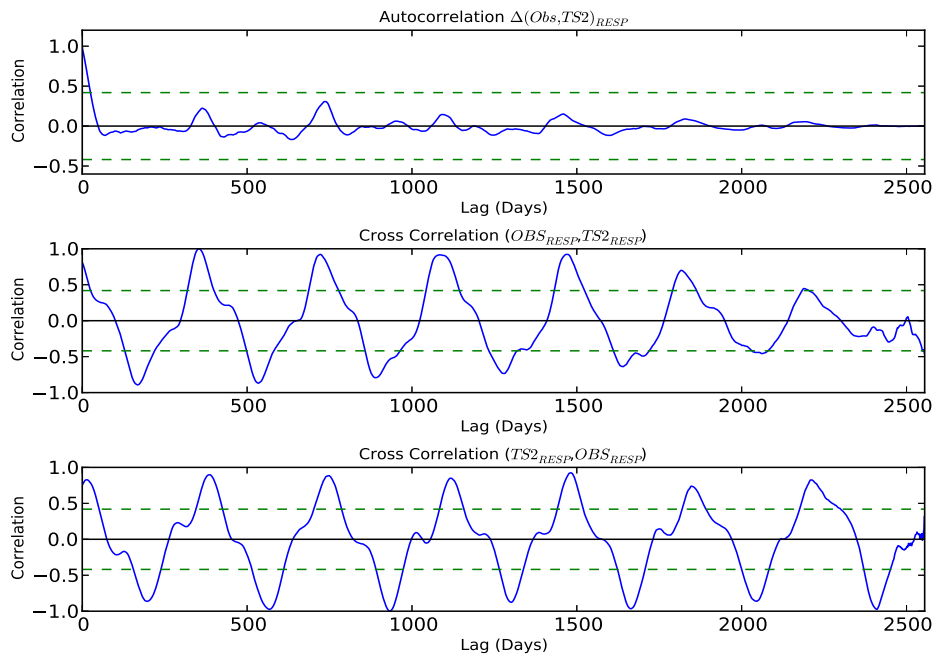


(B) Harvard Forest: RESP

FIG. 3.13. Cross-correlation and Autocorrelation functions between the error time series of the control and time smoothing algorithm used in Experiment 2 for Harvard Forest. Top: GPP. Bottom: RESP. First Panel: Autocorrelation function of error time series. Middle Panel: Observations lag Time Smoothing Algorithm



(A) Vaira Ranch: GPP



(B) Vaira Ranch: RESP

FIG. 3.14. Cross-correlation and Autocorrelation functions between observation and time smoothing estimation time series used in Experiment 2 for Vaira Ranch. Top: GPP. Bottom: RESP. First Panel: Autocorrelation function of error time series. Middle Panel: Observations lag Time Smoothing Algorithm

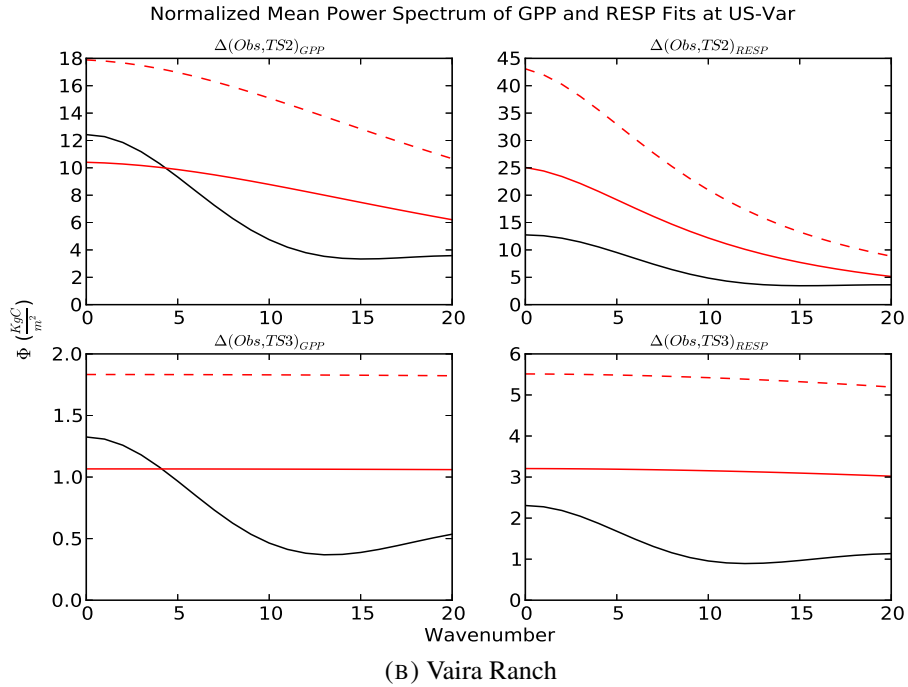
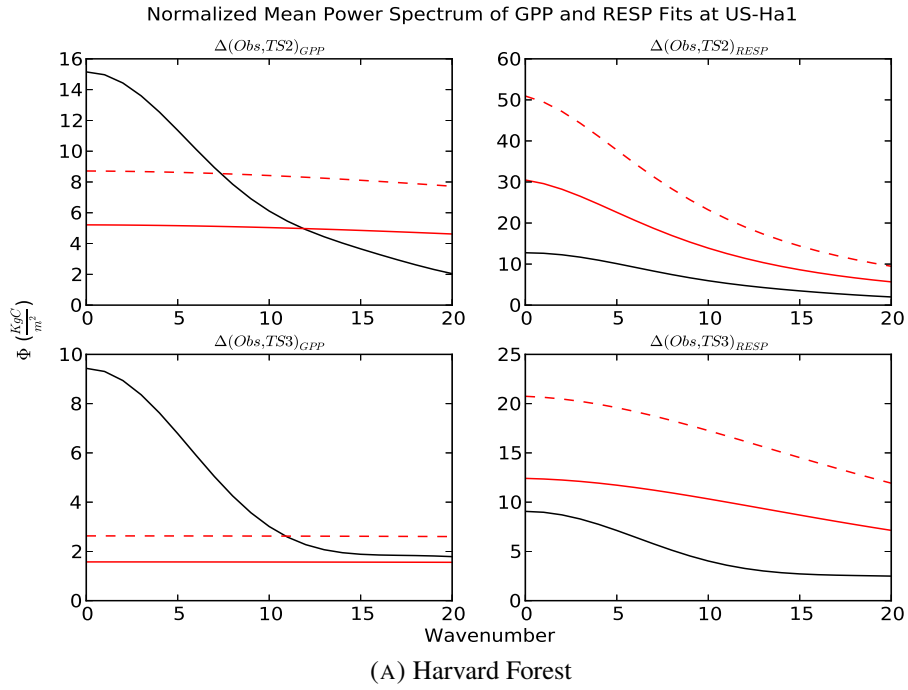
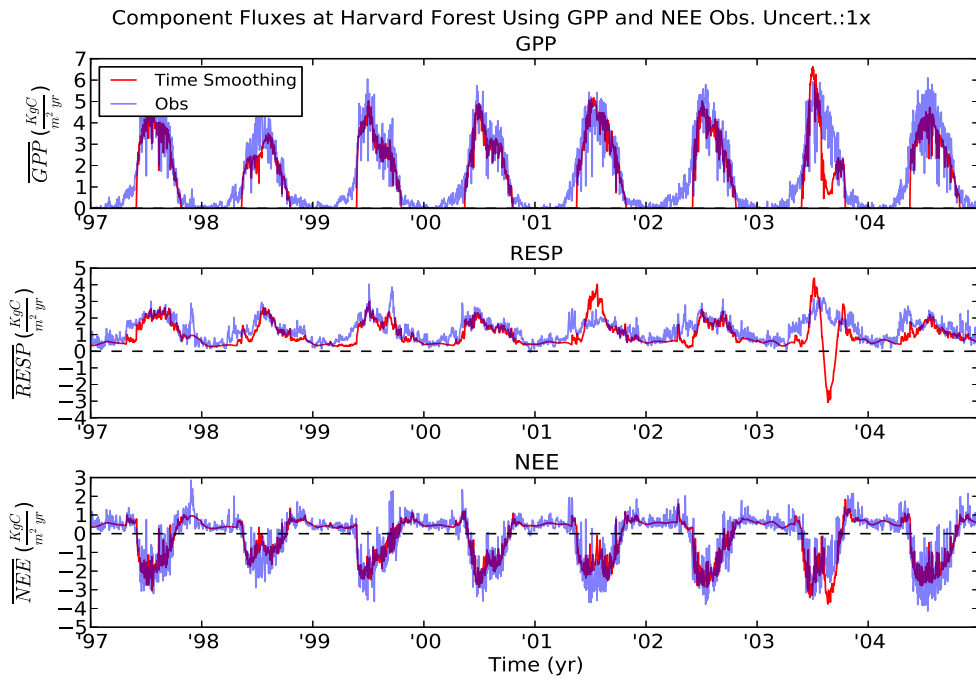
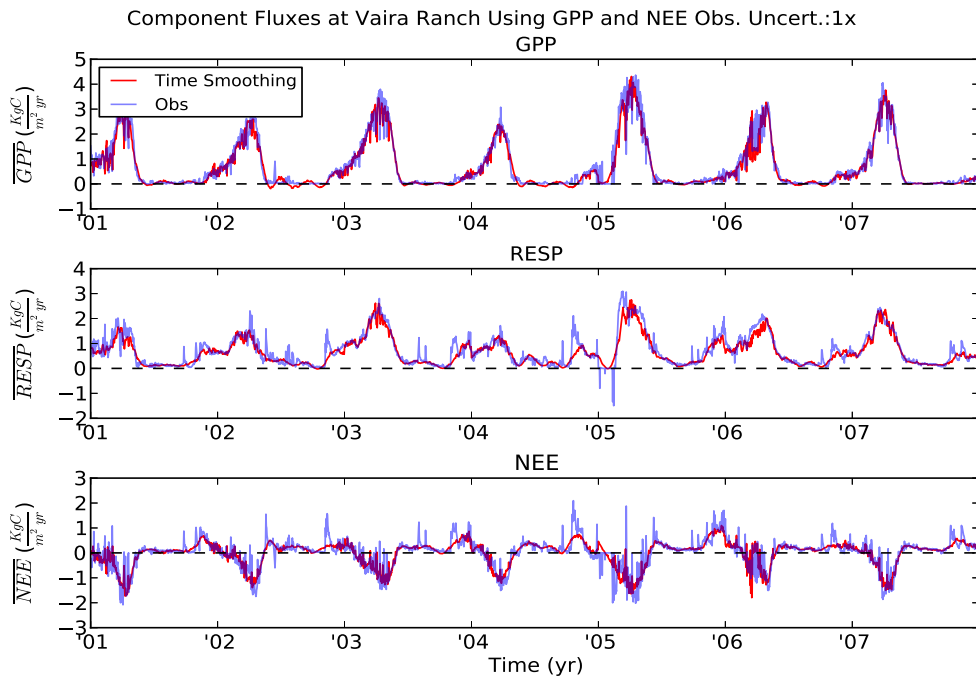


FIG. 3.15. Mean power spectrums of the component flux error for the second and third experiments at Harvard Forest and Vaira Ranch. Black lines are power. Red solid line is the red noise power spectrum of the datum, and the dashed red line is the red noise spectrum at the 95th percentile. Top Left: GPP Experiment 2. Top Right: RESP Experiment 2. Bottom Left: GPP Experiment 3. Bottom Right: RESP Experiment 3.

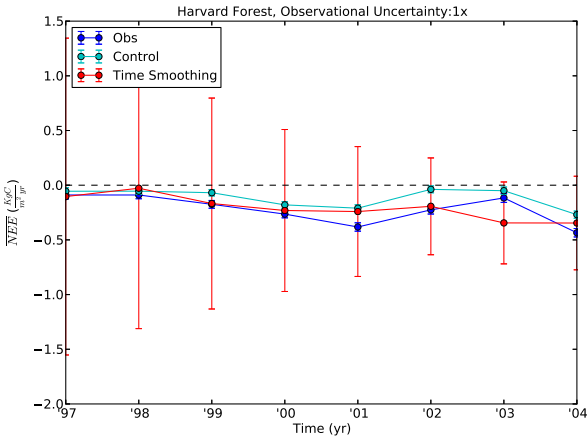


(A) Harvard Forest

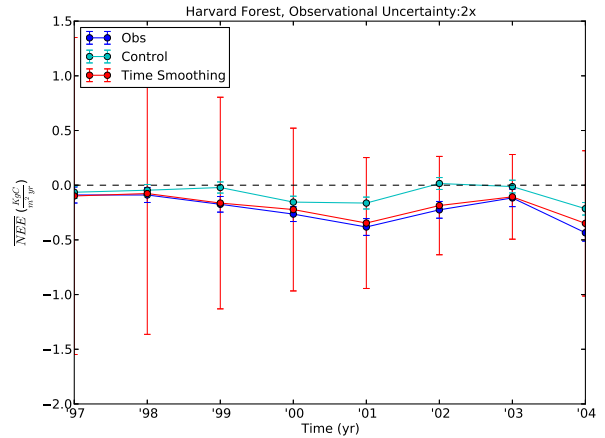


(B) Vaira Ranch

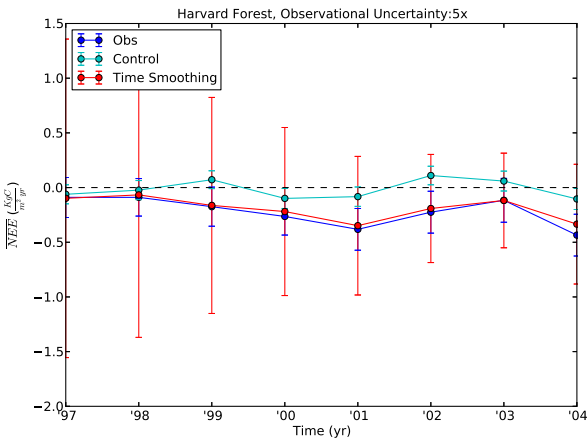
FIG. 3.16. Time evolution of the daily component fluxes of both Harvard Forest and Vaira Ranch as a result of the third experiment. The blue lines are the observations. The red lines are the posterior estimates.



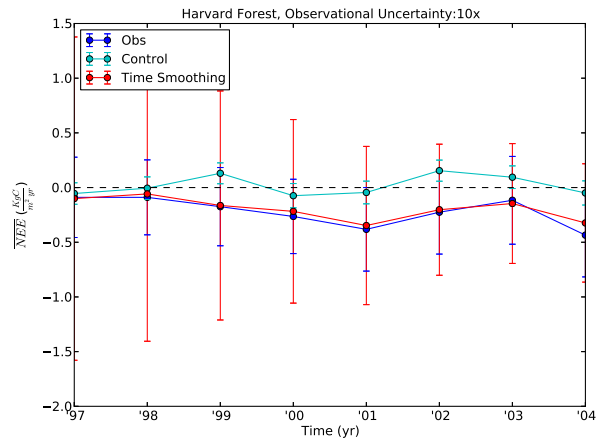
(A) Harvard Forest 1 Times Uncertainty



(B) Harvard Forest 2 Times Uncertainty

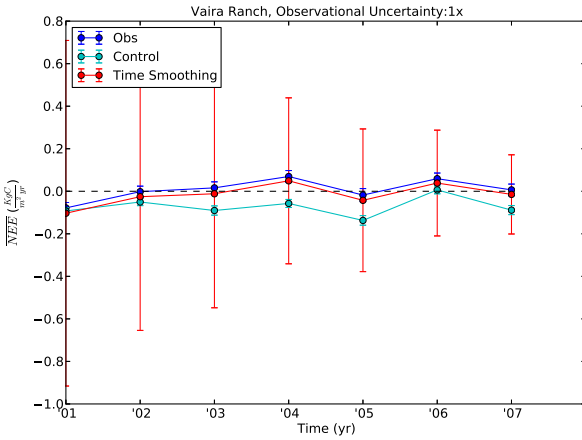


(C) Harvard Forest 5 Times Uncertainty

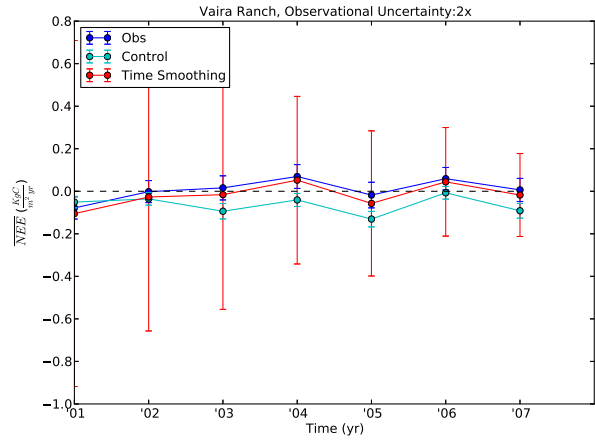


(D) Harvard Forest 10 Times Uncertainty

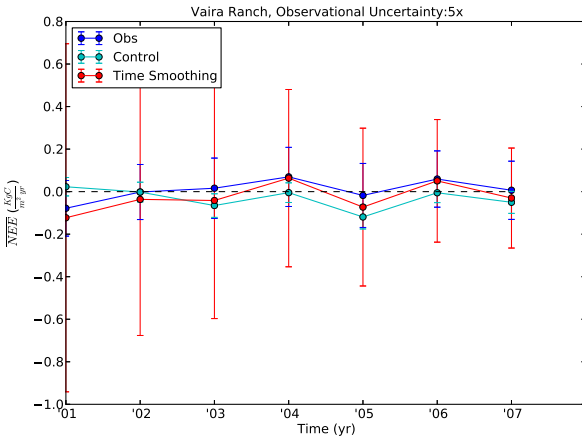
FIG. 3.17. Time evolution of the annually averaged NEE flux at Harvard Forest under varying amounts of observational uncertainty. Blue and cyan lines are the observations and control simulation. Purple lines are SiB4's simulation pre-assimilation. Red lines are the posterior estimates of SiB4 during assimilation. Error bars represent the 1 standard deviation uncertainty in the flux.



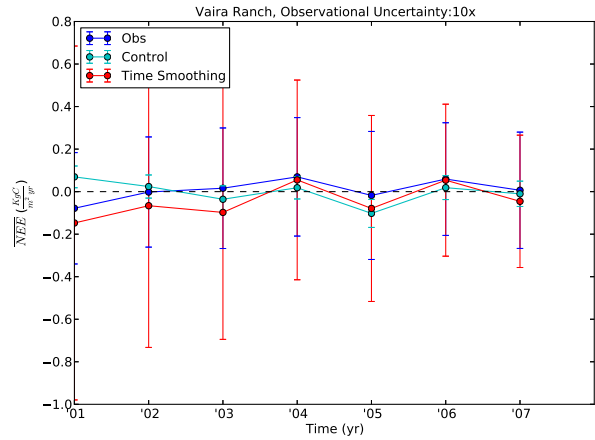
(A) Vaira Ranch 1 Times Uncertainty



(B) Vaira Ranch 2 Times Uncertainty

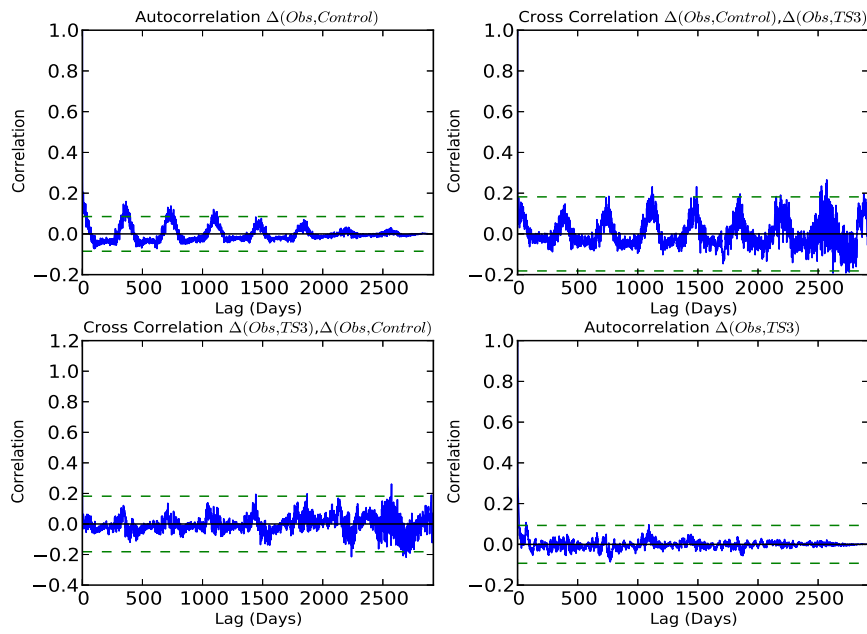


(C) Vaira Ranch 5 Times Uncertainty

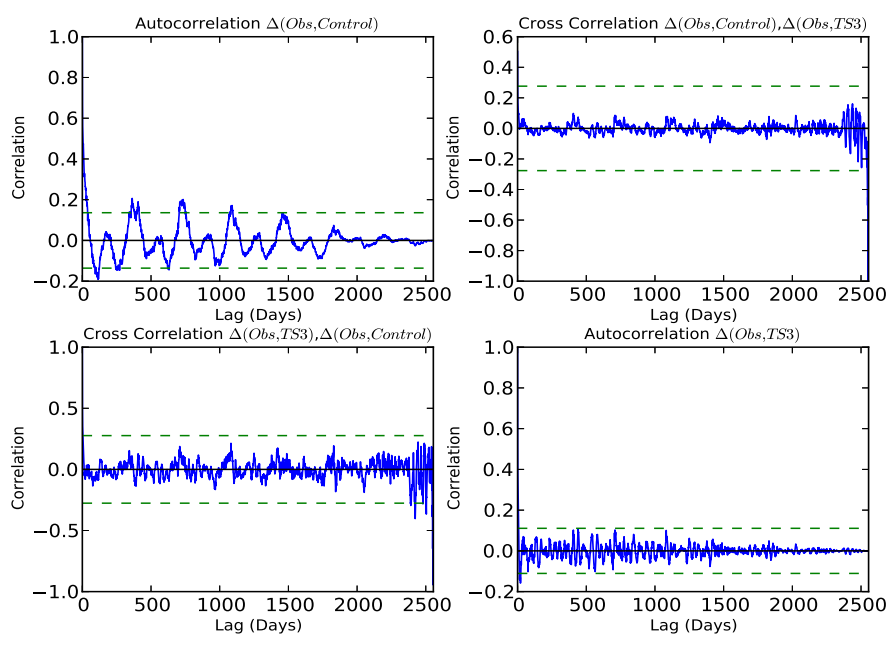


(D) Vaira Ranch 10 Times Uncertainty

FIG. 3.18. Time evolution of the annually averaged NEE flux at Vaira Ranch under varying amounts of observational uncertainty. Blue and cyan lines are the observations and control simulation. Purple lines are SiB4's simulation pre-assimilation. Red lines are the posterior estimates of SiB4 during assimilation. Error bars represent the 1 standard deviation uncertainty in the flux.

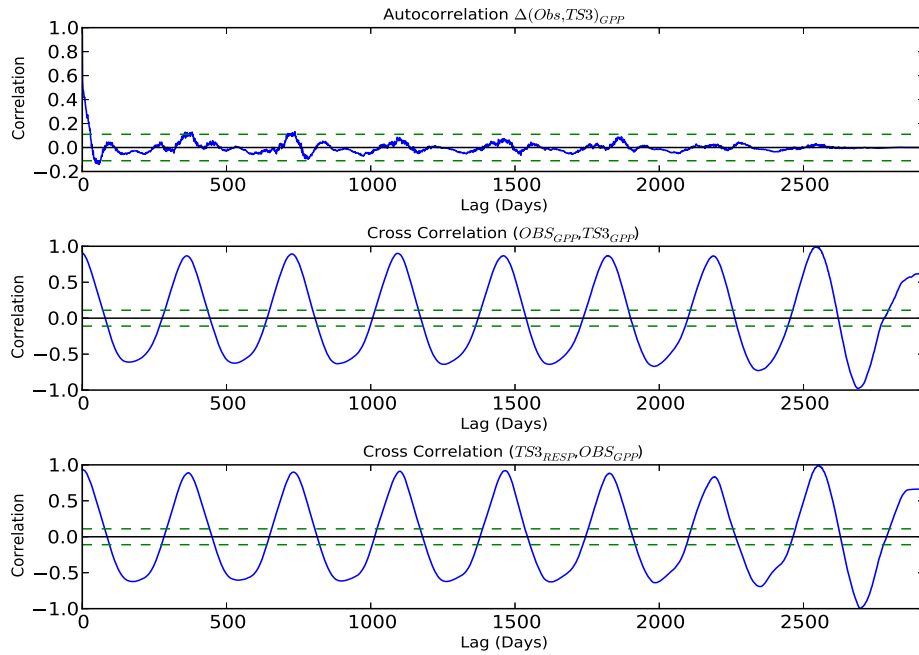


(A) Harvard Forest

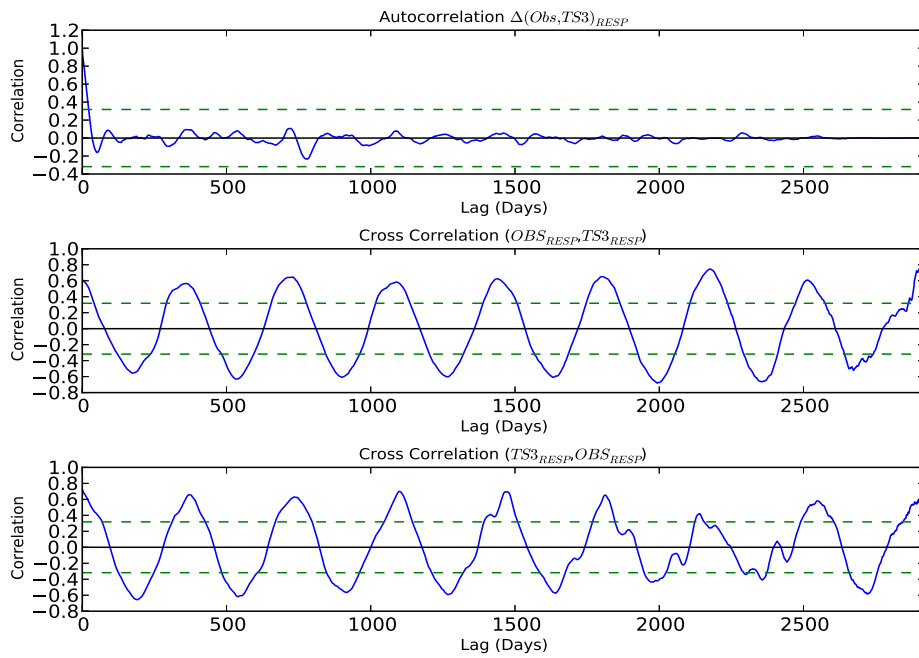


(B) Vaira Ranch

FIG. 3.19. cross-correlation and Autocorrelation functions between the error time series of the control and time smoothing algorithm used in Experiment 3 Harvard Forest and Vaira Ranch. Top Left: Autocorrelation function of control fit error. Top Right: cross-correlation function when control lags time smoothing. Bottom Left: cross-correlation function when time smoothing lags control. Bottom Right: Autocorrelation function of error time smoothing fit time series.

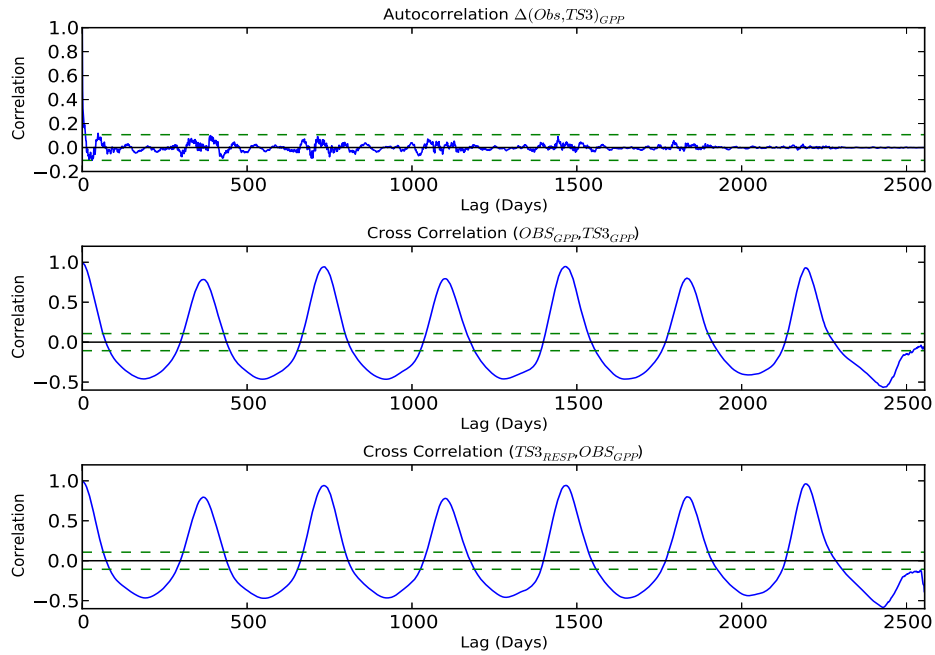


(A) Harvard Forest: GPP

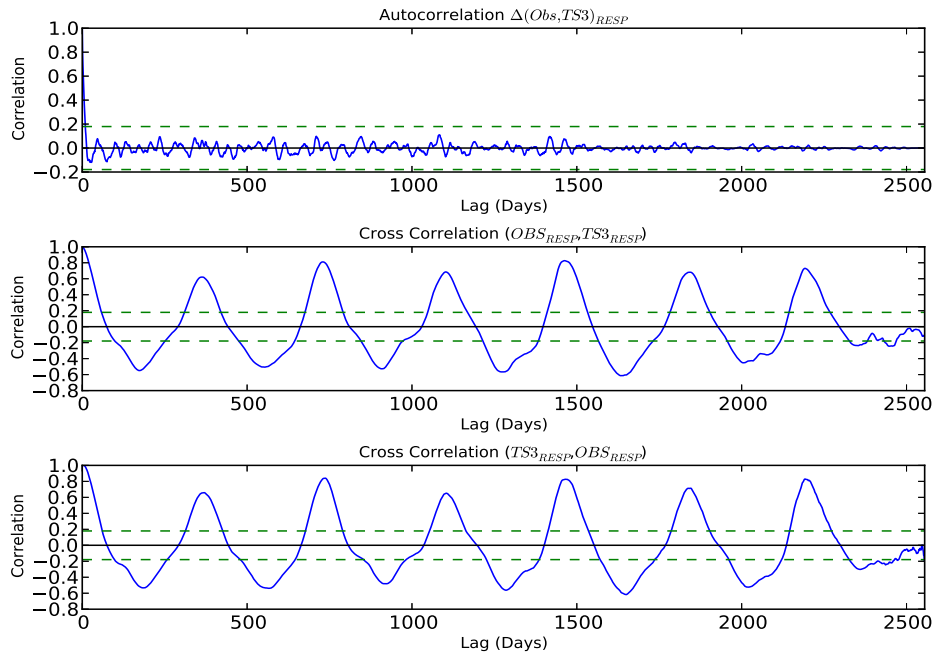


(B) Harvard Forest: RESP

FIG. 3.20. cross-correlation and Autocorrelation functions between the error time series of the control and time smoothing algorithm used in Experiment 3 for Harvard Forest. Top: GPP. Bottom: RESP. First Panel: Autocorrelation function of error time series. Middle Panel: Observations lag Time Smoothing Algorithm



(A) Vaira Ranch: GPP



(B) Vaira Ranch: RESP

FIG. 3.21. cross-correlation and Autocorrelation functions between observation and time smoothing estimation time series used in Experiment 3 for Vaira Ranch. Top: GPP. Bottom: RESP. First Panel: Autocorrelation function of error time series. Middle Panel: Observations lag Time Smoothing Algorithm

TABLE 3.1. Results of the suite of statistical tests performed on the data generated from Experiment 1. *P* means the statistical test rejected the null hypothesis and *F* means the statistical test failed to rejected the null hypothesis

(A) NEE

Site Name	Paired T-Test P-value	X-Corr (Control/TS) ΔZ_{crit} (Max, Mean, Min)	X-Corr (TS/Control) ΔZ_{crit} (Max, Mean, Min)	Autocorr (TS) ΔZ_{crit} (Max, Mean, Min)	Ljung-Box Test P-value	Mean Φ ($\bar{\Phi}$ k=1)
Harvard Forest	F 0.22	F < 0.01, 0.03, 0.87	F < 0.01, 0.04, 0.87	F < 0.01, 0.05, 0.91	P < 0.01	F 1.45, 1.36
U. of Mich. Biol. Stat.	F 0.15	F < 0.01, 0.08, 0.81	F < 0.01, 0.07, 0.81	F < 0.01, 0.08, 0.86	P < 0.01	P 1.67, 1.78
Old Black Spruce	F 0.39	F < 0.01, 0.05, 0.88	F < 0.01, 0.06, 0.88	P < 0.01, 0.11, 0.89	P < 0.01	P 1.36, 1.96
Campbell River	P < 0.01	F < 0.01, 0.05, 0.87	F < 0.01, 0.03, 0.87	P < 0.01, 0.12, 0.91	P < 0.01	P 0.42, 1.51
ARM-SGP	F 0.99	P 0.02, 0.38, 0.73	P 0.01, 0.37, 0.73	P < 0.01, 0.19, 0.85	P < 0.01	P 1.35, 2.14
Mead-Irrigated	F 0.94	F < 0.01, 0.08, 0.81	F < 0.01, 0.09, 0.81	F < 0.01, 0.10, 0.86	P < 0.01	P 0.57, 2.07
Vaira Ranch	P 0.05	F < 0.01, 0.06, 0.58	F < 0.01, 0.05, 0.72	F < 0.01, 0.17, 0.86	P < 0.01	F 3.74, 3.18
Lethbridge	F 0.63	F < 0.01, 0.07, 0.81	F < 0.01, 0.10, 0.81	P < 0.01, 0.10, 0.87	P < 0.01	P 2.59, 2.76

TABLE 3.2. Results of the suite of statistical tests performed on the data generated from Experiment 2. *P* means the statistical test rejected the null hypothesis and *F* means the statistical test failed to rejected the null hypothesis

(A) GPP

Site Name	Paired T-Test P-value	X-Corr (Obs/TS) ΔZ_{crit} (Max, Mean, Min)	X-Corr (TS/Obs) ΔZ_{crit} (Max, Mean, Min)	Autocorr (TS) ΔZ_{crit} (Max, Mean, Min)	Ljung-Box Test P-value	Mean Φ ($\bar{\Phi}$ k=1)
Harvard Forest	P < 0.01	F < 0.01, 0.39, 0.82	F < 0.01, 0.29, 0.82	F < 0.01, 0.12, 0.82	P < 0.01	F 14.97, 8.71
U. of Mich. Biol. Stat.	P 0.02	F < 0.01, 0.22, 0.62	F < 0.01, 0.23, 0.62	P 0.01, 0.31, 0.62	P < 0.01	P 8.47, 14.85
Old Black Spruce	F 0.14	F < 0.01, 0.33, 0.68	F < 0.01, 0.31, 0.68	F < 0.01, 0.15, 0.68	P < 0.01	P 15.93, 23.36
Campbell River	P < 0.01	F < 0.01, 0.37, 0.80	F < 0.01, 0.35, 0.83	P < 0.01, 0.15, 0.83	P < 0.01	F 21.38, 11.59
ARM-SGP	P 0.03	F < 0.01, 0.19, 0.39	F < 0.01, 0.18, 0.57	F < 0.01, 0.32, 0.64	P < 0.01	P 5.44, 12.71
Mead-Irrigated	P < 0.01	F < 0.01, 0.29, 0.67	F < 0.01, 0.28, 0.67	P < 0.01, 0.19, 0.67	P < 0.01	P 10.72, 14.32
Vaira Ranch	P < 0.01	F < 0.01, 0.40, 0.73	F < 0.01, 0.38, 0.70	P < 0.01, 0.22, 0.73	P < 0.01	P 12.28, 17.81
Lethbridge	P < 0.01	F < 0.01, 0.18, 0.76	F < 0.01, 0.25, 0.76	P 0.02, 0.36, 0.76	P < 0.01	P 8.81, 9.49

(B) RESP

Site Name	Paired T-Test P-value	X-Corr (Obs/TS) ΔZ_{crit} (Max, Mean, Min)	X-Corr (TS/Obs) ΔZ_{crit} (Max, Mean, Min)	Autocorr (TS) ΔZ_{crit} (Max, Mean, Min)	Ljung-Box Test P-value	Mean Φ ($\bar{\Phi}$ k=1)
Harvard Forest	P < 0.01	F < 0.01, 0.14, 0.56	P < 0.01, 0.19, 0.39	P 0.01, 0.29, 0.56	P < 0.01	P 12.63, 49.46
U. of Mich. Biol. Stat.	F 0.20	P < 0.01, < 0.01, < 0.01	P < 0.01, < 0.01, < 0.01	P < 0.01, < 0.01, < 0.01	P < 0.01	P 7.46, 68.68
Old Black Spruce	F 0.14	F < 0.01, 0.18, 0.46	F < 0.01, 0.18, 0.46	F 0.01, 0.24, 0.46	P < 0.01	P 14.12, 65.95
Campbell River	P < 0.01	F < 0.01, 0.28, 0.56	F < 0.01, 0.32, 0.70	P < 0.01, 0.17, 0.70	P < 0.01	P 21.70, 34.19
ARM-SGP	F 0.09	P < 0.01, 0.07, 0.11	P < 0.01, 0.07, 0.15	P < 0.01, 0.22, 0.40	P < 0.01	P 5.39, 32.69
Mead-Irrigated	P < 0.01	F < 0.01, 0.15, 0.31	F < 0.01, 0.14, 0.31	P 0.01, 0.18, 0.34	P < 0.01	P 9.05, 54.54
Vaira Ranch	P < 0.01	F < 0.01, 0.28, 0.58	F < 0.01, 0.26, 0.51	P 0.02, 0.30, 0.58	P < 0.01	P 12.59, 41.98
Lethbridge	F 0.38	P < 0.01, 0.09, 0.32	F < 0.01, 0.16, 0.32	P 0.03, 0.19, 0.32	P < 0.01	P 5.22, 68.65

(C) NEE

Site Name	Paired T-Test P-value	X-Corr (Control/TS) ΔZ_{crit} (Max, Mean, Min)	X-Corr (TS/Control) ΔZ_{crit} (Max, Mean, Min)	Autocorr (TS) ΔZ_{crit} (Max, Mean, Min)	Ljung-Box Test P-value	Mean Φ ($\bar{\Phi}$ k=1)
Harvard Forest	P < 0.01	P < 0.01, 0.04, 0.88	P < 0.01, 0.05, 0.88	P 0.12, 0.52, 0.92	P < 0.01	P 0.40, 0.95
U. of Mich. Biol. Stat.	P 0.02	P 0.01, 0.13, 0.75	P 0.75, 0.75, 0.75	P < 0.01, 0.20, 0.87	P < 0.01	P 0.47, 1.21
Old Black Spruce	P < 0.01	P < 0.01, 0.05, 0.88	P < 0.01, 0.06, 0.88	P < 0.01, 0.11, 0.89	P < 0.01	P 0.87, 1.58
Campbell River	P < 0.01	P < 0.01, 0.17, 0.84	P 0.01, 0.14, 0.84	P 0.07, 0.41, 0.92	P < 0.01	P 0.02, 1.21
ARM-SGP	P < 0.01	P 0.78, 0.78, 0.78	P 0.78, 0.78, 0.78	P 0.01, 0.32, 0.87	P < 0.01	P 0.16, 1.24
Mead-Irrigated	P < 0.01	F < 0.01, 0.07, 0.84	F < 0.01, 0.08, 0.84	P 0.12, 0.50, 0.88	P < 0.01	P 0.13, 1.20
Vaira Ranch	P < 0.01	P 0.29, 0.29, 0.29	P 0.01, 0.25, 0.72	P 0.06, 0.29, 0.89	P < 0.01	P 0.43, 1.73
Lethbridge	P < 0.01	P 0.05, 0.40, 0.76	P < 0.01, 0.10, 0.76	P < 0.01, 0.27, 0.90	P < 0.01	F 1.79, 1.41

TABLE 3.3. Results of the suite of statistical tests performed on the data generated from Experiment 3. *P* means the statistical test rejected the null hypothesis and *F* means the statistical test failed to rejected the null hypothesis

(A) GPP

Site Name	Paired T-Test P-value	X-Corr (Obs/TS) ΔZ_{crit} (Max, Mean, Min)	X-Corr (TS/Obs) ΔZ_{crit} (Max, Mean, Min)	Autocorr (TS) ΔZ_{crit} (Max, Mean, Min)	Ljung-Box Test P-value	Mean Φ ($\bar{\Phi}$ k=1)
Harvard Forest	P < 0.01	F < 0.01, 0.46, 0.89	F < 0.01, 0.47, 0.88	P < 0.01, 0.11, 0.89	P < 0.01	F 9.31, 2.63
U. of Mich. Biol. Stat.	P < 0.01	F < 0.01, 0.44, 0.85	F < 0.01, 0.46, 0.85	P 0.01, 0.12, 0.85	P < 0.01	F 6.02, 2.27
Old Black Spruce	P < 0.01	F < 0.01, 0.51, 0.90	F < 0.01, 0.50, 0.87	F < 0.01, 0.06, 0.90	P < 0.01	F 3.86, 1.56
Campbell River	P < 0.01	F < 0.01, 0.35, 0.92	F < 0.01, 0.31, 0.92	P 0.02, 0.29, 0.92	P < 0.01	F 4.40, 1.13
ARM-SGP	P < 0.01	F < 0.01, 0.37, 0.82	F < 0.01, 0.36, 0.82	F 0.01, 0.21, 0.82	P < 0.01	P 2.17, 3.28
Mead-Irrigated	P < 0.01	F < 0.01, 0.33, 0.78	F < 0.01, 0.33, 0.78	F < 0.01, 0.16, 0.78	P < 0.01	P 5.53, 6.32
Vaira Ranch	P < 0.01	F < 0.01, 0.45, 0.89	F < 0.01, 0.45, 0.89	P 0.01, 0.20, 0.89	P < 0.01	P 1.31, 1.83
Lethbridge	P < 0.01	F < 0.01, 0.26, 0.89	F < 0.01, 0.26, 0.89	P < 0.01, 0.12, 0.89	P < 0.01	F 6.68, 2.05

(B) RESP

Site Name	Paired T-Test P-value	X-Corr (Obs/TS) ΔZ_{crit} (Max, Mean, Min)	X-Corr (TS/Obs) ΔZ_{crit} (Max, Mean, Min)	Autocorr (TS) ΔZ_{crit} (Max, Mean, Min)	Ljung-Box Test P-value	Mean Φ ($\bar{\Phi}$ k=1)
Harvard Forest	P < 0.01	F < 0.01, 0.21, 0.68	F < 0.01, 0.18, 0.68	P 0.01, 0.33, 0.68	P < 0.01	P 8.97, 20.64
U. of Mich. Biol. Stat.	P < 0.01	F < 0.01, 0.30, 0.66	F < 0.01, 0.39, 0.66	P 0.01, 0.18, 0.66	P < 0.01	P 6.05, 12.58
Old Black Spruce	P < 0.01	F < 0.01, 0.48, 0.84	F < 0.01, 0.47, 0.84	P < 0.01, 0.10, 0.84	P < 0.01	P 4.14, 4.67
Campbell River	P < 0.01	F < 0.01, 0.42, 0.87	F < 0.01, 0.39, 0.87	P 0.01, 0.26, 0.87	P < 0.01	F 6.28, 3.90
ARM-SGP	P < 0.01	F < 0.01, 0.30, 0.76	F < 0.01, 0.18, 0.76	P < 0.01, 0.27, 0.76	P < 0.01	P 2.24, 5.77
Mead-Irrigated	P < 0.01	F < 0.01, 0.22, 0.54	F < 0.01, 0.20, 0.54	P < 0.01, 0.15, 0.54	P < 0.01	P 5.99, 27.24
Vaira Ranch	P < 0.01	F < 0.01, 0.34, 0.82	F < 0.01, 0.36, 0.82	P 0.01, 0.34, 0.82	P < 0.01	P 2.28, 5.51
Lethbridge	P < 0.01	F < 0.01, 0.28, 0.78	F < 0.01, 0.28, 0.78	P < 0.01, 0.33, 0.78	P < 0.01	P 4.21, 8.63

(C) NEE

Site Name	Paired T-Test P-value	X-Corr (Control/TS) ΔZ_{crit} (Max, Mean, Min)	X-Corr (TS/Control) ΔZ_{crit} (Max, Mean, Min)	Autocorr (TS) ΔZ_{crit} (Max, Mean, Min)	Ljung-Box Test P-value	Mean Φ ($\bar{\Phi}$ k=1)
Harvard Forest	P < 0.01	P < 0.01, 0.06, 0.82	P 0.01, 0.19, 0.82	P < 0.01, 0.15, 0.91	P < 0.01	P 1.23, 1.39
U. of Mich. Biol. Stat.	P 0.02	P < 0.01, 0.38, 0.75	P 0.01, 0.38, 0.75	P 0.01, 0.23, 0.87	P < 0.01	P 0.56, 1.13
Old Black Spruce	F 0.14	F < 0.01, 0.05, 0.91	P < 0.01, 0.04, 0.91	P < 0.01, 0.27, 0.91	P < 0.01	P 0.30, 1.02
Campbell River	P < 0.01	P < 0.01, 0.11, 0.86	P < 0.01, 0.11, 0.86	P 0.06, 0.40, 0.92	P < 0.01	P 0.09, 1.14
ARM-SGP	P 0.03	P < 0.01, 0.07, 0.79	P < 0.01, 0.09, 0.79	P 0.01, 0.15, 0.87	P < 0.01	P 0.21, 1.66
Mead-Irrigated	P < 0.01	F < 0.01, 0.07, 0.84	F < 0.01, 0.08, 0.84	P 0.12, 0.50, 0.88	P < 0.01	P 0.13, 1.58
Vaira Ranch	P < 0.01	P 0.23, 0.23, 0.23	P 0.01, 0.21, 0.72	P 0.03, 0.26, 0.89	P < 0.01	P 0.46, 1.91
Lethbridge	P < 0.01	P < 0.01, 0.37, 0.73	P 0.01, 0.12, 0.73	P < 0.01, 0.23, 0.90	P < 0.01	P 1.42, 1.57

CHAPTER 4

DISCUSSION

This section contains a discussion, interpretations, and conclusions regarding the time smoothing algorithm and the overarching hypotheses that the three experiments were designed to address. Table 4.1 shows a summary of the hypothesis conclusions from this and the results section.

4.1. EXPERIMENT 1 INTERPRETATIONS

The first experiment was an “apples-to-apples” comparison of the time smoothing algorithm and control algorithm on level terms. The visual results of the average annual source and sink plots gave the indication that this version of the time smoothing algorithm was capable of making an estimate of the annual and seasonal NEE signals as good or better than the control. Furthermore, the similar reduction of the RMSE of NEE time series suggested that the two time series were similarly fitted and could have similar source and sink fitting capabilities. However, this was not the case because the paired T-tests suggested that the interannual mean of the errors for this version of the time smoothing algorithm were greater than the control to within the 95th confidence bounds. The qualitative and quantitative evidence from experiment 1 suggests that a time smoothing algorithm is not capable of producing better estimates of interannual and annual NEE estimates than a present day algorithm. Thus, hypothesis 1 is rejected. Despite this finding, the seasonality was suggested to be well recovered.

From the seasonality analysis in the first experiment, the time smoothing algorithm was suggested to be capable of properly estimating the seasonal NEE signal at 6 of the 8 sites. While these were all below the 95th confidence interval, the estimates might not be truly robust as the statistics would require them to be. The four sites shown to contain only relative noise when

from the autocorrelation analysis all showed that the seasonal cycle was estimated by the time smoothing algorithm. This was not seen in the control algorithm for these sites. The inability to properly estimate the seasonal cycle across all sites was due to the fact that some of the NEE signals crossed zero suddenly and formulated shorter timescale harmonics than the were assumed. These are caused because of seasonal mismatches between the model and observations, which were not completely accounted for in the bias coefficient uncertainty. However, the general pattern of the sites with good estimates showed that given reasonable uncertainty estimates, the time smoothing algorithm could outperform the control algorithm at estimating the seasonality of NEE. Therefore, these results indicated that hypothesis 2 was either plausible or confirmed for any site given the optimization conditions and constraints.

The observational uncertainty analysis showed that the time smoothing algorithm was more robust than the control under increased uncertainty. As previously mentioned, the pattern from the results showed that the estimate would revert to the prior and progress toward the pre-assimilation model estimate as uncertainty increased. The time smoothing algorithm was more robust because of the “learning” nature inherent in the time smoothing algorithm. The design of the algorithm was such that if one year is much more certain than another, then an estimation of the bias coefficients could still be made under a large uncertainty. This cannot happen with the control because the posterior bias coefficient covariance matrix is not carried over between assimilation cycles. As a result, this evidence and the results of Experiment 1 validates the uncertainty criterion for hypotheses 1 and 2.

4.2. EXPERIMENT 2 INTERPRETATIONS

The second experiment showed the impact that the time smoothing algorithm using NEE to optimize for NEE estimates from GPP and RESP. Unlike the first experiment, using the time

smoothing algorithm in this manner demonstrated nearly exact recovery of the observed annually averaged and interannual patterns of NEE at every site to within error estimates of the observations. This result indicated the benefit of using the component fluxes over a standalone NEE flux estimate in the time smoothing algorithm. By using the slowly-varying component fluxes to formulate an NEE estimate, the smaller variations of NEE can still be present in the estimate. The sudden crosses between a source and a sink in the NEE signal can be accounted for by the two constantly non-negative component fluxes. The suite of statistical tests showed that NEE estimates optimized in this manner produced lower RMSE and achieved statistically better estimations of the annual NEE sources and sinks over the control algorithm across all sites. Furthermore, the mean power spectrum of NEE revealed that the seasonality is also confidently estimated by the algorithm. Therefore, the second experiment was able to confirm hypotheses 3 and 4.

The same conclusions for NEE are true for the estimation of the GPP and RESP fluxes from the second experiment, but are misleading. The second experiment showed that the cost to a highly accurate NEE signal was the warping of the two component fluxes. It was apparent from the spectral analysis that the harmonics were not indicative of the seasonal or mean harmonics, but rather the other optimized waves ($k = 2, 3, 4,$ and 5). While this may seem like poor behavior, this is the mathematical result of using the Kalman filter. The methodology is designed to make the best possible estimate with the information it was given. In the second experiment, the underlying mathematical principals are only concerned with fitting the NEE flux by optimizing the bias coefficients to make the best fit of NEE. Starting with the shortest harmonics, the optimization's methodology warps the the information in the modeled GPP and RESP fluxes in order to make an more accurate estimation of NEE. The presence of low seasonal and annual power in the error

confirms hypothesis 5. When summarized with the all estimates this confirmation is misleading because of a completely unrealistic estimate for either GPP or RESP.

The results of robustness tests for the second experiment indicated that this version of the time smoothing algorithm is very robust to changes in uncertainty over all sites. This is because the time smoothing algorithm is still able to capture the observed NEE flux by consistently warping the GPP and RESP fluxes in different manners to fit NEE, depending on the scenario. By examining the evolving time series, it was apparent that while some portions of component fluxes are being pulled toward the prior, others are being pulled toward the observations. This was caused by the mathematical balance between the confidence of the prior and observations during each assimilated year. This suggests that the bias coefficients are consistently changing over each assimilation cycle to compensate for individual mismatches in the GPP and RESP patterns. Since NEE is very robust over the all uncertainty increases and over all sites, the uncertainty criterion of hypotheses 3 and 4 is satisfied. Since GPP and RESP are almost constantly changing under various uncertainty scenarios, these estimates are not robust. Therefore, the uncertainty criterion for hypothesis 5 is not satisfied.

4.3. EXPERIMENT 3 INTERPRETATIONS

The third experiment demonstrated that it was possible to estimate all three fluxes given that observed NEE and a component flux are used as the constraining observational measurements. When using these two quantities, the time smoothing algorithm takes advantage of the optimization methodology wanting to make the best possible estimate with information it was given. In this case, the filter optimized for NEE and GPP fluxes. By design, this experiment was capable of recovering all three fluxes due to the intimate nature of the net and component fluxes.

The conclusions for NEE are similar to that of the second experiment. The slightly worse NEE RMSE was caused by the addition of the observed GPP as an additional constraint. The annual averages, fractional RMSE reduction, and the paired T-test for the NEE estimates revealed that this version of the optimization produced better annual NEE averages than the control and comparable values to that of the second experiment. The issues found at Old Black Spruce were due to numerical instability of the bias coefficient covariance matrix and not the design of the theory itself. Therefore, the third experiment was able to confirm hypothesis 6. Additionally, the mean spectral and autocorrelation analyses suggested that the residual error term of the time smoothing estimate was completely red noise for all sites. This means that both the mean and seasonal cycles were well-estimated. Thus, the third experiment was able to confirm hypothesis 7.

The addition of an extra observational constraint allowed for GPP and RESP to be properly estimated for most sites. Visually, the time series estimates showed that GPP and RESP are well fit from the third experiment. The presence of a reduction in RMSE across most sites showed improvement from the pre-assimilation flux estimates. Furthermore, the nearly indistinguishable flux time series from the autocorrelation functions indicated that the observations and the component flux estimates were nearly identical. The mean spectral analysis of RESP proved that across all sites both the mean and seasonal cycles of RESP were well resolved. The spectral analysis of GPP showed that some of the sites were incapable of sub-red noise estimation. While statistically significant, this may be irrelevant because the power retrieved by mean spectrum is very low across all sites. The spectral power of GPP is only about a quarter to a half of that produced by the second experiment. From these results, it was seen that GPP and RESP were both well-estimated by the third experiment. Therefore, the third experiment confirmed hypothesis 8.

Like the second experiment, this version of time smoothing algorithm showed a robust retrieval of annually averaged and daily NEE fluxes under increases in uncertainty estimates across a variety of PFTs. The rate at which the fluxes revert to the prior fluxes occurs sooner for some sites than others. Like the first experiment, this is because the initial observational uncertainty for some sites is greater than it is for others. This experiment was able to produce more robust estimates than the control algorithm and reverted toward the pre-assimilation flux only slightly sooner than the second experiment. When applied to the GPP and RESP signals, the increasing uncertainty did not produce the same results as the second experiment. As the observational uncertainty increased, GPP tended to revert toward the prior estimate, but RESP was still able to be well-estimated. This pattern kept the NEE estimate relatively well constrained and robust. In summary, this suggested that the uncertainty criterion for GPP, RESP, and NEE in hypotheses 6, 7, and 8 were all met.

TABLE 4.1. A summary of the conclusions about whether the hypotheses were accepted (A) or rejected (R). The uncertainty criteria conclusions were denoted as satisfied (S) or unsatisfied (U)

(A) Experiment 1

Hypothesis 1	Hypothesis 2	Uncertainty Criteria NEE
R	C	S

(B) Experiment 2

Hypothesis 3	Hypothesis 4	Hypothesis 5	Uncertainty Criteria NEE	Uncertainty Criteria GPP/RESP
C	C	C	S	U

(C) Experiment 3

Hypothesis 6	Hypothesis 7	Hypothesis 8	Uncertainty Criteria NEE	Uncertainty Criteria GPP/RESP
C	C	C	S	S

CHAPTER 5

CONCLUSIONS AND FUTURE WORK

The purpose of this study was to create a new inversion framework capable of characterizing and adapting to the long-lived biases between land-atmosphere model gross CO₂ fluxes and observations. This study has shown that in order to do this both the Kalman filter and harmonics can be used to smooth the modeled flux estimates in time to diagnose these long-lived biases. Several PFTs over a range of climate regimes showed that the largest sources of error between model simulations and observations were attributed to low wavenumbers that consist of discrepancies in the “slow-varying” model variables. These results were applied to the time smoothing algorithm with a yearly assimilation cycles through three different experiments.

These experiments demonstrated that using a small number of harmonics with greater observational data constraints can produce as good or better estimates of net sources and sinks of CO₂ than a comparable weekly assimilation algorithms. The first experiment produced NEE estimates that were unable to be more accurate annual source and sink estimates over a control algorithm when using observed NEE to optimize estimated NEE. However, this experiment showed the time smoothing algorithm was capable of being more robust to increased observational uncertainty estimates and produced good seasonality estimates of NEE. The second experiment concluded that when using the component fluxes to make an estimate of NEE that is optimized by NEE observations, there is a dramatic increase in the accuracy of both the magnitude and interannual/seasonal cycles of NEE over just using modeled NEE itself. This accuracy came at the price of a poor recovery of the two component fluxes for sub-seasonal harmonics, but the NEE estimate was very robust over several observational uncertainty increases. The third experiment found that when an observed component flux is used to further constrain the time smoothing algorithm, all three fluxes

are well fit on all timescales over a variety observational uncertainty increases. For all variants of the time smoothing algorithm, the posterior estimation was able to overcome seasonal phase shifts, crop and harvest mistimings, and flux magnitude errors present in the prior model fluxes. Given there are improvements with better observations and uncertainty estimates, this algorithm could one day serve to understand the errors and biases present in land-atmosphere model estimates and how ecosystems behave under different biological circumstances.

There will be several improvements to this work in future studies. One way will be to both improve this assimilation algorithm and to apply it in a more general sense. This can be done by incorporating more eddy-covariance data over an even wider assortment of climates to truly obtain the strengths and weaknesses of this algorithm. One adjustment to the algorithm should include a consistent way of estimating the number of harmonics needed for optimization. An example to estimate this number of harmonics required may be the usage of variance explained by the observation-model errors to set a parameter as a cut off point between slow and fast harmonics. This would keep the number of resolved harmonics to minimum number of slow processes. Another adjustment would be a better way to estimate the uncertainty of the land model. Since this study revolved around an assumption that modeled RESP and GPP did not covary with one another, future studies must make a more realistic assumption and relate these two quantities. A third update would be to address the observational uncertainty matrix. Introduction of a more thorough covariance matrix where the proper relations between NEE and the component flux would dramatically increase the robustness and accuracy of this algorithm beyond its tested capabilities. A final update would be to design an algorithm to adjust the tuning parameter of the covariance update step in such a way so that the model uncertainty matrix does not converge and skew or break the bias coefficient adjustments. A robust way is to use some sort normalized difference between the

model and observations to give a general idea of how uncertain the model is to begin with and how our initial conditions should be shaped.

Future applications of this algorithm should be to apply it to multiple land-atmosphere models to see how and where these biases exist. Traditionally, these models are balanced on an annual basis, which makes the three gross fluxes all interconnected within the theory and application. Isolation of a variety of slowly-varying and poorly understood parameters should be chosen as the implementation points for this algorithm's influence. Improvements in land-atmosphere models are always happening and with these improvements land-atmosphere models can hopefully produce better *a priori* flux estimates for future inversion model simulations of regional and global sources and sinks of CO₂.

REFERENCES

- Baker, D. F., et al., 2006: TransCom 3 inversion intercomparison: Impact of transport model errors on the interannual variability of regional CO₂ fluxes, 19882003. *Global Biogeo. Cyc.*, **20**, GB1002.
- Baker, I. T., L. Prihodko, A. S. Denning, M. Goulden, S. Miller, and H. R. da Rocha, 2008: Seasonal Drought Stress in the Amazon: Reconciling Models and Observations. *J. Geophys. Res.*, **113**, G00B01, doi:10.1029/2007JG000644.
- Bakwin, P. S., P. P. Tans, D. F. Hurst, and C. Zhao, 1998: Measurements of carbon dioxide on very tall towers: Results of the NOAA/CMDL program. *Tellus*, **50B**, 401–415.
- Baldocchi, D., 2008: ‘breathing’ of the terrestrial biosphere: Lessons learned from a global network of carbon dioxide flux measurement systems. *Aust. J. Bot.*, **56**, 1–26.
- Baldocchi, D. and Coauthors, 2001: FLUXNET: A New Tool to Study the Temporal and Spatial Variability of Ecosystem Scale Carbon Dioxide, Water Vapor, and Energy Flux Densities. *Bull. Amer. Meteor. Soc.*, **82**, 2415–2434.
- Ball, J. T., 1988: An analysis of stomatal conductance. Ph.D. thesis, Stanford University.
- Barr, A. G., T. A. Black, E. H. Hogg, N. Kljun, K. Morgenstern, and Z. Nestic, 2004: Inter-annual Variability in the Leaf Area Index of a Boreal Aspen-Hazelnut Forest in Relation to Net Ecosystem Production. *Agric. For. Meteorol.*, **126**, 237–255, doi:10.1016/j.agrformet.2004.06.011.
- Barr, A. G., et al., 2013: NACP Site: Tower Meteorology, Flux Observations with Uncertainty, and Ancillary Data [Dataset]. URL <http://daac.ornl.gov>.
- Bolin, B. and W. Bischoff, 1970: Variations of the carbon dioxide content of the atmosphere in the northern hemisphere. *Tellus*, **22**, 431–442.
- Bolin, B. and E. Eriksson, 1958: *Changes in the Carbon Dioxide Content of the Atmosphere and Sea due to Fossil Fuel Combustion*. The Rockefeller Int. Press, New York, NY, USA.
- Bolin, B. and C. D. Keeling, 1963: Large scale atmospheric mixing as deduced from the seasonal and meridional variations in carbon dioxide. *J. Geophys. Res.*, **68**, 3899.
- Bonan, G. B., S. Levis, L. Kergoat, and K. W. Oleson, 2002: Landscapes as patches of plant functional types: An integrating concept for climate and ecosystem models. *Global Biogeo. Cyc.*, **16**, 1021, doi:10.1029/2000GB001360.
- CarbonTracker, 2014: *CarbonTracker Documentation CT2013 Release*. ESRL.
- Chevallier, F., S. Maksyutov, P. Bousquet, F.-M. Bréon, R. Saito, Y. Yoshida, and T. Yokota, 2009: On the accuracy of the CO₂ surface fluxes to be estimated from the GOSAT observations.

- Geophys. Res. Lett.*, **36**, L19 807, doi:10.1029/2009GL040108.
- Ciais, P., P. P. Tans, M. Trolier, J. W. C. White, and R. J. Francey, 1995: A large northern hemisphere terrestrial CO₂ sink indicated by the ¹³C/¹²C ratio of atmospheric CO₂. *Science*, **269**, 1098–1102.
- Collatz, G. J., J. Ball, C. Grivet, and J. A. Berry, 1991: Physiological and environmental regulation of stomatal conductance, photosynthesis and transpiration: a model that includes a laminar boundary layer. *Agric. For. Meteorol.*, **54**, 107–136.
- Collatz, G. J., M. Ribas-Carbo, and J. A. Berry, 1992: Coupled Photosynthesis-Stomatal Conductance Model for Leaves of C₄ Plants. *Aust. J. Plant Physiol.*, **19**, 519–513.
- Denning, A. S., J. Collatz, C. Zhang, D. Randall, J. Berry, P. Sellers, G. Colello, and D. Dazlich, 1996: Simulations of terrestrial carbon metabolism and atmospheric CO₂ in a general circulation model. Part 1: Surface carbon fluxes. *Tellus*, **48B**, 521–542.
- Denning, A. S., et al., 1999: Three-dimensional transport and concentration of SF₂: A model intercomparison study (TransCom 2). *Tellus*, **51B**, 266–297.
- Desai, A. R., et al., 2008: Cross-site evaluation of eddy covariance GPP and RE decomposition techniques. *Agric. For. Meteorol.*, **148**, 821 – 383, doi:10.1016/j.agrformet.2007.11.012.
- Drever, J. I., 1988: *The Geochemistry of Natural Waters*. Prentice Hall, Englewood Cliffs, NJ, USA.
- ESRL, 2014: Earth System Research Laboratory Global Monitoring Division: Up-to-Date Weekly Average CO₂ at Mauna Loa. URL <http://www.esrl.noaa.gov/gmd/ccgg/trends/weekly.html>.
- Evensen, G., 1994: Sequential data assimilation with a nonlinear quasi-geostrophic model using Monte Carlo methods to forecast error statistics. *J. Geophys. Res.*, **99**, 10 143–10 162.
- Evensen, G., 2009: *Data Assimilation: The Ensemble Kalman Filter*. 2d ed., Springer-Verlag, 307 pp.
- Farquhar, G. D., S. von Caemmerer, and J. A. Berry, 1980: A Biochemical Model of Photosynthetic CO₂ Assimilation in Leaves of C₃ Species. *Planta*, **149**, 78–90.
- Fischer, M. L., D. P. Billesbach, W. J. Riley, J. A. Berry, and M. S. Torn, 2007: Spatiotemporal Variations in Growing Season Exchanges of CO₂, H₂O, and Sensible Heat in Agricultural Fields of the Southern Great Plains. *Earth Interact.*, **11**, 1–21, doi:10.1175/EI231.1.
- Flanagan, L. B. and A. C. Adkinson, 2011: Interacting Controls on Productivity in a Northern Great Plains Grassland and Implications for Response to ENSO Events. *Global Change Biology*, **17**, 3239–3311, doi:10.1111/j.1365-2486.2011.02461.x.

- Friedlingstein, P., et al., 2006: Climate-Carbon Cycle Feedback Analysis: Results from the C⁴MIP Model Intercomparison. *J. Climate*, **19**, 3337–3353.
- Gough, C. M., C. S. Vogel, H. P. Schmid, H.-B. Su, and P. S. Curtis, 2008: Multi-year Convergence of Biometric and Meteorological Estimates of Forest Carbon Storage. *Agric. For. Meteorol.*, **148**, 158–170, doi:10.1016/j.agrformet.2007.08.004.
- Gurney, K. R. and A. S. Denning, 2007: TransCom 3: Annual Mean CO₂ Flux Estimates from Atmospheric Inversions (Level 1). URL http://daac.ornl.gov/cgi-bin/dsvviewer.pl?ds_id=895, doi:10.3334/ORNLLDAAC/895.
- Gurney, K. R., et al., 2002: Towards Robust Regional Estimates of CO₂ Sources and Sinks Using Atmospheric Transport Models. *Nature*, **415**, 626–630.
- Gurney, K. R., et al., 2004: Transcom 3 Inversion Intercomparison: Model Mean Results for the Estimation of Seasonal Carbon Sources and Sinks. *Global Biogeochem. Cyc.*, **18**, GB1010, doi:10.1029/2003GB002111.
- Haynes, K. D., I. T. Baker, A. S. Denning, R. Stöckli, K. Schaefer, and E. Lokupitiya, 2013: Global Self Consistent Carbon Flux and Pool Estimates Utilizing the Simple Biosphere Model (SiB4). *Abstract B31F-01 presented at 2013, Fall Meeting, AGU*.
- Hoffman, F. M., et al., 2014: Causes and implications of persistent atmospheric carbon dioxide biases in Earth System Models. *J. Geophys. Res. Biogeosci.*, **119**, doi:10.
- Houghton, R. A., 1999: The annual net flux of carbon to the atmosphere from changes in land use 1850-1990. *Tellus*, **51B**, 298–313.
- Hurt, G. and C. Kang, 2014: *NASA Carbon Monitoring System Phase 1 Report*. NOAA.
- IPCC, 2013: *Climate Change 2013: The Physical Science Basis. Contribution of Working Group I to the Fifth Assessment Report of the Intergovernmental Panel on Climate Change*. Cambridge University Press, Cambridge, United Kingdom and New York, NY, USA.
- Jolly, W. M., R. Nemani, and S. W. Running, 2005: An analysis of stomatal conductance. *Global Change Biol.*, **11**, 619–632.
- Kaminski, T., M. Heimann, and R. Giering, 1999: A coarse grid three-dimensional global inverse model of the atmospheric transport: 2. Inversion of the transport of CO₂ in the 1980s. *J. Geophys. Res.*, **104**, 18 555–18 582.
- Kawa, S. R., D. J. E. III, S. Pawson, and Z. Zhu, 2004: Global CO₂ transport simulations using meteorological data from the NASA data assimilation system. *J. Geophys. Res.*, **109**, D18 312, doi:10.1029/2004JD004554.

- Kljun, N., T. A. Black, T. J. Griffis, A. G. Barr, D. Gaumont-Guay, K. Morgenstern, J. H. McCaughey, and Z. Nestic, 2006: Response of Net Ecosystem Productivity of Three Boreal Forest Stands to Drought. *Ecosystems*, **9**, 1128–1144.
- Krishnan, P., T. A. Black, A. G. Barr, N. J. Grant, D. Gaumont-Guay, and Z. Nestic, 2008: Factors Controlling the Interannual Variability in the Carbon Balance of a Southern Boreal Black Spruce Forest. *J. Geophys. Res.*, **113**, D09 109, doi:10.1029/2007JD008965.
- Krishnan, P., T. A. Black, A. Jassal, B. Chen, and Z. Nestic, 2009: Interannual variability of the carbon balance of three different-aged Douglas-fir stands in the Pacific Northwest. *J. Geophys. Res.*, **114**, G04 011, doi:10.1029/2008JG000912.
- Law, R. M., et al., 1996: Variations in modeled atmospheric transport of carbon dioxide and the consequences for CO₂ inversions. *Global Biogeo. Cyc.*, **10**, 783–796.
- Ljung, G. and G. Box, 1978: On a Measure of Lack of Fit in Time Series Models. *Biometrika*, **65**, 297–303.
- Lokupitiya, E., et al., 2009: Incorporation of Crop Phenology in Simple Biosphere Model (SiBcrop) to Improve Land Atmosphere Carbon Exchanges from Croplands. *Biogeosci.*, **6**, 969–986.
- Lokupitiya, R. S., D. Zupanski, A. S. Denning, S. R. Kawa, K. R. Gurney, , and M. Zupanski, 2008: Estimation of global CO₂ fluxes at regional scale using the Maximum Likelihood Ensemble Filter. *J. Geophys. Res.*, **113**, D20 110, doi:10.1029/2007JD009679.
- Ma, S., D. D. Baldocchi, L. Xu, and T. Hehn, 2007: Inter-annual Variability in Carbon Dioxide Exchange of an oak/grass Savanna and Open Grassland in California. *Agric. For. Meteorol.*, **147**, 157–171, doi:10.1016/j.agrformet.2007.07.008.
- Michalak, A. M., 2008: Adapting a fixed-lag Kalman smoother to a geostatistical atmospheric inversion framework. *Atmos. Chem. Phys.*, **8**, 6789–6799.
- Michalak, A. M., L. Bruhwiler, and P. P. Tans, 2004: A Geostatistical Approach to Surface Flux Estimation of Atmospheric Trace Gases. *J. Geophys. Res.*, **109**, D14 109.
- Moffat, A. M., et al., 2007: Comprehensive comparison of gap-filling techniques for eddy covariance net carbon fluxes. *Agric. For. Meteorol.*, **147**, 209 – 232, doi: 10.1016/j.agrformet.2007.08.011.
- Peters, W., et al., 2007: An Atmospheric Perspective on North American Carbon Dioxide Exchange: CarbonTracker. *Proceedings of the National Academy of Sciences of the United States of America*, **104**, 18 925–18 930.
- Peters, W., et al., 2010: Seven years of recent European net terrestrial carbon dioxide exchange constrained by atmospheric observations. *Global Change Biology*, **16**, 1317–1337.

- Portland State Aerospace Society, 2011: Kalman intro. URL <http://psas.pdx.edu/KalmanIntro/>.
- Richardson, A. D. and D. Y. Hollinger, 2007: A method to estimate the additional uncertainty in gap-filled NEE resulting from long gaps in the CO₂ flux record. *Agric. For. Meteor.*, **147**, 199–208, doi:10.
- Rödenbeck, C., S. Houweling, M. Gloor, and M. Heimann, 2003: CO₂ flux history 1982-2001 inferred from atmospheric data using a global inversion of atmospheric transport. *Atmos. Chem. Phys.*, **3**, 1919–1964.
- Sabine, C. L., et al., 2004: The Oceanic Sink for Anthropogenic CO₂. *Science*, **305**, 367–371.
- Schaefer, K., et al., 2012: A model-data comparison of gross primary productivity: Results from the north american carbon program site synthesis. *J. Geophys. Res.*, **117**, doi: 10.1029/2012JG001960.
- Schuh, A. E., A. S. Denning, K. D. Corbin, I. T. Baker, M. Uliasz, N. Parazoo, A. E. Andrews, and D. E. J. Worthy, 2010: A regional high-resolution carbon flux inversion of North America for 2004. *Biogeosciences*, **7**, 1625–1644.
- Schuh, A. E., A. S. Denning, M. Uliasz, and K. D. Corbin, 2009: Seeing the forest through the trees: Recovering large-scale carbon flux biases in the midst of small-scale variability. *J. Geophys. Res.*, **114**, G03 007, doi:10.1029/2008JG000842.
- Schuh, A. E., et al., 2013: Evaluating atmospheric CO₂ inversions at multiple scales over a highly-inventoried agricultural landscape. *Global Change Biology*, **19**, 1424–1439, doi: 10.1111/gcb.12141.
- Sellers, P. J., S. O. Los, C. J. Tucker, C. O. Justice, D. A. Dazlich, G. J. Collatz, and D. A. Randall, 1996a: A Revised Land Surface Parameterization (SiB2) for Atmospheric GCMs. Part II: The Generation of Global Fields of Terrestrial Biophysical Parameters from Satellite Data. *J. Climate*, **9**(4), 706–737.
- Sellers, P. J., Y. Mintz, Y. C. Sud, and A. Dalcher, 1986: A Simple Biosphere Model (SiB) for Use within General Circulation Models. *J. Atmos. Sci.*, **275**, 502–509.
- Sellers, P. J., Y. Mintz, Y. C. Sud, and A. Dalcher, 1992: Canopy Reflectance, Photosynthesis, and Transpiration. III. A Reanalysis Using Improved Leaf Models and a New Canopy Integration Scheme. *Rem. Sens. Enviro.*, **42**, 187–216.
- Sellers, P. J., et al., 1996b: A Revised Land Surface Parameterization (SiB2) for Atmospheric GCMs Part I: Model Formulation. *J. Climate*, **9**, 676–705.

- Stöckli, R., T. Rutishauser, I. Baker, M. A. Liniger, and A. S. Denning, 2011: A global reanalysis of vegetation phenology. *J. Geophys. Res.*, **116**, G03 020, doi:10.1029/2010JG001545.
- Stöckli, R., T. Rutishauser, P. E. Thornton, L. Lu, and A. S. Denning, 2008: Remote sensing data assimilation for a prognostic phenology model. *J. Geophys. Res.*, **113**, G04 021, doi: 10.1029/2008JG000781.
- Suyker, A. E. and S. B. Verma, 2010: Coupling of Carbon Dioxide and Water Vapor Exchanges of Irrigated and Rainfed Maize-Soybean Cropping Systems and Water Productivity. *Agric. For. Meteorol.*, **150**, 553563, doi:10.1016/j.agrformet.2010.01.020.
- Tans, P. P., I. Y. Fung, and T. Takahashi, 1990: Observational Constraint on the Global Atmospheric CO₂ Budget. *Science*, **247**, 1431–1438.
- UNH, 2014: Pools, Fluxes, and a Word about Units. URL <http://globecarboncycle.unh.edu/CarbonPoolsFluxes.shtml>.
- Urbanski, S., et al., 2007: Factors Controlling CO₂ Exchange on Timescales from Hourly to Decadal at Harvard Forest. *J. Geophys. Res.*, **112**, G02 020, doi:10.1029/2006JG000293.
- Verma, S. B., et al., 2005: Annual Carbon Dioxide Exchange in Irrigated and Rainfed Maize-based Agroecosystems. *Agric. For. Meteorol.*, **131**, 77–96, doi:10.1016/j.agrformet.2005.05.003.
- Welch, G. and G. Bishop, 2006: An Introduction to the Kalman Filter. University of North Carolina at Chapel Hill, Available online at http://www.cs.unc.edu/welch/media/pdf/kalman_intro.pdf.
- Zhang, F., C. Snyder, and J. Sun, 2004: Impacts of Initial Estimate and Observation Availability on Convective-Scale Data Assimilation with an Ensemble Kalman Filter. *Mon. Wea. Rev.*, **132**, 1238–1253, doi:[http://dx.doi.org/10.1175/1520-0493\(2004\)132\(1238:IOIEAO\)2.0.CO;2](http://dx.doi.org/10.1175/1520-0493(2004)132(1238:IOIEAO)2.0.CO;2).
- Zupanski, D., et al., 2007: Carbon flux bias estimation employing Maximum Likelihood Ensemble Filter (MLEF). *J. Geophys. Res.*, **112**, D17 107, doi:10.1029/2006JD008371.

APPENDIX A

KALMAN FILTER DERIVATION

The inversion method used for this study of the Kalman filter. The equations used the bias coefficient estimates in this study are as follows

$$\vec{\beta}_t^{pre} = \mathbf{A}_{t-1} \vec{\beta}_{t-1}^{upd} + \mu_t \quad (\text{A.1})$$

$$\mathbf{C}_{\beta,t}^{pre} = \mathbf{A}_{t-1}^T \mathbf{C}_{\beta,t-1}^{upd} \mathbf{A}_{t-1} + \mathbf{Q}_{t-1} \quad (\text{A.2})$$

$$\mathbf{K}_t = \frac{\mathbf{C}_{\beta,t}^{pre} \mathbf{G}_t^T}{\mathbf{C}_{d,t} + \mathbf{G}_t^T \mathbf{C}_{\beta,t}^{pre} \mathbf{G}_t} \quad (\text{A.3})$$

$$\vec{\beta}_t^{upd} = \vec{\beta}_t^{pre} + \mathbf{K}_t (\mathbf{d}_t - \mathbf{G}_t \vec{\beta}_t^{pre}) \quad (\text{A.4})$$

$$\mathbf{C}_{\beta,t}^{upd,*} = (\mathbf{I} - \mathbf{K}_t \mathbf{G}_t)^T \mathbf{C}_{\beta,t}^{pre} (\mathbf{I} - \mathbf{K}_t \mathbf{G}_t) + \mathbf{K}_t^T \mathbf{C}_{d,t} \mathbf{K}_t \quad (\text{A.5})$$

$$\mathbf{C}_{\beta,t}^{upd,*} = \mathbf{C}_{\beta,t}^{upd,*}(w) + \mathbf{C}_{\beta,t}^{pre}(1-w) \quad (\text{A.6})$$

This appendix will present a discussion of the derivation of all equations presented above. The derivation presented here follows the work of Evensen (2009), Welch and Bishop (2006) and Portland State Aerospace Society (2011). All variables and their meaning will be presented in text and in Table A.1 for reference.

A.1. BAYES THEOREM AND ASSUMPTIONS

At its core, the Kalman filter is a recursive linear Gauss-Markov least-squares unbiased estimator of a state parameter given some observations. A state parameter is a variable that a system of equations is dependent upon and can be used to predict the future behavior of the system (Evensen

2009). In this study, the state parameters are the bias coefficients (β) between the observed and modeled fluxes.

The Kalman filter derived in this study begins by stating Bayes Theorem given as

$$P(\vec{\beta}|\mathbf{d}) = \frac{P(\vec{\beta})P(\mathbf{d}|\vec{\beta})}{P(\mathbf{d})} \quad (\text{A.7})$$

$$P(\vec{\beta}|\mathbf{d}) \propto P(\vec{\beta})P(\mathbf{d}|\vec{\beta}) \quad (\text{A.8})$$

where $\vec{\beta}$ is a vector of bias coefficient estimates and \mathbf{d} is a matrix of flux observations. In this study, Bayes Theorem states that the *a posteriori* cumulative probability distribution, or likelihood, of the bias coefficients estimates given a set of flux observations ($P(\vec{\beta}|\mathbf{d})$) is proportional to the *a priori* probability distribution of the bias coefficient estimates ($P(\vec{\beta})$) and the likelihood of the flux observations given the *a priori* bias coefficient estimates ($P(\mathbf{d}|\vec{\beta})$) (Evensen 2009; Welch and Bishop 2006).

From Bayes Theorem, the first two assumptions are that the estimate is linear and a Markovian process. This means that the new state estimate at the current assimilation time, t , is a linear transition solely dependent upon the most recent state estimate at assimilation time, $t-1$. Furthermore, the observations at the concurrent assimilation time, t , are a linear function of the true state and a Jacobian matrix, which maps the state from state to observational space with some error. For this study, these assumptions are given by

$$\vec{\beta}_t^{pre} = \mathbf{A}_{t-1}\vec{\beta}_{t-1}^{upd} + \mu_t \quad (\text{A.9})$$

$$\mathbf{d}_t = \mathbf{G}_t\vec{\beta}_t^{true} + \nu_t \quad (\text{A.10})$$

where $\vec{\beta}_t^{pre}$ is the predicted bias coefficient estimates at the current assimilation time, $\vec{\beta}_{t-1}^{upd}$ is the updated, or *a posteriori*, bias coefficient estimates from the previous assimilation time, $\vec{\beta}_t^{true}$ is the true value of the bias coefficients at the current assimilation time, A_{t-1} is the transition matrix to map the bias coefficients from the previous assimilation time to the current time, μ_t is some white noise error in the bias coefficient estimates between assimilation times, G_t is the Jacobian matrix that maps the bias coefficient estimates to the flux observations and ν_t is the error in the flux observations at the current assimilation time. As can be seen, equation is equivalent to equation (A.1), which is the state prediction equation of the Kalman filter for the bias coefficients.

The third assumption is that the probability density functions of both the state estimates and the observations are Gaussian and the errors between them are uncorrelated. Under this assumption, the expectation of the errors in the bias coefficient estimates, noise terms, and flux observations are the following

$$E[(\vec{\beta}_t^{true} - \vec{\beta}_t)^2] = \mathbf{C}_{\beta,t} \quad (\text{A.11})$$

$$E[(\mu_t)^2] = \mathbf{Q}_t \quad (\text{A.12})$$

$$E[\nu_t^2] = \mathbf{C}_{d,t} \quad (\text{A.13})$$

$$E[\mu\nu] = E[\mu] = E[\nu] = 0 \quad (\text{A.14})$$

Here “E” indicates the expectation of a variable, \mathbf{Q}_t is the transition noise covariance matrix of bias coefficient estimates, $\mathbf{C}_{d,t}$ is the observational covariance matrix and \mathbf{C}_{β} is the covariance matrix of the bias coefficient estimates. From these assumptions, the next step is use the equations above to define the probability of the bias coefficient estimates from the proportionality statement equation (A.8). As previously stated, the probability density functions of all terms are Gaussian.

Therefore, the three terms in equation (A.8) are defined as follows

$$\begin{aligned}
P(\vec{\beta}_t^{upd} | \vec{\beta}_t^{pre}) &\equiv \mathcal{N}(\vec{\beta}_t^{pre}, \mathbf{C}_\beta) \\
&= \frac{1}{\sqrt{(2\pi)^k |\mathbf{C}_\beta|}} e^{-\frac{1}{2}(\vec{\beta}_t^{upd} - \vec{\beta}_t^{pre})^T \mathbf{C}_\beta^{-1} (\vec{\beta}_t^{upd} - \vec{\beta}_t^{pre})}
\end{aligned} \tag{A.15}$$

$$\begin{aligned}
P(\mathbf{d}_t | \mathbf{G}_t \vec{\beta}_t^{upd}, \mathbf{C}_{d,t}) &\equiv \mathcal{N}(\mathbf{G}_t \vec{\beta}_t^{upd}, \mathbf{C}_{d,t}) \\
&= \frac{1}{\sqrt{(2\pi)^k |\mathbf{C}_{d,t}|}} e^{-\frac{1}{2}(\mathbf{d}_t - \mathbf{G}_t \vec{\beta}_t^{upd})^T (\mathbf{C}_{d,t})^{-1} (\mathbf{d}_t - \mathbf{G}_t \vec{\beta}_t^{upd})}
\end{aligned} \tag{A.16}$$

$$P(\vec{\beta}_t^{upd} | \mathbf{d}_t, \mathbf{C}_{d,t}) \propto P(\vec{\beta}_t^{upd} | \vec{\beta}_t^{pre}) P(\mathbf{d}_t | \mathbf{G}_t \vec{\beta}_t^{upd}) \tag{A.17}$$

$$P(\vec{\beta}_t^{upd} | \mathbf{d}_t, \mathbf{C}_{d,t}) \propto e^{-\frac{1}{2}[(\vec{\beta}_t^{upd} - \vec{\beta}_t^{pre})^T \mathbf{C}_\beta^{-1} (\vec{\beta}_t^{upd} - \vec{\beta}_t^{pre}) + (\mathbf{d}_t - \mathbf{G}_t \vec{\beta}_t^{upd})^T (\mathbf{C}_{d,t})^{-1} (\mathbf{d}_t - \mathbf{G}_t \vec{\beta}_t^{upd})]} \tag{A.18}$$

From equation (A.18), the *a posteriori* likelihood of the bias coefficient estimates given flux observations is determined by a term in the exponential known as the cost function. The cost function is a balance between the deviation of the updated estimate from the predicted state given some uncertainty estimate and the deviation of the observational estimate from the real observations given some uncertainty in the real observations. The cost function is given as

$$\Psi = \left[(\vec{\beta}_t^{upd} - \vec{\beta}_t^{pre})^T \mathbf{C}_\beta^{-1} (\vec{\beta}_t^{upd} - \vec{\beta}_t^{pre}) + (\mathbf{d}_t - \mathbf{G}_t \vec{\beta}_t^{upd})^T \mathbf{C}_{d,t}^{-1} (\mathbf{d}_t - \mathbf{G}_t \vec{\beta}_t^{upd}) \right] \tag{A.19}$$

In the context of this study, the cost function is a balance between the deviation between the predicted and updated bias coefficient estimates and deviation between real flux observations and posterior flux estimates.

A.2. KALMAN FILTER EQUATIONS: STATE ESTIMATE UPDATE EQUATION

The state estimate update equation can be formulated by first redefining the cost function in equation (A.19) in terms of more general matrices. Terms that are not the *a posteriori* state estimate of the bias coefficients are placed into three general matrices (\mathbf{H} , \mathbf{P} , and \mathbf{X}) given as

$$\mathbf{H} = \begin{pmatrix} \mathbf{I} \\ \mathbf{G}_t \end{pmatrix}, \mathbf{P} = \begin{pmatrix} \mathbf{C}_{\beta,t}^{pre} & 0 \\ 0 & \mathbf{C}_{d,t} \end{pmatrix}^{-1}, \mathbf{X} = \begin{pmatrix} \vec{\beta}_t^{pre} \\ \mathbf{d}_t \end{pmatrix}$$

Substituting these matrices into equation (A.19) gives a much simpler cost function of the form

$$\Psi = (\mathbf{X} - \mathbf{H}\vec{\beta}_t^{upd})^T \mathbf{P} (\mathbf{X} - \mathbf{H}\vec{\beta}_t^{upd}) \quad (\text{A.20})$$

Next, expand the the terms in (A.20) to get the following

$$\Psi = \mathbf{X}^T \mathbf{P} \mathbf{X} - \mathbf{X}^T \mathbf{P} \mathbf{H} \vec{\beta}_t^{upd} - \mathbf{H}^T \vec{\beta}_t^{T,upd} \mathbf{P} \mathbf{X} + \mathbf{H}^T \vec{\beta}_t^{T,upd} \mathbf{P} \mathbf{H} \vec{\beta}_t^{upd} \quad (\text{A.21})$$

The best *a posteriori* estimate of the bias coefficients is achieved through the minimization of the cost function. This is done by taking the derivative of (A.21) with respect to the updated bias coefficient estimates ($\vec{\beta}_t^{upd}$), setting the resultant equation to 0, and solving for $\vec{\beta}_t^{upd}$. It is important to note that to obtain equation (A.22) both the bias coefficient covariance matrix and the observational covariance matrix ($\mathbf{C}_{\beta,t}^{pre}$ and $\mathbf{C}_{d,t}$) must be symmetric matrices.

$$\frac{d\Psi}{dm_t} = -2\mathbf{H}^T \mathbf{P} \mathbf{X} + 2\mathbf{H}^T \mathbf{P} \mathbf{H} \vec{\beta}_t^{upd} \quad (\text{A.22})$$

$$\vec{\beta}_t^{upd} = \frac{\mathbf{H}^T \mathbf{P} \mathbf{X}}{\mathbf{H}^T \mathbf{P} \mathbf{H}} \quad (\text{A.23})$$

Equation (A.23) is known as the least-squares optimization solution. When the general matrices \mathbf{H} , \mathbf{P} , and \mathbf{X} are expanded into equation (A.23) the state estimate update equation for the bias coefficients is obtained.

$$\vec{\beta}_t^{upd} = \frac{\left(\vec{\beta}_t^{pre} \mathbf{C}_{\beta,t}^{pre,-1} + \mathbf{G}_t^T \mathbf{C}_{d,t}^{-1} \mathbf{d}_t \right)}{\left(\mathbf{C}_{\beta,t}^{pre,-1} + \mathbf{G}_t^T \mathbf{C}_{d,t}^{-1} \mathbf{G}_t \right)} \quad (\text{A.24})$$

Equation (A.24) is a mathematically sound state estimate update equation for the Kalman filter, but not the one used in equation (A.4). Equation (A.4) is obtained by using the *matrix inversion lemma* seen below on the denominator term of equation (A.24).

$$(\mathbf{A} - \mathbf{BDC})^{-1} = (\mathbf{A}^{-1} + \mathbf{A}^{-1} \mathbf{B} (\mathbf{D}^{-1} - \mathbf{CA}^{-1} \mathbf{B})^{-1} \mathbf{CA}^{-1}) \quad (\text{A.25})$$

$$\left(\mathbf{C}_{\beta,t}^{pre,-1} - \mathbf{G}_t^T (-\mathbf{C}_{d,t}^{-1}) \mathbf{G}_t \right)^{-1} = \left(\mathbf{C}_{\beta,t}^{pre} - \frac{\mathbf{C}_{\beta,t}^{pre} \mathbf{G}_t^T \mathbf{G}_t \mathbf{C}_{\beta,t}^{pre}}{(\mathbf{C}_{d,t} + \mathbf{G}_t^T \mathbf{C}_{\beta,t}^{pre} \mathbf{G}_t)} \right) \quad (\text{A.26})$$

Substituting equation (A.26) into equation (A.24), and rearranging the resultant terms gives the state update equation for the bias coefficient estimates as seen in equation (A.4).

$$\begin{aligned} \vec{\beta}_t^{upd} &= \left(\mathbf{C}_{\beta,t}^{pre} - \frac{\mathbf{C}_{\beta,t}^{pre} \mathbf{G}_t^T \mathbf{G}_t \mathbf{C}_{\beta,t}^{pre}}{(\mathbf{C}_{d,t} + \mathbf{G}_t^T \mathbf{C}_{\beta,t}^{pre} \mathbf{G}_t)} \right) (\vec{\beta}_t^{pre} \mathbf{C}_{\beta,t}^{pre,-1} + \mathbf{G}_t^T \mathbf{C}_{d,t}^{-1} \mathbf{d}_t) \\ &= \vec{\beta}_t^{pre} + \mathbf{C}_{\beta,t}^{pre} \mathbf{G}_t^T \mathbf{C}_{d,t}^{-1} \mathbf{d}_t - \frac{\mathbf{C}_{\beta,t}^{pre} \mathbf{G}_t^T \mathbf{G}_t \vec{\beta}_t^{pre}}{\mathbf{C}_{d,t} + \mathbf{G}_t^T \mathbf{C}_{\beta,t}^{pre} \mathbf{G}_t} - \frac{\mathbf{C}_{\beta,t}^{pre} \mathbf{G}_t^T \mathbf{G}_t \mathbf{C}_{\beta,t}^{pre} \mathbf{G}_t^T \mathbf{C}_{d,t}^{-1} \mathbf{d}_t}{\mathbf{C}_{d,t} + \mathbf{G}_t^T \mathbf{C}_{\beta,t}^{pre} \mathbf{G}_t} \\ &= \vec{\beta}_t^{pre} + \mathbf{C}_{\beta,t}^{pre} \mathbf{G}_t^T \mathbf{C}_{d,t}^{-1} \mathbf{d}_t \left(\mathbf{I} - \frac{\mathbf{C}_{\beta,t}^{pre} \mathbf{G}_t^T \mathbf{G}_t}{\mathbf{C}_{d,t} + \mathbf{G}_t^T \mathbf{C}_{\beta,t}^{pre} \mathbf{G}_t} \right) - \frac{\mathbf{C}_{\beta,t}^{pre} \mathbf{G}_t^T \mathbf{G}_t \vec{\beta}_t^{pre}}{\mathbf{C}_{d,t} + \mathbf{G}_t^T \mathbf{C}_{\beta,t}^{pre} \mathbf{G}_t} \\ &= \vec{\beta}_t^{pre} + \frac{\mathbf{C}_{\beta,t}^{pre} \mathbf{G}_t^T \mathbf{C}_{d,t}^{-1} \mathbf{d}_t}{\mathbf{C}_{d,t} + \mathbf{G}_t^T \mathbf{C}_{\beta,t}^{pre} \mathbf{G}_t} (\mathbf{C}_{d,t} + \mathbf{G}_t^T \mathbf{C}_{\beta,t}^{pre} \mathbf{G}_t - \mathbf{C}_{\beta,t}^{pre} \mathbf{G}_t^T \mathbf{G}_t) - \frac{\mathbf{C}_{\beta,t}^{pre} \mathbf{G}_t^T \mathbf{G}_t \vec{\beta}_t^{pre}}{\mathbf{C}_{d,t} + \mathbf{G}_t^T \mathbf{C}_{\beta,t}^{pre} \mathbf{G}_t} \\ &= \vec{\beta}_t^{pre} + \frac{\mathbf{C}_{\beta,t}^{pre} \mathbf{G}_t^T \mathbf{d}_t}{\mathbf{C}_{d,t} + \mathbf{G}_t^T \mathbf{C}_{\beta,t}^{pre} \mathbf{G}_t} - \frac{\mathbf{C}_{\beta,t}^{pre} \mathbf{G}_t^T \mathbf{G}_t \vec{\beta}_t^{pre}}{\mathbf{C}_{d,t} + \mathbf{G}_t^T \mathbf{C}_{\beta,t}^{pre} \mathbf{G}_t} \end{aligned}$$

$$\begin{aligned}
&= \vec{\beta}_t^{pre} + \frac{\mathbf{C}_{\beta,t}^{pre} \mathbf{G}_t^T}{\mathbf{C}_{d,t} + \mathbf{G}_t^T \mathbf{C}_{\beta,t}^{pre} \mathbf{G}_t} (\mathbf{d}_t - \mathbf{G}_t \vec{\beta}_t^{pre}) \\
&= \vec{\beta}_t^{pre} + \mathbf{K}_t (\mathbf{d}_t - \mathbf{G}_t \vec{\beta}_t^{pre})
\end{aligned} \tag{A.27}$$

Here \mathbf{I} is the identity matrix and \mathbf{K}_t is known as the ‘‘Kalman Gain’’ matrix. As defined in equations (A.3) and (A.28), the Kalman Gain moderates the updated state estimates of the bias coefficients by balancing the uncertainty in the observations and predicted bias coefficient estimates.

$$\mathbf{K}_t = \frac{\mathbf{C}_{\beta,t}^{pre} \mathbf{G}_t^T}{\mathbf{C}_{d,t} + \mathbf{G}_t^T \mathbf{C}_{\beta,t}^{pre} \mathbf{G}_t} \tag{A.28}$$

A.3. KALMAN FILTER EQUATIONS: STATE COVARIANCE MATRIX

Fundamentally, when the cost function is minimized the state covariance matrix is minimized as well. That is, the more accurate the data that the Kalman filter assimilates for an estimate, the more confident filter becomes about the state estimate. Mathematically, this results in the minimization of the state covariance matrix.

The covariance prediction equation of the bias coefficients estimates is derived from equation (A.11)

$$\begin{aligned}
\mathbf{C}_{\beta,t}^{pre} &= E[(\vec{\beta}_t^{pre} - \vec{\beta}_t^{true})^2] \\
&= E[(\vec{\beta}_t^{pre} - \vec{\beta}_t^{true})^T (\vec{\beta}_t^{pre} - \vec{\beta}_t^{true})]
\end{aligned} \tag{A.29}$$

Using the linear state transition assumption, equation (A.31) becomes the following

$$\begin{aligned}
\mathbf{C}_{\beta,t}^{pre} &= E[(\mathbf{A}_{t-1} \vec{\beta}_{t-1}^{upd} + \mu_t - \mathbf{A}_{t-1} \vec{\beta}_{t-1}^{true})^T (\mathbf{A}_{t-1} \vec{\beta}_{t-1}^{upd} + \mu_t - \mathbf{A}_{t-1} \vec{\beta}_{t-1}^{true})] \\
&= E[(\mathbf{A}_{t-1} (\vec{\beta}_{t-1}^{upd} - \vec{\beta}_{t-1}^{true}) + \mu_t)^T (\mathbf{A}_{t-1} (\vec{\beta}_{t-1}^{upd} - \vec{\beta}_{t-1}^{true}) + \mu_t)]
\end{aligned}$$

$$= E[\mathbf{A}_{t-1}^T (\vec{\beta}_{t-1}^{upd} - \vec{\beta}_{t-1}^{true})^T \mathbf{A}_{t-1} (\vec{\beta}_{t-1}^{upd} - \vec{\beta}_{t-1}^{true}) + 2\mathbf{A}_{t-1}^T (\vec{\beta}_{t-1}^{upd} - \vec{\beta}_{t-1}^{true})^T \mu_t + \mu_t^T \mu_t] \quad (\text{A.30})$$

Finally, take the expectation of equation (A.30) and apply the assumptions in equation (A.14) as follows

$$\mathbf{C}_{\beta,t}^{pre} = \mathbf{A}_{t-1}^T \mathbf{C}_{\beta,t-1}^{upd} \mathbf{A}_{t-1} + Q_{t-1} \quad (\text{A.31})$$

This is the covariance prediction equation of the bias coefficients estimates as seen in equation (A.2).

Derivation of the *a posteriori* state covariance matrix begins by assuming that this is the covariance between the true and *a posteriori* state estimates at the current time. In this study, this matrix is the covariance between the true and *a posteriori* bias coefficient estimates.

$$\begin{aligned} \mathbf{C}_{\beta}^{upd} &= E[(\vec{\beta}_t^{true} - \vec{\beta}_t^{upd})^2] \\ &= E[(\vec{\beta}_t^{true} - \vec{\beta}_t^{upd})^T (\vec{\beta}_t^{true} - \vec{\beta}_t^{upd})] \end{aligned} \quad (\text{A.32})$$

Next, substitute $\vec{\beta}_t^{upd}$ with equation (A.27) and \mathbf{d}_t with equation (A.10) in equation (A.32) and collect terms. Finally, expand the two polynomial terms in equation (A.33) and evaluate the expectation using equations (A.11) and (A.13).

$$\begin{aligned} \mathbf{C}_{\beta}^{upd} &= E[(\vec{\beta}_t^{true} - (\vec{\beta}_t^{pre} + \mathbf{K}_t(\mathbf{d}_t - \mathbf{G}_t \vec{\beta}_t^{pre})))^T (\vec{\beta}_t^{true} - (\vec{\beta}_t^{pre} + \mathbf{K}_t(\mathbf{d}_t - \mathbf{G}_t \vec{\beta}_t^{pre})))] \\ &= E[((\mathbf{I} - \mathbf{K}_t \mathbf{G}_t)(\vec{\beta}_t^{true} - \vec{\beta}_t^{pre}) - \mathbf{K}_t \nu_t)^T ((\mathbf{I} - \mathbf{K}_t \mathbf{G}_t)(\vec{\beta}_t^{true} - \vec{\beta}_t^{pre}) - \mathbf{K}_t \nu_t)] \end{aligned} \quad (\text{A.33})$$

$$\begin{aligned} &= E[(\mathbf{I} - \mathbf{K}_t \mathbf{G}_t)^T (\vec{\beta}_t^{true} - \vec{\beta}_t^{pre})^T (\mathbf{I} - \mathbf{K}_t \mathbf{G}_t) (\vec{\beta}_t^{true} - \vec{\beta}_t^{pre}) + \mathbf{K}_t^T \nu_t^T \mathbf{K}_t \nu_t] \\ &= (\mathbf{I} - \mathbf{K}_t \mathbf{G}_t)^T \mathbf{C}_{\beta,t}^{pre} (\mathbf{I} - \mathbf{K}_t \mathbf{G}_t) + \mathbf{K}_t^T \mathbf{C}_{d,t} \mathbf{K}_t \end{aligned} \quad (\text{A.34})$$

Equation (A.34) is known as the “Joesph’s Form” of the bias coefficient estimate covariance update equation.

Finally, equation (A.6) is an inflation equation of the *a posteriori* bias coefficient estimate covariance matrix. This adjustment prevents a zero or a negative probability density function. It is presented in Zhang et al. (2004) and is defined as follows

$$\mathbf{C}_{\beta,t}^{upd} = \mathbf{C}_{\beta,t}^{upd,*}(w) + \mathbf{C}_{\beta,t}^{pre}(1 - w) \quad (\text{A.35})$$

where $\mathbf{C}_{\beta,t}^{upd,*}$ is the *a posteriori* bias coefficient estimate covariance matrix from equation (A.34), $\mathbf{C}_{\beta,t}^{pre}$ is the predicted bias coefficient estimate covariance matrix and “w” is a weighting factor between 0 and 1 used for the inflation magnitude.

TABLE A.1. Variables present in equations (2.6) through (2.11). All variables are given at a current assimilation time (t).

Variable	Definition
$\vec{\beta}_t^{pre}$	Predicted bias coefficient estimates (state estimate)
$\vec{\beta}_t^{true}$	True value of bias coefficients
$\vec{\beta}_t^{upd}$	<i>A posteriori</i> or updated bias coefficient estimates
\mathbf{d}_t	Vector of flux observations
\mathbf{A}_{t-1}	Transition matrix of bias coefficient estimates between assimilation times
μ_t	White noise error in the bias coefficient estimates between assimilation times
ν_t	Error in the flux observations at the current assimilation time
\mathbf{Q}_t	Transition noise covariance matrix of bias coefficient estimates
$\mathbf{C}_{\beta,t}^{pre}$	Predicted bias coefficient estimates covariance matrix
$\mathbf{C}_{\beta,t}^{upd}$	<i>A posteriori</i> or updated bias coefficient estimates covariance matrix
\mathbf{K}_t	Kalman Gain matrix
\mathbf{G}_t	Bias coefficient estimates space to flux space Jacobian at current assimilation time
\mathbf{I}	Identity matrix
w	Inflation parameter to prevent bias coefficient estimates covariance collapse
E	Expectation of a variable